NOAA Technical Memorandum ERL ETL-285

DEPARTMENT OF COMMERCE
UNITED STATES OF AMERICA

LABORATORY MODELING AND THEORETICAL STUDIES OF WAVE PROCESSES IN THE OCEAN

Part 3: Second Stage Results

L.A. Ostrovsky, Editor

Environmental Technology Laboratory
Boulder, Colorado
November 1997

noaa NATIONAL OCEANIC AND ATMOSPHERIC ADMINISTRATION / Environmental Research Laboratories

NOAA Technical Memorandum ERL ETL-285

LABORATORY MODELING AND THEORETICAL STUDIES OF WAVE PROCESSES IN THE OCEAN

Part 3: Second Stage Results

L.A. Ostrovsky, Editor

Environmental Technology Laboratory
Boulder, Colorado
November 1997

**UNITED STATES
DEPARTMENT OF COMMERCE**

**William M. Daley
Secretary**

NATIONAL OCEANIC AND
ATMOSPHERIC ADMINISTRATION

D. JAMES BAKER
Under Secretary for Oceans
and Atmosphere/Administrator

Environmental Research
Laboratories

James L. Rasmussen
Director

NOTICE

The Memorandum outlines the results of the second stage of the research work of the Institute of Applied Physics (IAP) of the Russian Academy of Sciences, which has been carried out in the framework of the Agreement between IAP and the NOAA Environmental Technology Laboratory (ETL). The work was supported by the joint NOAA/DOD Advanced Sensor Applications Program (ASAP).

Head of the Project: V.I. Talanov
Program Coordinator: L.A. Ostrovsky
Authors: V.V. Bakhanov, I.S. Dolina, S.A. Ermakov, E.M. Gromov, V.V. Papko, V.I. Talanov, Yu. I. Troitskaya

The large IAP wave tank experiments were performed with the participation of:

S.D. Bogatyrev, V.I. Kazakov, D.P. Korotkov, B.V. Serin, I.I. Gopalo

Translator: N.V. Rudik

For sale by the National Technical Information Service, 5285 Port Royal Road
Springfield, VA 22061

Contents

Laboratory Modeling and Theoretical Studies of Wave Processes in the Ocean

Part 3: Second Stage Results

Edited by L. A. Ostrovsky

Abstract

The results of theoretical and experimental studies of surface water waves and their interactions with subsurface currents and turbulence are presented. The experiments were carried out in several laboratory tanks of the Institute of Applied Physics. The theoretical chapter includes the theory of short wind-wave growth rate modulation by long surface waves, of nonlinear evolution of a short surface wave train, and of surface wave scattering by a moving body. The experiments described below are a detailed investigation of two-dimensional contrasts in a surface wave created by an inhomogeneous current, optical measurements of curvature and slope distributions in gravity-capillary waves, and laboratory experiments on surface wave interaction with a small-scale turbulence.

1 Introduction

This is a continuation of the previous ETL Technical Memorandums (see [?] and [?]) devoted to the results of theoretical and experimental studies of processes in the upper ocean, performed by the Institute of Applied Physics under the agreement with ETL and based, to a large degree, on design and use of the IAP laboratory complex. This part deals mainly with some "hot topics" concerning surface waves and signatures of underwater flows via surface waves.

As in the previous Memorandum [?], this Memorandum is divided into theoretical and experimental chapters. In both of them, some results can be considered as a direct development of previous results. In this context, a theory of propagation of short, intense, gravity wave trains is developed to describe the experimental data given in the previous Memorandum. On the other hand, the experimental chapter begins with experiments on constructing two-dimensional contrast patterns formed in a surface gravity wave by an inhomogeneous subsurface current created in the large tank by a moving sphere. These wave perturbations can also arise around bottom features in shallow sea. Experimental data show a good qualitative agreement with theoretical considerations of this problem given in the previous Memorandum.

Among the new problems considered here is an important theoretical problem of short gravity-capillary wave modulation by longer waves through the turbulent atmospheric boundary layer. The variation of short wind-wave growth rate due to a long wave is calculated to show that the effect can be significant. In the end of the theoretical chapter, surface-wave scattering by a moving underwater obstacle is considered; it is shown that such effect can be of a resonant character and, as a result, leads to a formation of strong surface contrasts.

The experimental chapter, apart from the experiments on surface wave modulation mentioned above, describes an optical method of measuring curvature distributions in surface waves, which has been developed and realized in the wind-wave tank. This method enables distinguishing positive and negative curvatures and selecting the "parasitic" capillary ripples generated near the crests of strong gravity waves. Finally, the interactions between a surface wave and subsurface turbulence are investigated: additional wave damping due to turbulence as well as the effect of the wave on turbulence spectrum have been studied experimentally.

2 Theoretical Studies

2.1 Modulation of the growth rate of a short surface wave riding on a long wave under the turbulent wind

The interactions between short surface waves (of centimeter and decimeter wave bands) and long waves (waves close to a peak in the spectrum of wind waves or swell) are intensively studied because of their importance for the problem of remote sensing of long surface waves. Numerous measurements of the ocean wave-radar modulation transfer function (MTF) have been carried out (see survey [3] and references therein). The MTF is defined as the ratio of the intensity modulation of the radar signal scattered by a long wave and the steepness of the latter. The measurements show that, except in the case of small grazing angles of the radar beam, the MTF modulus is mainly defined by short-wave modulation; it increases with decreasing long-wave frequency f, up to the values of 12 - 15 for $f = 0.1$ Hz. As mentioned in [3], such large values of MTF cannot be explained in the framework of commonly used, conservative kinematic models.

One of the possible mechanisms suggested for this effect in [4] and [3] is associated with variations of the growth rate (increment) of short waves via modulation of wind stress in air. It has been demonstrated in [3] that for obtaining the MFT modulus values of 12 - 15, the increment modulation coefficient should be 25 - 30. However, the increment modulation values have not been calculated in either of works [3, 4]. Such a calculation was probably made first in [5], where the Orr-Zommerfeld equation that is valid for a laminar flow was solved. A detailed calculation of the increment modulation in the framework of the quasi-laminar Miles model [6] was performed in [7]. It was then assumed that the air velocity profile over waves was linearly logarithmic, while the coefficient of the momentum exchange was taken to be equal to the air molecular viscosity ν_a. The coefficient of growth-rate modulation for short waves was defined as a combination of the ratio of velocity gradient oscillations due to the long wave and an average wind velocity gradient close to the water surface, which was characterized by the value $M = \frac{2cka}{u_*^2}(ck\nu_a)^{\frac{1}{2}}$. (Here, c, k, and a are phase velocity, wavenumber, and the amplitude of the long-wave surface displacement, respectively; u_* is the wind friction velocity). However, in the framework of that model, the characteristic scale of the viscous boundary layer for a long wave, $\delta_w = \left(\frac{\nu_a}{ck}\right)^{\frac{1}{2}}$, greatly exceeds the thickness of the viscous sublayer in the turbulent boundary layer, $\delta_0 = \frac{10\nu_a}{u_*}$, corresponding to the wind flow, which is true even at weak winds close to the short-wave generation threshold. As a result, the ratio of the oscillatory and average velocity gradients and the corresponding ratio of the oscillatory and average parts of the short-wave increment proved to be approximately 3 times lower than necessary for an explanation of the experiment described in [3]. Besides, it should be noted that although for short waves, the turbulent momentum exchange can be neglected, turbulent stresses should be taken into account for determining the long-wave field in air, the characteristic vertical scale of which essentially exceeds the thickness of a viscous sublayer.

We have performed calculations of the modulation coefficient for short-wave growth rate in the framework of a more rigorous and complete model of the wind boundary layer over a wavy water surface suggested in [10]. It is based on the use of curvilinear coordinates, (ξ, η), in which one of the coordinate lines coincides with a water surface undulated by a wave. A simple gradient approximation with the effective coefficient of turbulent viscosity $\nu(\eta)$ obtained in [11] is employed to parametrize turbulent momentum fluxes:

$$\langle u_i' u_j' \rangle = \langle u_i^2 \rangle \delta_{ij} + \nu(\eta) \left[\frac{\partial \langle u_i \rangle}{\partial x_j} + \frac{\partial \langle u_i \rangle}{\partial x_j} \right],$$

where

$$\nu(\eta) = \nu_a \left[1 + 0.4\eta^+ \left(1 - e^{-\left(\frac{\eta^+}{L}\right)^2} \right) \right],$$

$\eta^+ = \eta u_* / \nu_a$, and $L = 22.4$ for a hydrodynamically smooth surface.

This model, based on the gradient approximation of the turbulent stresses and the use of curvilinear coordinates, is applied to the calculation of growth rate variations of the short wave in the presence of a long wave. For this purpose, the model should be generalized for a case in which the water surface is undulated by two waves of strongly different scales (long and short ones). The problem is to obtain the equations for the short-wave perturbation in the presence of the long-wave disturbance in the air. The procedure of obtaining such equations is based on the double coordinate transformation.

First, the transformation is performed from Cartesian coordinates (x, y) to the long-wave coordinates (s, γ) in which the coordinate line $\gamma = 0$ coincides with the water surface perturbed by the long wave.

The equations for the long-wave disturbance in the air are presented in terms of the stream function

$$\psi = -c\gamma + \int U_0(\gamma)\, d\gamma + \varphi_1(s, \gamma), \qquad (1)$$

and vorticity

$$\chi = U_{0\gamma} + \chi_1(s,\gamma),$$

where $U_0(\gamma)$ is the undisturbed velocity profile in the air. They correspond to the reference frame moving with the phase velocity of the steady-state long wave, $c^2 = g/k$ (g is the gravity acceleration),

$$\begin{aligned}\left[(U_0 - c)\chi_{1s} - \varphi_{1s}U_{0\gamma\gamma} - \left(\frac{\partial^2}{\partial s^2} + \frac{\partial^2}{\partial \gamma^2}\right)(\chi_1\nu)\right] = \\ = -2\nu_{\gamma\gamma}\varphi_{1ss} - I_\gamma\left(\left(U_0 - c\right)\nu_\gamma\right)_\gamma,\end{aligned} \tag{2}$$

$$\frac{\partial^2\varphi_1}{\partial s^2} + \frac{\partial^2\varphi_1}{\partial\gamma^2} = -2kae^{-k\gamma}U_{0\gamma} + \chi_1. \tag{3}$$

The set (2), (3) is supplemented with the boundary "no-leaking" condition

$$\varphi_1|_{\gamma=0} = 0 \tag{4}$$

and the "adhesion" condition, which can be reduced to a form

$$\partial\varphi_1/\partial\gamma|_{\gamma=0} = 2ckae^{iks}. \tag{5}$$

Then, in the reference frame moving along the curved surface $\gamma = 0$ with the phase velocity of the short wave, where the short-wave disturbance is quasi-stationary, the further transformation is performed from the long-wave coordinates to the short-wave ones, (ξ,η), so that the coordinate line $\eta = 0$ coincides with the water surface undulated by the short wave riding on the long wave. All the subsequent expressions are the approximate ones, valid within the first order of the small parameters of the problem: the ratios of the short- and long-wave lengths and their periods. In the reference frame under consideration, the stream function Φ and the vorticity X are

$$\Phi = -C(1-2\alpha)\eta + (\varphi_1(\eta,\Sigma) - 2\alpha c\eta) + \int U_0(\eta)\,d\eta + \psi_2(\eta,\xi,\Sigma).$$

$$X = U_{0\eta} + \chi_1(\eta,\Sigma) + \chi_2(\eta,\xi,\Sigma) \tag{6}$$

Here, Σ is the phase of elevation in the long wave, $\alpha = ka\cos\Sigma$, $C = \sqrt{g/K + TK(1+3\alpha)}$, K and A being the wavenumber and the amplitude of elevation in the short wave respectively, and T is the surface tension coefficient.

As a result of this double coordinate transformation, the system of equations for short-wave disturbance in the air on the background of the long wave is obtained:

$$\begin{gathered}(1-2\alpha)\left[\left(\Phi_{0\eta}\chi_2-\psi_2\chi_{0\eta}\right)iK-\left(\tfrac{d^2}{d\eta^2}-K^2\right)(\chi_2\nu)\right]=\\ =-2\nu_{\eta\eta}\psi_2K^2-2KAe^{-K\eta}\left(\Phi_{0\eta}\nu_\eta\right)_\eta,\end{gathered}$$

$$\frac{d^2\psi_2}{d\eta^2}-K^2\psi_2=\left[\chi_2-2KAe^{-K\eta}\chi_0\right](1-2\alpha). \qquad (7)$$

It is similar to the system of equations for the long-wave variations in air (2, 3), but the coefficients of the equations contain not only undisturbed velocity and vorticity, but the long-wave disturbances of these values :

$$\Phi_{0\eta}=-C(1-2\alpha)+\left(\varphi_{1\eta}(\eta,\Sigma,\Upsilon)-2\alpha c\right)+U_0(\eta),$$

$$\chi_0=U_{0\eta}+\chi_1(\eta,\Sigma,\Upsilon).$$

The set (7) should be supplemented by the boundary conditions. The first of them is again the "no-leaking" condition:

$$\psi_2|_{\eta=0}=0. \qquad (8)$$

The second one is the "adhesion" condition, that of the continuity of the velocity component tangential to the surface:

$$\psi_{2\eta}|_{\eta=0}=2C(1-2\alpha)KA. \qquad (9)$$

The system (7) with boundary conditions (8), (9) has been solved numerically by the grid method using the same scheme as in [10]. Before that, the long-wave perturbations of the stream function and the vorticity, φ_1 and χ_1 included in the coefficients of set (7), were found by employing a numerical solution of the system (2, 3) with the same method.

After that, the wind increment $\beta=\operatorname{Im}\omega_w$, depending on the long wave phase, was calculated. In the case of rather small steepness of the long wave, one can represent the wind increment as

$$\beta=\beta_0\left(1+mka\cos(\Sigma-\varphi_m)\right).$$

The values m and φ_m for various lengths of a long wave and of friction velocities were calculated using the above numerical results. Figures 1(a, b), 2(a, b), and 3(a, b) show the dependencies of the modulus m and the phase φ_m of the wind increment modulation coefficient on the parameter c/u_* for the cases of $u_* = 10$ cm/s, $u_*= 20$ cm/s, and $u_*=30$ cm/s, and for the wavenumbers of a short wave K equaling 0.3 cm^{-1} and 3 cm^{-1}, respectively. All the curves have a typical shape with a minimum at $c/u_*=20\div30$. To explain these results, one should determine the position of the region of energy exchange between the short wave and wind flow with respect to profiles of long-wave perturbations of hydrodynamic fields in air, which cause modulation of the increment.

First of all, we define what the region of energy exchange between a wave and a flow is. For this purpose, we consider a harmonic short wave without a long wave. An integral expression for an energy flux on the water surface from wind to waves, which is proportional to their wind increment, has been obtained in [12], for this case from the equation of the energy balance for wave perturbation. This expression can be written as:

$$-\left\langle(\mathcal{P}-\mathcal{S}_{22})\mathcal{V}-\mathcal{S}_{12}\mathcal{U}\right\rangle\big|_{\eta=0}=\int\limits_0^\infty T_{sour}(\eta)\,d\eta+\int\limits_0^\infty T_{vis}(\eta)\,d\eta, \tag{10}$$

where $T_{sour}(\eta)=U_0(\eta)\dfrac{d}{d\eta}\left(\langle\sigma_\tau\rangle-u_*^2\right)$ and
$T_{vis}(\eta)=-\nu\left\langle(D_{22}+U_{0\eta}x_\eta)^2+(D_{12}+U_{0\eta}y_\eta)^2\right\rangle$.

Here, the angle parentheses mean averaging over the wavelength; $u=\dfrac{\partial\psi}{\partial x}, v=-\dfrac{\partial\psi}{\partial y}$ are the horizontal and vertical velocities, respectively; p is the pressure; σ_{ij} are components of the viscous stress tensor; σ_τ is the tangential stress; $\mathcal{P}=p-\langle p\rangle$; $\mathcal{U}=u-\langle u\rangle$; $\mathcal{V}=v-\langle v\rangle$; $\mathcal{S}_{ij}=\sigma_{ij}-\langle\sigma_{ij}\rangle$; $D_{ij}=\mathcal{S}_{ij}/\nu$.

Equation (10) has a simple physical meaning. The first term in its right-hand side is the work done by the tangential stress force averaged over the wave period in the resting reference frame (while in a stationary wave field, this force is balanced by a radiation force). The second term describes viscous dissipation of the wave energy in air. Thus, the energy flux from wind to waves is determined by a balance of the average radiation force power and viscous losses.

The vertical profiles of the sum of the integrands $T_{sour}+T_{vis}$ for the waves with $K = 0.3\text{cm}^{-1}$, 1cm^{-1}, 3cm^{-1} and the wind friction velocities u_*=10cm/s, u_*=20cm/s, u_* =30cm/s are presented in Fig. 4(a, b, c). It is seen that the maximum of $T_{sour} + T_{vis}$ is located close to the viscous sublayer boundary. However, as the wavelength grows, the energy exchange region moves away from the surface, and at K=0.3cm^{-1}, its essential part is located in the turbulent boundary layer.

Let us now consider the form of the long-wave perturbation fields close to the surface where the region of energy exchange between a short wave with air flux lies. Hence, we deal with the solution of the set (2, 3). The simplest case is when, in the considered region of the stream, $c \gg U_0$. Since at the viscous sublayer boundary, $U_0 \simeq 10 \div 12u_*$ [9], and the air velocity above this level varies relatively slowly, this condition is equivalent to $c \gg 12u_*$. Then, Equations (2), (3) simplify and can be reduced to the form:

$$\frac{d^2T_1}{d\gamma^2} + ikc\frac{T_1}{\nu(\gamma)} = 0, \qquad (11)$$

where $T_1 = \chi_1\nu$ has the meaning of the long-wave perturbation of tangential viscous stress to an accuracy of the order of $k\delta$ (where δ is the viscous sublayer thickness).

We assume that the characteristic scale of variability of $T_1(\gamma)$ is large compared to δ. Here, $\nu(\gamma) = 0.4u_*\gamma$, and the characteristic scale for T_1 is $L_T = \dfrac{u_*}{kc}$. Taking into account that $\delta = \dfrac{10\nu_a}{u_*}$, we write the applicability condition $L_T \gg \delta$ in the form:

$$\frac{0.4u_*^2}{kc\nu_a} \gg 10. \qquad (12)$$

If condition (12) is fulfilled, one can easily find expressions for $\Phi_{0\eta}$ and χ_0, included in (7), for the considered region:

$$\chi_0 = \frac{u_*^2 + \mathrm{Re}\left(T_1 e^{i(\Sigma - \Upsilon)}\right)}{\nu(\eta)},$$

$$\Phi_{0\eta} = U_0(\eta)\left(1 + \mathrm{Re}\left(\frac{T_1 e^{i(\Sigma-\Upsilon)}}{u_*^2}\right)\right).$$

Hence, obtaining long-wave perturbations of the velocity, vorticity, and other hydrodynamic fields in air is reduced to the similarity transformation for the velocity and vorticity profiles without variations in their characteristic form. For the velocity profile variation given above, the wind increment is

$$\beta(1+\varepsilon)|_{\varepsilon=\frac{T_1}{u_*^2}} = \beta(1+\varepsilon)|_{\varepsilon=0} + \left.\frac{\partial\beta}{\partial\varepsilon}\right|_{\varepsilon=0}\frac{T_1}{u_*^2},$$

while

$$me^{i\varphi_m} = \frac{1}{\beta ka}\frac{\partial\beta}{\partial\varepsilon}\frac{T_1}{u_*^2}. \tag{13}$$

Dashed lines in Figs. 1(a), 2(a), and 3(a) show the solutions found from the approximate formula (13). T_1 was calculated numerically using the solution of the system (2, 3). The value $\frac{\partial\beta}{\partial\varepsilon}$ was calculated for the limit $ka = 0$ employing the solution of the same system, in which the mean fields were assigned as $U_0(1+\varepsilon)$, $\chi_0(1+\varepsilon)$, $\chi_{0\eta}(1+\varepsilon)$. One can see good agreement between precise and approximate curves at large c/u_*, when condition (12) is fulfilled.

If the wind velocity U_0 is small compared to the wave-phase velocity c, and γ is of the order of the variability scale (T_1 - L_T), then one can obtain an approximate expression for T_1:

$$T_1 = \frac{0.8u_*cka}{\ln\left(\frac{3.15kc\nu_a}{0.4u_*^2}\eta_0^+\right) + i\frac{\pi}{2}}, \tag{14}$$

where η_0^+ is the dimensionless roughness parameter expressed in viscous lengths. In the case of a hydrodynamically smooth surface, η_0^+=0.15. The dependences of the modulus $\frac{T_1}{kau_*^2}$ and the phase φ_{T_1} of the modulation coefficient of the tangential viscous stress on $\frac{c}{u_*}$, calculated from formula (14) with the use of the numerical solution for the set (2, 3), are given in Fig. 5(a,b). It is seen that at large $\frac{c}{u_*}$, an approximate solution is close to an exact one. Here, $\left|\frac{T_1}{kau_*^2}\right| \gg 1$, while the dependence of $\frac{T_1}{kau_*^2}$ on $\frac{c}{u_*}$ (and thus, the dependence of m on $\frac{c}{u_*}$) is almost linear.

At $\frac{c}{u_*} < 30$, the characteristic scale of the function $T_1(\eta^+)$ becomes comparable to the viscous sublayer width. As an illustration, the profiles

$T_1(\eta^+)$ for $u_* = 10cm/s = \frac{c}{u_*} = 10, 20, 100$, and the profiles $T_{sour} + T_{vis}$ for $k = 0.3cm^{-1}, 1cm^{-1}$, and $3cm^{-1}$ are shown in Fig. 6. It can be seen that at $\frac{c}{u_*} = 100$, the curve $T_1(\eta^+)$ is much wider than the energy exchange region, while for $\frac{c}{u_*} = 10$ and 20, these scales are comparable. Here, at $\frac{c}{u_*} = 20$, the energy exchange regions coincide with the minimum of T_1, and there is a minimum in plots of $m\left(\frac{c}{u_*}\right)$.

In conclusion, we shall compare the calculated and experimental data; the latter, given in [13], are referred to in the survey [3]. In the latter, amplitudes and phases of measured modulation transfer functions (MTF) for two wavelengths $\lambda = 2.1$ cm and $\lambda = 12$ cm in the range of long-wave frequencies f from 0.5 Hz to 0.1 Hz are presented. A specific feature of these dependences is the growth of MFT modulus, $|m_{MTF}|$ with the wavelength, achieving 12 - 15 for $f = 0.1$ Hz. MFT phase shift with respect to the long wave varied from 0 to 30° - 40°. As already mentioned, according to [3], these values of $|m_{MTF}|$ cannot be explained by the conservative kinematic effect. The short-wave increment modulation was discussed in [3] as one of the possible mechanisms providing large values of $|m_{MTF}|$. And to ensure quantitative agreement with observations, the increment modulation coefficient m must equal 25 - 30. The dependences of m and φ_m on f are presented in Figs. 7 and 8 (a, b). It is seen that the calculations yield the values m of the order of 25 - 30 at f close to 0.1 Hz, which is sufficient for the strong modulation. However, the phase values calculated for the same frequency are close to $-\pi$. This value strongly differs from the experimentally observed phases of MTF and of the modulation coefficient of the short surface wave spectrum. In general, however, the phase of the wave spectrum does not coincide with the increment modulation phase. This takes place only when the relaxation time for the short waves is small compared to the long wave period. If these values are comparable, as they appear in the considered bandwidth of parameters, the phases of the increment and the spectrum modulations are related in a rather complicated way. In any case, it is shown here that the modulation coefficient of the short-wave increment can be large for a high relative velocity of a long wave. This effect should be taken into account when calculating the modulation of the short wave spectrum by long waves. At the same time, the contribution of another factor discussed in [3], i.e., the effects caused by the modulation of a wind drift in water, should also be estimated in order to obtain a reliable theory of short wave modulation.

2.2 The dynamics of short intense deep-water gravity wave trains

In the previous Memorandum [2], the experimental results demonstrating the profile distortion of the short (about 2.5 wave lengths), intense deep-water gravity wave packets were presented. One of these results is reconstructed in Fig. 9. One can see significant asymmetric distortion of the pulse shape, which is cumulated with the distance. These distortions cannot be described by the nonlinear Schrödinger equation (NLS), which is commonly used for nonlinear gravity waves. For this equation, under any symmetric initial condition, only symmetric deformations of wave envelope are possible. Hence, the higher-order approximation of the nonlinear dispersion theory is needed here.

Upon considering the third-order terms with respect to the wave amplitude and an inverse length of the packet, the corresponding equation for the wave-complex amplitude can be written in the following general form:

$$2i\frac{\partial\psi}{\partial t}+q\frac{\partial^2\psi}{\partial\xi^2}+\alpha\left|\psi\right|^2\psi=$$
$$-2i\left(\beta\left|\psi\right|^2\frac{\partial\psi}{\partial\xi}+\mu\psi\frac{\partial\left|\psi\right|^2}{\partial\xi}\right)-i\gamma\frac{\partial^3\psi}{\partial\xi^3}-\psi U\left(\left|\psi\right|^2\right), \qquad (15)$$

where the coefficients q, α, β, μ, and γ are constants. Equation (15) contains the main (second-order) terms in its left-hand side, and the third-order terms in its right-hand side. In the latter, the parenthetic terms give rise to the steepening of the wave envelope fronts. The possibility of self-steepening of the envelope wave, including that caused by the nonlinear dispersion, was first considered in [14] and [15]. In optics, this effect was studied in detail in [16] within the framework of the nonlinear geometrical optics method. For intense deep-water gravity wave packets, the envelope equation in the third-order approximation of the nonlinear dispersion theory was first studied by Dysthe [17]. It has the form

$$2i\left(\frac{\partial a}{\partial t}+\frac{5}{2}V_g^L k_0^2\left|a\right|^2\frac{\partial a}{\partial\xi}\right)+\frac{\omega_0}{4k_0^2}\frac{\partial^2 a}{\partial\xi^2}+\omega_0 k_0^2\left|a\right|^2 a-i\frac{\omega_0}{8k_0^3}\frac{\partial^3 a}{\partial\xi^3}+$$

$$+\omega_0 k_0 a \int_{-\infty}^{+\infty} \left|a\left(\xi',t\right)\right|^2 \frac{\left[(\xi-\xi')^2 - s^2\right]}{\left[(\xi-\xi')^2 + s^2\right]^2} d\xi' = 0. \qquad (16)$$

Here, a is the water surface deviation from the equilibrium for a wave train, the wavenumber k_0 and frequency ω_0 satisfy the linear dispersion relation $\omega_0^2 = gk_0$, and $V_g^L = \omega_0/(2k_0)$ is the group velocity of the train. In particular, the decrease both in the growth rate and the modulation instability region in comparison with the NLS approximation has been demonstrated. Equations (15) and (16) coincide under the conditions

$$a \equiv \psi,\ q = \frac{\omega_0}{4k_0^2},\ \alpha = \omega_0 k_0^2,\ \beta = \frac{5}{2} V_g^L k_0^2 \left|a\right|^2,\ \gamma = -\frac{\omega_0}{8k_0^3}.$$

Note that the integral in the right-hand side of (16) is due to the period-averaged flow induced by a gravity wave train near the water surface.

Let us now come back to Eq. (15) and analyze the effects of the higher-order approximation.

2.2.1 General properties of the higher-order nonlinear equation

As already mentioned, the first and second terms in the right-hand side of Eq. (15) correspond to the dependence of the local wave-train group velocity on its intensity $|\psi|^2$ (nonlinear dispersion). In order to demonstrate this, we assume $q = \alpha = \gamma = U = 0$ to reduce the equation to the simple-wave form

$$\frac{\partial |\psi|^2}{\partial t} + (\beta + 2\mu)\, |\psi|^2 \frac{\partial |\psi|^2}{\partial \xi} = 0.$$

We see that the wave groups of different intensities move with different group velocities

$$\frac{d\xi}{dt} = \Delta V_g^{NL} = (\beta + 2\mu)\, |\psi|^2 . \qquad (17)$$

For $(\beta + 2\mu) > 0$, the wave groups of higher intensity move with higher velocities so that the leading front of the initially symmetric train becomes steeper. In the opposite case, when $(\beta + 2\mu) < 0$, the trailing edge of an initially symmetric wave train becomes steeper.

In order to estimate the role of the steepening effects, let us find the velocity of the "mass center" in a reference frame moving with the linear group velocity V_g^L :

$$\overline{\xi(t)} = \frac{1}{N_0}\int_{-\infty}^{+\infty} \xi\,|\psi|^2\,d\xi, \tag{18}$$

where $N_0 = \int_{-\infty}^{+\infty} |\psi|^2\,d\xi$ is the wave-train energy. For the velocity of the localized wave trains from (18), in case of a real function U $(U = U^*)$, we obtain

$$\overline{\overset{\bullet}{\xi}(t)} = \frac{(\beta + 2\mu)}{2N_0}\int_{-\infty}^{+\infty} |\psi|^4\,d\xi - \frac{3\gamma}{2N_0}\int_{-\infty}^{+\infty}\left|\frac{\partial\psi}{\partial\xi}\right|^2 d\xi + \frac{1}{N_0}\int_{-\infty}^{+\infty}\frac{\partial\varphi}{\partial\xi}\,|\psi|^2\,d\xi, \tag{19}$$

where $\bullet \equiv d/dt$, and φ is the wave phase $(\psi = |\psi|\exp(i\varphi))$. The last term in (19) describes the motion of the packet in frames of the NSL. The additional change of the wave velocity, $\overline{\Delta V} = \overline{\overset{\bullet}{\xi}(t)}$, in comparison with the NLS case, is described by two other terms: $\overline{\Delta V} = \overline{\Delta V}^{NL} + \overline{\Delta V}^{L}$. The term $\overline{\Delta V}^{NL}$ depends on the field intensity and is due to the nonlinear dispersion discussed above:

$$\overline{\Delta V}^{NL} = \frac{(\beta + 2\mu)}{2N_0}\int_{-\infty}^{+\infty} |\psi|^4\,d\xi. \tag{20}$$

The second term, $\overline{\Delta V}^{L}$, does not depend on the wave intensity at all. It is due to the additional, higher-order dispersion effect (an analog of the aberration in optics) existing in a linear wave:

$$\overline{\Delta V}^{L} = \frac{3\gamma}{2N_0}\int_{-\infty}^{+\infty}\left|\frac{\partial\psi}{\partial\xi}\right|^2 d\xi. \tag{21}$$

This aberrational velocity perturbation is negative for $\gamma > 0$ and positive for $\gamma < 0$. Its absolute value , $\left|\overline{\Delta V}^{L}\right|$, increases with the decrease of the wave train width, i.e., with the increase of its spectral bandwidth.

2.2.2 Numerical study of intense short deep-water gravity wave trains

The propagation of intense deep-water gravity wave trains was investigated in numerous experiments (see, for example, [18]). The experimental results obtained were in most cases interpreted with the NLS corresponding to the second-order ("parabolic") approximation of the dispersion theory ([18], [19], [20]). The discrepancies between these thoretical models and experimental results were associated, in particular, with the violation of symmetry of the wave-train shape and the dependence of wave velocity on its intensity. Some of these peculiarities were investigated numerically in [21] in frames of Dysthe's equation (16). However, important effects of the dependence of the velocity of a wave train on its intensity were not analyzed in [21].

For a detailed comparison to the third-order approximation theory with the experiments, we have carried out the following numerical experiments.

For the description of the wave-train shape evolution in the third-order approximation, we performed numerical simulation on the basis of Eq. (16). In the dimensionless variables

$$\tau = \frac{t}{T},\ \eta = \frac{\xi}{l},\ \psi = \frac{a}{\bar{a}}, \tag{22}$$

where

$$\omega_0 T = \frac{25}{4},\ k_0 l = \frac{5}{4},\ k_0\, \bar{a} = \frac{2}{5},$$

Eq. (16) takes the form

$$2i\left(\frac{\partial\psi}{\partial\tau} + |\psi|^2\frac{\partial\psi}{\partial\eta}\right) + \frac{\partial^2\psi}{\partial\eta^2} - i\frac{2}{5}\frac{\partial^3\psi}{\partial\eta^3} + |\psi|^2\psi +$$

$$-\frac{4}{5}\psi\int\limits_{-\infty}^{+\infty}\frac{\partial\left(|\psi(\eta',\tau)|^2\right)}{\partial\eta'}\frac{d\eta'}{(\eta-\eta')} = 0. \tag{23}$$

The initial conditions for Eq. (23) were specified in the form of the even function without phase modulation (similar to the known NLS soliton but without any fixed relationship between ψ_0 and δ):

$$\psi(\eta, 0) = \frac{\psi_0}{\cosh(2\eta/\delta)}. \tag{24}$$

The dimensionless parameters are $\psi_0 = 0.75$ and $\delta = 4\pi$. They correspond to the experimental values of the gravity wave slope $k_0 a = 0.4\psi_0 = 0.3$ and the wave-train length $\Delta = 5\lambda\delta/(8\pi) = 145$ cm at a distance $L_0 = 4$ m from the wavemaker. The dependences of the train amplitude $|\psi|$ on coordinate η are shown in Fig. 10 for different time moments τ. The distance L from the wavemaker to the measurement point is determined by the relation $L = (4 + 0.29\tau)$ m. The moment $\tau = 0$ corresponds to the distance $L =$ 4m (Fig. 10a); $\tau = 6.8 - L = 6$m (Fig. 11b); $\tau = 13.6 - L = 8$m (Fig. 10c); $\tau = 20 - L = 10$m (Fig. 10d); $\tau = 26.8 - L = 12$m (Fig. 10e). One can see that first, the leading edge of the wave train is steepened (Fig. 10b), and then a short, intense pulse is initiated near the leading front (Fig. 10c, d). Comparing these numerical results with experimental data, one can see good agreement not only for the characteristic distance L_{st} of wave steeepening, but also for details of the packet envelope deformation. In particular, the leading front steepening distance is $L_{st} = 8$m both from the computations (Fig.10b), and the experiment (Fig. 9b) At larger distances, shorter pulses are formed on the leading front both in the numerical (Fig. 10d) and experimental (Fig. 9d) pictures, presumably as a result of the known modulation (Benjamin-Feir) instability. For smaller values of the wave-packet amplitude ($a \leq 2$cm), the steepening distance is too large (for $a = 2$cm, the theoretical value is $L_{steep} \simeq 12$m) to be observed experimentally in our tank.

For elucidation of the role of the induced current in the propagation of short intense gravity wave trains, we simulated Eq. (23) without the corresponding integral term. The result of the calculation for the same initial condition (24) as before ($\psi_0 = 0.75$, and $\delta = 4\pi$) is shown in Fig. 11 for the same time moments as those in Fig. 10. In the absence of the induced current, the modulation instability occurs at smaller times: $\tau \sim 20$, or $L \sim 10$m (Fig. 11d), while in the presence of the induced current, the corresponding values are larger: $\tau = 26.8$, $L = 12$m (Fig. 10d). Hence, the induced current tends to inhibit the modulation instability.

Thus, for deep-water gravity waves, the account of the third-order effects yields a good description of the experimentally observed effects concerning the shape and velocity evolution of a wave train, which cannot be described within the framework of the NLS. Note that for the stratified water, when internal waves occur, the third-order approximation effects can play a similar role in the interaction between surface and internal gravity waves.

2.2.3 Steady-state nonlinear solitary waves

An interesting problem in the form of a steady-state wave packet (envelope soliton) is too complicated for finding such a soliton analytically. Here, we accept a condition under which one can neglect two last terms in equation (16), which differs now from the NLS only by the nonlinear dispersion term in the left-hand side. This condition can be shown to be the following:

$$\frac{\omega_0}{8k_0^3\Delta^2} \ll \frac{5}{2}V_g^L k_0^2 \left|a\right|^2, \tag{25}$$

where Δ is the length of the wave packet. Now, Eq. (15) for the packet envelope is reduced to a simpler form (we use the dimensionless variables here):

$$2i\left(\frac{\partial\psi}{\partial t} + \beta\left|\psi\right|^2\frac{\partial\psi}{\partial\xi} + \mu\psi\frac{\partial\left|\psi\right|^2}{\partial\xi}\right) + \frac{\partial^2\psi}{\partial\xi^2} + \left|\psi\right|^2\psi = 0. \tag{26}$$

Note that Eq. (26) is the particular case of the more general nonlinear

$$2i\left(\frac{\partial\psi}{\partial t} + \beta\left|\psi\right|^2\frac{\partial\psi}{\partial\xi} + \mu\psi\frac{\partial\left|\psi\right|^2}{\partial\xi}\right) + q\frac{\partial^2\psi}{\partial\xi^2} + \alpha\left|\psi\right|^2\psi + i\gamma\frac{\partial^3\psi}{\partial\xi^3} = 0. \tag{27}$$

For $\beta = \gamma = \mu = 0$, Eq. (27) is the well-known NLS [22]; for $\alpha = q = 0$ and real function ψ, it is the modified Korteveg-de Vries equation [25, 23]. For $\mu = 0$ and $2q\beta = 3\gamma\alpha$, Eq. (27) was analyzed by Hirota [24]. All these cases were analyzed by the inverse scattering method [22], and exact $N-$soliton solutions of these equations were obtained. In Eq. (26), $2q\beta \neq 3\gamma\alpha$, and $\mu \neq 0$; i.e., it is not reduced to the above cases. Eq. (27) has the solution in the form of a phase-modulated soliton. To demonstrate this, we seek a solution of (26) in the form of a stationary traveling wave

$$\psi\left(\xi, t\right) = A\left(\xi - Vt\right)\exp\left\{i\Omega t + i\varphi\left(\xi - Vt\right)\right\}. \tag{28}$$

In variables

$$\rho = \zeta\sqrt{2\Omega - V^2},\ B = A\sqrt{\frac{1 - 2\beta V}{2\Omega - V^2}}, \tag{29}$$

Eq. (26), under zero conditions at infinity: $B\left(\zeta \to \pm\infty\right) \to 0$, and $B'\left(\zeta \to \pm\infty\right) \to 0$, has the soliton solution

$$B^2\left(\rho\right) = \frac{4}{1 + \left(1 + 16r/3\right)^{1/2}\cosh\left(2\rho\right)}, \tag{30}$$

$$\varphi(\rho) = \frac{V}{\delta}\rho - q\int\limits_{0}^{\rho} \frac{4d\,\hat{\rho}}{1 + (1 + 16r/3)^{1/2}\cosh\left(2\,\hat{\rho}\right)}, \tag{31}$$

where

$$r = \Theta\left(\beta - \frac{\Theta}{4}\right)\frac{(2\Omega - V^2)}{(1 - 2\beta V)^2},\ q = \frac{\Theta}{2}\frac{\sqrt{2\Omega - V^2}}{(1 - 2\beta V)},\ \delta = \sqrt{2\Omega - V^2}.$$

We see from (30) that the soliton exists for the values $r > -3/16$. The dependences of the packet envelope B and phase φ on the coordinate ρ for different values of r are shown in Fig. 12. Fig. 12a corresponds to the amplitude B, and b - phase φ for $q = r$. In both cases, curve 1 corresponds to the value $r = -2990/16000$, $2 - r = 0$, $3 - r = 2$. The soliton amplitude $B_0 = B(0)$ and soliton length Δ decrease with the growth of the parameter r. In the limit case $r = 0$ when the nonlinear dispersion is absent and $V = 0$, relations (30) and (31) correspond to the well-known NLS soliton without phase modulation [22]:

$$B(\rho) = \frac{\sqrt{2}}{\cosh(\rho)},\ \varphi(\rho) = 0. \tag{32}$$

However, for the modified soliton, when $r \neq 0$, there is the nonzero phase distribution. As should be expected for a conservative system, the soliton remains symmetric even in the presence of nonlinear dispersion.

The surface wave train dynamics considered above appears to be important for the description of a number of real situations, both of the "elementary" surface wave trains and of the "surface wave turbulence," which may consist of the chaotically distributed nonlinear wave trains.

2.3 Resonance effects caused by surface gravity-wave scattering by an underwater obstacle

The problem of surface wave scattering by underwater obstacles (bodies, bottom inhomogeneities) is a classical one in hydrodynamics. Various numerical [26, 27] and approximate analytical [28, 29, 30, 31] methods have been developed for its solution. We suggested one of these methods in earlier papers [30, 31]. The method is based on the assumption that the instant velocity field in the vicinity of an obstacle is quasi-stationary; i.e., it is close to the velocity field formed at its stationary streamlining. As is shown in [31], for submerged obstacles at $h > R$ (h is the submergence depth; R is the characteristic size of the body), this approximation is applicable over the entire wavelength range when calculating the scattered field. In this case, the problem of the surface wave scattering by an obstacle is reduced to the problem of wave radiation by an equivalent mass source, the intensity of which is determined by the velocity of fluid particles streamlining an obstacle and by the size of the latter.

The surface wave scattering by a small sphere towed with a constant velocity under a free fluid surface is considered here using this method. It is shown that singularities (when the wave amplitude logarithmically diverges along some isolated directions) occur in the scattered wave field under definite resonance conditions, and the resonant wave parameters are investigated. This result is somewhat analogous to that known in the theory of surface wave radiation by a source moving with the velocity U and oscillating with the frequency Ω. As is already known [27, 28, 32, 33, 34], at $\Omega \to g/4U$, the generated wave amplitude diverges in a three-dimensional case as $\ln|1 - 4\Omega U/g|$, while in a two-dimensional one as $|1 - 4\Omega U/g|^{-1/2}$. The solution for the case of $\Omega = g/4U$ is obtained in [27, 33, 35]. In [33], some additional restrictions are imposed on the spatial spectrum of the source that enables one to eliminate the divergence. The asymptotic behavior of surface waves for an oscillating source moving along the fluid surface for $\Omega = g/4U$ and $t \to \infty$ is obtained in [35], and it is shown that the generated wave amplitude grows in resonance. For a two-dimensional case, the surface wave scattering by an obstacle placed in a fluid stream is considered in [27]. Numerical calculations have shown that when approaching resonance, the reflected wave amplitude grows but remains limited and has the order of the incident wave amplitude.

Let us consider now a simple model: a small sphere of radius R_0 is towed at a depth h under the fluid surface with a velocity U in the positive direction of the x axis. The surface wave with an elevation $\zeta = a\cos(\Omega t - \mathbf{k}^0\mathbf{r})$ propagates at an angle Ψ to the sphere velocity direction. We consider the process of this wave scattering at the sphere. The fluid particle velocities in a wave are described by the formulae

$$\left.\begin{matrix} u \\ v \end{matrix}\right\} = a\Omega e^{k^0 z}\cos\left(\Omega t - k_x^0 x - k_y^0 y\right)\left\{\begin{matrix} \cos\Psi \\ \sin\Psi \end{matrix}\right. ,$$

$$w = -a\Omega e^{k^0 z} \sin\left(\Omega t - k_x^0 x - k_y^0 y\right) \tag{33}$$

Here k^0 is the wavenumber modulus, $k_x^0 = k^0 \cos\Psi$, $k_y^0 = k^0 \sin\Psi$, and $\Omega^2 = gk^0$ is given by the dispersion equation for surface gravity waves in deep water.

The intensity of dipole mass sources in the quasi-stationary approximation [31] is determined by the velocity (33), taken at the body trajectory $x = Ut$, $y = 0$, $z = -h$, and by its dimensions so that

$$q = -\left(\mathbf{p}\nabla\right) F\left(x, y, z, t\right), \tag{34}$$

where $\mathbf{p}$ is the dipole momentum: $p_x = Q\left(U - a_B\Omega \cos\Omega_1 t \cos\Psi\right)$, $p_y = -Qa_B\Omega \cos\Omega_1 t \sin\Psi$, $p_z = Qa_B\Omega \sin\Omega_1 t$, where $\Omega_1 = \Omega - k_x^0 U = \Omega - \Omega^2 U/g \cos\Psi$ is the wave frequency in the accompanying coordinate system, $a_B = ae^{-k^0 h}$ is the wave amplitude at the horizon h, $Q = 2\pi R_0^3$, and F is the function describing the scattering source geometry. Due to the smallness of the sphere diameter, it may be represented by a point source:

$$F\left(x, y, z, t\right) = \delta\left(x - Ut\right) \delta\left(y\right) \delta\left(z + h\right). \tag{35}$$

Then, the final form of the equivalent mass source is

$$\begin{gathered} q = -Q\left(U - a_B\Omega \cos\Omega_1 t \cos\Psi\right) \delta'\left(x - Ut\right) \delta\left(y\right) \delta\left(z + h\right) + \\ + Qa_B\Omega \cos\Omega_1 t \sin\Psi \delta\left(x - Ut\right) \delta'\left(y\right) \delta\left(z + h\right) - \\ -Qa_B\Omega \sin\Omega_1 t \delta\left(x - Ut\right) \delta\left(y\right) \delta'\left(z + h\right). \end{gathered} \tag{36}$$

Now, the potential of the scattered wave field is yielded as a result of solving the following set of equations:

$$\begin{gathered} \Delta\varphi = q\left(\mathbf{r}, z, t\right) \\ \varphi_{tt} + g\varphi_z = 0, \text{ for } z = 0 \\ \varphi \to 0, \text{ for } z \to -\infty. \end{gathered} \tag{37}$$

Therefore, the problem is reduced to finding radiation from a dipole mass source moving with velocity U and oscillating with frequency Ω_1. Such problems have been considered in the literature several times [28, 32, 33, 34, 35]. The difference is, according to formula (36), in our case, perturbations are represented by the sum of three dipole sources oscillating with the frequency Ω_1 which are "coordinated" by the incident wave field. When solving (37) by using the Fourier transformation, we obtain an expression for free surface displacement $\zeta = -\varphi_t/g$ in the form

$$\zeta = 2\pi i \int\limits_{-\infty}^{\infty} \frac{\omega q_s}{\omega^2 - gk} e^{i(\mathbf{kr}-\omega t)} d\mathbf{k} d\omega. \tag{38}$$

Here, q_s is the spatio-temporal spectrum of the sources, $q_s = q_{s1} + q_{s2}$, $q_{s1} = -\dfrac{ik_x UQ}{8\pi^3} e^{-kh} \delta\left(\omega - k_x U\right)$ corresponds to the uniform motion of a source, and q_{s2} takes into account source oscillations with the frequency Ω_1:

$$\begin{aligned} q_{s2} = \frac{Q\Omega a_B i e^{-kh}}{16\pi^3} &\left[\left(k_x \cos\Psi + k_y \sin\Psi - k\right)\delta\left(\omega - k_x U + \Omega_1\right) + \right. \\ &\left.\left(k_x \cos\Psi + k_y \sin\Psi + k\right)\delta\left(\omega - k_x U - \Omega_1\right)\right]. \end{aligned} \tag{39}$$

The waves radiated by a uniformly moving source satisfy the Cherenkov condition $\omega = k_x U$. These are well-known Kelvin ship waves [29, 32], and we shall not deal with them below. The resonance effects are caused by source oscillations with the frequency Ω_1. Here, the source (39) radiates both slower and faster waves with $k_x = \dfrac{\omega \pm \Omega_1}{U}$. These are waves of anomalous and normal Doppler frequencies, respectively [36].

By substituting (39) in (37), making integration with respect to k_x and k_y, and introducing dimensionless variables $\omega' = \omega U/g$, $\Omega_1' = \Omega_1 U/g$, $x_1' = (x - Ut)\, g/U^2$, $y' = yg/U^2$, $t = tg/U$ (primes are omitted further), we obtain the following approximation for ζ:

$$\zeta = \frac{Qa_B i g^2 \Omega}{4\pi U^5} \sum_{l=\pm 1} e^{-i\Omega_1 l t} \int \frac{\omega^3 \left[(\omega - \Omega_1 l)\cos\Psi + \sqrt{\omega^4 - (\omega - \Omega_1 l)^2}\sin\Psi + \omega^2 l\right]}{\sqrt{\omega^4 - (\omega - \Omega_1 l)^2}}$$

$$\exp\left\{-\frac{\omega^2}{Fr^2}+i\left[\left(\omega-\Omega_1 l\right)x_1+\sqrt{\omega^4-\left(\omega-\Omega_1 l\right)^2}y\right]\right\}d\omega. \tag{40}$$

Here, $Fr=\dfrac{U}{\sqrt{gh}}$ is the Froude number. The integration limits are chosen here from the condition of real values of the wave vector transverse component k_y; i.e.,

$$\omega^2-\left(1-\frac{\Omega_1 l}{\omega}\right)^2\geq 0,\omega>0. \tag{41}$$

The solution of this inequality yields admissible frequency intervals of radiated waves. If $\Omega_1>1/4$, then $\omega>\omega_1=\dfrac{1+\sqrt{1+4\Omega_1}}{2}$ for $l=-1$, and $\omega>\omega_4=\dfrac{\sqrt{1+4\Omega_1}-1}{2}$ for $l=1$. If $\Omega_1<1/4$, then $\omega>\omega_1$ for $l=-1$, while for $l=1$, there are two admissible intervals: $\omega>\omega_2=\dfrac{1+\sqrt{1-4\Omega_1}}{2}$ and $\omega_4<\omega<\omega_3$, where $\omega_3=\dfrac{1-\sqrt{1-4\Omega_1}}{2}$. Therefore, the expression for ζ at $\Omega_1<1/4$ has the form:

$$\zeta=\zeta_0\,\mathrm{Re}\left\{e^{-i\Omega_1 t}\left[\int\limits_{\omega_4}^{\omega_3}f_1\left(\omega\right)e^{i\phi_1(\omega)}d\omega+\int\limits_{\omega_2}^{\infty}f_1\left(\omega\right)e^{i\phi_1(\omega)}d\omega\right]+\right. \tag{42}$$

$$\left.e^{i\Omega_1 t}\int\limits_{\omega_1}^{\infty}f_{-1}\left(\omega\right)e^{i\phi_{-1}(\omega)}d\omega\right\}.$$

Here,

$$\phi_l=\left(\omega-\Omega_1 l\right)x_1+\sqrt{\omega^4-\left(\omega-\Omega_1 l\right)^2}y \tag{43}$$

$$f_l=\frac{i\omega^3\left[\left(\omega-\Omega_1 l\right)\cos\Psi+\sqrt{\omega^4-\left(\omega-\Omega_1 l\right)^2}\sin\Psi+\omega^2 l\right]}{\sqrt{\omega^4-\left(\omega-\Omega_1 l\right)^2}} \tag{44}$$

$$l=\pm 1,\zeta_0=\frac{Qa_Bg^2\Omega}{4\pi U^5}.$$

It is seen from (42)-(44) and expressions for ω_1 to ω_4 that at $\Omega_1 = 1/4$, $\omega_2 = \omega_3 = 1/2$, and the first two terms in (42) become logarithmically divergent. Note that the function $\partial\zeta/\partial y$, the surface slope in the transverse direction with respect to the source motion, does not have such a singularity.

We consider the incident wave parameters in resonance:

$$\Omega - \Omega^2 \cos\Psi = \frac{1}{4}$$

or

$$\Omega = \frac{1 \pm \sqrt{1-\cos\Psi}}{2\cos\Psi}. \tag{45}$$

Thus, if a wave and inhomogeneity move in the same direction ($\cos\Psi = 1$), we have $\Omega = 1/2$, or in dimensional variables, $U = g/2\Omega = c_g$ (c_g is the group velocity of surface waves); i.e., the incident wave is in group resonance with the source. For the counter-running motion ($\cos\Psi = -1$,) U =0.4c_g when a wave is incident at a normal angle U=0.5c_g. For an arbitrary angle $\cos\Psi > 0$, there are two values of the resonant frequency, while for $\cos\Psi < 0$, there exists one value. The dependence of the resonant wave frequency on its incidence angle is shown in Fig. 13.

Now, we deal with the scattered wave field geometry in the accompanying coordinate system $x_1 = R\cos\theta$, $y = R\sin\theta$. Thus, using the stationary phase method, we obtain from (43) and the condition $\phi'_\omega = 0$:

$$\tan\theta = \frac{\sqrt{\omega^4 - (\omega - \Omega_1 l)^2}}{\omega - \Omega_1 l - 2\omega^3}. \tag{46}$$

Hence, each frequency is radiated at its definite angle θ. The radiated wave frequency versus the angle θ for $\Omega_1 = 0.1$ and 1 is given in Fig. 14, and the phase pattern of scattered waves in the case $\Omega_1 = 0.1$ is shown in Fig. 15. It is seen that at $\Omega_1 < 1/4$, the latter represents a set of "ring" waves distorted by a translation velocity of the source motion as well as ship waves split into two sets because of source oscillations. Phase pictures of waves radiated by an oscillating source are thoroughly discussed in [32].

In the resonance case $\Omega_1 = 1/4$, $\omega = 1/2$, we have from (46):

$$\begin{gathered} \tan\theta = \pm\sqrt{2} \\ \theta = 54.7^\circ, \end{gathered} \tag{47}$$

and the resultant phase picture in the plane x_1, y will have the form schematically shown in Fig. 16. The resonant wave frequency satisfies the ratio

$$U = \frac{g}{2\omega} = c_{gr}; \tag{48}$$

i.e., the group velocity of a scattered wave equals to the source motion velocity. The reradiated wave does not move away from the source, and its energy is stored in the directions (47).

Note that in this statement, there is at least one resonant frequency for any incidence angle, and in this sense, all the wave incidence angles are equivalent. If scattering takes place at obstacles of finite sizes, for example, the length L at the x axis, then by substituting (35) by the distribution

$$F(x, y, z, t) = \delta(y)\,\delta(z + h)\,\frac{1(x + L/2 - Ut) - 1(x - L/2 - Ut)}{L} \tag{49}$$

where $1(x)$ is the Heavyside unit function, we obtain that the additional term $\dfrac{\sin(\omega - \Omega l)\,L/2}{(\omega - \Omega l)\,L/2}$ will be included in expression (40), which achieves its maximum at $\omega = \Omega$. As seen from (45) and (48), this equality is fulfilled only in the case of the co-running wave and source. Thus, the allowance for finite sizes of the source leads to a conclusion that the most intensively scattered waves among the resonant waves statisfying (45) are those propagating in the same direction as the source.

The results obtained above for the surface wave scattering by a submerged body enables one to calculate the domain of parameters for which the incident wave is resonant, the geometry of a scattered wave field, and their other kinematic characteristics. In this formulation, the scattered wave amplitude in resonance tends to infinity. To evaluate the perturbation values for these directions, a more detailed analysis of the problem is necessary. Numerical calculation results for the two-dimensional problem [27] show that the wave amplitude grows in resonance, but remains limited and amounts to a value of the order of the incident wave amplitude.

3 Experimental Studies

3.1 Laboratory experiments on surface wave transformation on a inhomogeneous flow around a sphere

The study of the surface wave transformation by the inhomogeneous subsurface flows is of primary interest in connection with the remote sensing methods of ocean monitoring. It is not an easy matter to carry out the related field experiments, such as a detailed recording of surface wave transformation by an inhomogeneous flow over a bottom elevation or around a moving object. Thus, laboratory experiments seem to be of high importance at the present stage of research. A laboratory experiment described in [1] dealt with an effect of a flow, inhomogeneous along its direction, on the characteristics of a counter-running surface wave.

This subsection deals with the results of laboratory studies of the surface wave amplitude variability under the action of a flow created by a moving sphere with a comparison of the experimental data with the results of related theoretical calculations made using the model described in the previous Memorandum [2].

3.1.1 Experimental method

Experiments were carried out in a large tank, in which an area 10 m x 2 m was used for our purposes. A schematic of the experiment is shown in Fig. 17. Quasi-harmonic surface waves of a frequency f were generated by the wavemaker (1) placed at one end of the tank and were absorbed by wave absorber (7) at the other end of the tank. Sphere (6) of a radius r was fixed at the end of a narrow streamlined knife and was submerged at a depth h (a distance from the unperturbed water surface to sphere center). The knife was attached to a trolley (5) moving it along the tank from left to right with the velocity V=0.4 m/s. A rod with acoustic sensors of water-surface deviation was placed across the tank. The acoustic sensors developed in our Institute are based on the ultrasound location phase method of measuring reflecting surface movements in a continuous regime of ultrasound wave radiation. The rod was located at a distance R from the point where the trolley gained the velocity V (R is slightly less than the distance from the rod to the wavemaker). The instant of a knife intersecting the sensor plane was recorded by a special contact marker. In the experiments we used two water surface deviation sensors placed at different distances from the tank axis. Data of the sensors and the contact marker of the sensor plane intersection by a sphere were recorded by an IBM PC computer.

The aim of the experiments was to determine the spatial structure of surface wave amplitude anomalies in the vicinity of the sphere. This problem was solved in the following way:

- Based on the assumption that the parameters of the surface wave anomalies do not significantly change during the time τ when they pass the acoustic sensors ($\tau \approx 5$ s), the recorded time variations of the surface wave amplitude were converted into the dependence of the surface wave amplitude on the coordinate directed along the tank axis (the x axis).
- After sphere motion ceased, the acoustic sensors were shifted by 0.1 m, and a new realization was recorded. Therefore, using the contact marker data, we could combine the data of several experimental realizations and obtain spatial distribution of surface wave characteristics in the xy plane (y is the coordinate across the tank).

17 sets of experimental parameters for which spatial distributions have been obtained are listed in Table 1 (see the end of this section).

An image taken by a TV camera (4) during the experiments was recorded on an IBM PC. Black cable (8) laid across the tank was in the view field of the camera, which could be used to calculate surface wave slopes. Processing of data yielded by telecamera is at the initial stage now, and thus only data of the acoustic sensors are analyzed in the present report.

3.1.2 Experimental results and their comparison with theoretical calculations.

First, the surface wave parameters were measured without a knife, and then with a moving knife but still without a sphere. These experiments have demonstrated a slight inhomogeneity of the surface wave amplitude distribution across the tank, as well as the fact that the knife itself does not noticeably alter the surface wave field.

Spatial distributions of the surface wave amplitude for the parameter sets no. 1-3 (Table 1) are shown in Fig. 18, and for no. 6-8 in Fig. 20. The horizontal axis in these figures corresponds to the x axis, and the vertical to the y axis. Surface deviations were measured only on one side of the tank axis, so that the second half of the figure is obtained by reflection with respect to the tank axis. The axes are increase in centimeters; the position of the sphere center in Fig. 18 corresponds to the point x=400, y=0, and in Fig. 20 x=700, y=0. Data on the y axis are given only up to y=75 cm, because data from more remote sensors are strongly distorted by flow inductor walls. The values of the relative variation of the surface wave amplitude A are shown in the figures by colors. In each experimental realization, the surface wave amplitude was normalized by its value in the region remote from surface anomalies (the region of unperturbed amplitudes was chosen at realization obtained at 10-20 s before the sphere passes by the acoustic sensors). Variation of A is shown by color in accordance with the scale presented to the right of the spatial distribution. Note that in Fig. 18 and Fig. 20, the limits of the color scales are different.

As seen from Figs. 18 and 20, spatial structures of surface wave amplitude anomalies essentially depend on the surface wave frequency f. Thus, in distributions 1 and 6 (f=1.73 Hz, the group velocity of surface waves $V_g > V$), the region of A decrease is shifted forward with respect to the sphere. In distributions 2 and 7 (f=2.02 Hz, V_g is slightly less than V), this region is practically above the sphere; while in distributions 3 and 8 (f=2.29 Hz, $V_g < V$), the region of the A decrease is shifted back with respect to the sphere. For f=1.73 Hz and f=2.29 Hz, one region of increased A is particularly pronounced in both figures; in the former case, it is situated mainly to the left of the sphere, while in latter cases to the right. In distributions 2 and 7, there are regions of larger A both before and after the the sphere.

Analogous spatial structures of surface wave anomalies were obtained from theoretical calculations. In the reference system moving with the sphere, we deal with a physical situation comparable to that considered in the previous memorandum ([2]). Some results of theoretical calculations for values of the parameters involved in distributions 1-3 and 6-8 are given in Figs. 19 and 21. Arrangement of regions of larger and smaller A basically corresponds to the experimental data. The main difference between theoretical and experimental results is observed in the rear areas: for $x < 300$ in Figs. 18 and 19 and for $x < 580$ in Figs. 20 and 21. Essential anomalies of surface waves in these regions observed in the experiment are, evidently, due to the surface wave transformation at a turbulent wake of a moving sphere. This effect is not taken into account in the developed model, and in Figs. 19 and 21, the A variation at $x < 300$ and $x < 580$ is inessential.

Let us consider the dependence of the A variations on the frequency f. As a characteristics of A variability, we have taken the value δA equal to the difference between the maximum and minimum values of A over the entire distribution. In distributions 1-3 and 15-17, the maximum value of δA is observed for f=2.02 Hz, when the group velocity of surface waves is close to V. In distributions 4-8, δA grows with increase of f. Note, that at frequencies f=1.02 Hz and 1.30 Hz, surface wave anomalies caused by sphere motion have not been recorded at all. That is why distributions 4 and 5 are not given in Fig. 20. In distributions 9-11 and 12-14, A only slightly depends on f.

Theoretical calculations yield for δA 3-7 the values 3-7 times less than in the experiment. In Figs. 19 and 21, the limits of color scales differ from those in Figs. 18 and 20. In our opinion, the cause of this discrepancy is the difference between the real field of sphere streamlining and the dipole field assigned in calculations. To elucidate this problem in order to find a solution, additional experiments should be carried out. According to the theoretical calculations, the dependence of δA on f is weak in the frequency range 1.73 Hz - 2.29 Hz. (The variation δA amounts, on average, to 10%.) At frequencies 1.02 Hz and 1.30 Hz, the value of δA is very small (0.01 and 0.05, respectively). Comparison of distributions 1-3 with 6-8 and 9-11 with 12-14 enables one to draw some conclusions regarding the character of surface anomaly development with increase of R. The sizes of the spatial region above the sphere increase. Thus, the distance between the characteristic surface anomaly structures L for R=7 m are, on average, 0.3 m larger than for R=4 m. Similar results follow from theoretical calculations. The value δA for R=7 m is, on average, 80% larger than for R=4 m. Theoretical calculations also yield an increase of δA of 40%.

The character of the dependence of A variability on h can be considered by comparing distributions 1-3 with 9-11 and 6-8 with 12-14. With an increase of h from 0.3 m to 0.45 m, the distance L grows, on average, by 0.2 m. In theoretical calculations, this effect is absent; L is practically independent of h. Regarding the value of δA, in the experiment with h=0.45, it is, on average, 1.6 times less than for h=0.3 m. A more rapid decrease of δA (2.8 times) with the same growth of h is observed in theoretical calculations.

3.1.3 Conclusion

Our experiments have shown that the structure of the surface wave anomalies caused by the flow around a submerged sphere strongly depends on the surface wave frequency. On the other hand, such structures depend only slightly on the sphere depth. The surface wave amplitude essentially changes only in a limited range of surface wave frequency f close to $g/4\pi V$, where V is the sphere motion velocity; these changes are stronger for smaller submersion depths. This is a demonstration of the role of the group synchronism described in the previous Memorandums [37, ?].

The results of theoretical calculations agree with the experimental data in what concerns the disposition of regions of the surface wave amplitude increase and decrease. At the same time, they yield essentially smaller values of surface wave amplitude variation than those recorded in the experiment. This may be due to the difference between the real flow around the sphere and the dipole approximation and to the assumption of surface wave linearity adopted in theoretical calculations. The dependences of the surface wave amplitude variation on sphere motion time and its submersion depth in theoretical calculations are close to those obtained in experiments.

Further, the plan is to develop the theoretical model in several areas: taking account of nonlinear effects in surface waves, which will result in a stronger surface-wave amplitude variation; investigation of surface wave transformation for the case when surface waves have lengths of the same order with characteristic sizes of flow inhomogeneity; and a more correct description of sphere-created flow.

Table 1. Sets of parameters used in the experiment.

Set number	r(mm)	h(m)	R(m)	f(Hz)
1	75	0.3	4	1.73 ±0.03
2	75	0.3	4	2.02 ±0.03
3	75	0.3	4	2.29 ±0.03
4	75	0.3	7	1.02 ±0.02
5	75	0.3	7	1.30 ±0.02
6	75	0.3	7	1.73 ±0.03
7	75	0.3	7	2.02 ±0.03
8	75	0.3	7	2.29 ±0.03
9	75	0.45	4	1.73 ±0.03
10	75	0.45	4	2.02 ±0.03
11	75	0.45	4	2.29 ±0.03
12	75	0.45	7	1.73 ±0.03
13	75	0.45	7	2.02 ±0.03
14	75	0.45	7	2.29 ±0.03
15	42.5	0.17	7	1.73 ±0.03
16	42.5	0.17	7	2.02 ±0.03
17	42.2	0.17	7	2.29 ±0.03

3.2 Laboratory measurements of gravity-capillary wave curvature

The wavy water surface curvature is an important characteristic of wind waves, which should be known, in particular, for constructing models of radar and optical signal reflections from the sea surface. The hydrodynamic aspect of gravity-capillary wave curvature investigations is related to the formation mechanisms of a small-scale part of the wind-wave spectrum and to the study of strongly nonlinear waves and their stability. Wind-wave curvature was investigated under field and laboratory conditions using a method based on the light focusing effect caused by its reflection from a wavy water surface [38, 39, 40, 41, 42, 43]. The curvature radii measured in these works correspond to the region of very small values of, primarily, the capillary part of the wave spectrum. Only the modulus of the curvature radii was measured, which did not enable one, for example, to distinguish differences in wave crest and trough curvatures and, thus, to make a judgment regarding the wave profile. At the same time, in strongly nonlinear waves, the profile is asymmetric and is characterized by the presence of sharp crests. Hence, it is necessary to separate positive and negative curvature values. This is helpful, in particular, for investigation of the capillary-gravity ripple generation (the so-called parasitic ripple) on the crests of longer gravity waves [44, 45, 46, 47, 48]. Since the parasitic ripples contribute considerably into the formation of the wind-wave spectrum, of special interest is the study of decimeter-range wave profile curvature and the influence of capillary-gravity ripple generation on statistics of wind-wave curvature.

Here, the first attempt is made to investigate the curvature of decimeter-range surface waves, both those of small amplitude and strongly nonlinear ones characterized by ripple generation at their profile. The experimental scheme and the method of data processing have been designed to provide distribution functions for wave crest and trough curvatures, to demonstrate an increase of gravity-wave profile asymmetry with the growth of their amplitude, and to illustrate the parasitic ripple generation on their slopes. Analysis of distribution function for time intervals between neighboring crests and troughs has enabled us to find out that, besides the previously investigated high-frequency parasitic ripple generated at the front slopes of decimeter waves, a lower-frequency component is observed on their rear slopes.

3.2.1 Experimental setup

Wave curvature on a water surface was measured in the oval wind-wave tank (see the first Memorandum [?]), having two semicircular sections of radius 2 m and two straight-line sections of length 2 m. The channel width is 30 cm, the water depth is 25 cm, and the aerochannel height is 35 cm. The first experimental run was devoted to measurements of surface gravity waves of various amplitudes excited by a mechanical wavemaker at a frequency close to 4 Hz (the corresponding wavelength is of the order of 10 cm). The measurements were carried out at a distance of 70 cm from the wavemaker for four regimes, with wavemaker oscillation amplitudes 1.5, 2, 3, and 4 mm. The first two regimes correspond to small-amplitude waves with a quasi-sinusoidal profile, regime 3 corresponds to an amplitude critical for the parasitic capillary ripple generation onset at a gravity wave profile, and regime 4 corresponds to a strongly nonlinear gravity wave with developed parasitic ripples. In the second experimental run, the wind-excited wave curvature was investigated for two wind velocities: 2.2 m/s and 4 m/s. The wind-wave fetch amounted to 6 m. In the "weak-wind" regime ($V = 2$ m/s), there were generated small-amplitude wave trains with a narrow frequency spectrum (the characteristic wave frequency is 5-6 Hz), and parasitic high-frequency ripple has not been observed in this regime. In the moderate-wind regime (4 m/s), energy-carrying waves had a frequency of 3-4 Hz and were characterized by essential steepness. Developed small-scale ripple was observed on their slopes.

A scheme of the laboratory setup designed for measuring surface wave curvature is displayed in Fig. 22. The setup includes a laser, a beam formation system, and a photoreceiver. The laser and the beam formation system are located under a transparent bottom of the wind-wave tank; a defocusing lens varies the initial beam divergence. The photoreceiver has a narrow slot diaphragm oriented along the tank. The diaphragm sizes are chosen so that the width of the diaphragm is less than the beam width in the receiver plane, whereas the slot length is larger than possible beam deviations in the transverse direction, all of which enables one to measure the wave curvature averaged over the transverse coordinate.

3.2.2 Method for wave-curvature measurement

Let a laser beam pass from water to air through a wavy surface. If the surface slope is such that after refraction, the beam reaches the receiver diaphragm (in the particular case, when a source and a receiver are arranged coaxially, a beam passes through surface without refraction), the signal on the receiver is determined by the beam width which, in its turn, depends on the surface curvature at the refraction point. When passing through other parts of the surface, the beam reaches the diaphragm, and the signal is nonzero. Thus, the signal has a character of pulses. An example of temporal record for regular waves (regimes 1 and 4) is shown in Fig. 23. If the beam width at the receiver plane is larger than the slot size, then for the case when the beam passes through a surface portion without refraction, the light power P_l recorded by the photoreceiver for a wavy surface is related to the power P_0 for a smooth surface in the following way:

$$P_l = P_0 \frac{|\Delta_0|}{|\Delta_l|}. \tag{50}$$

Here, Δ_0 and Δ_l are the beam widths at the receiver plane in the longitudinal direction for the cases of a smooth and a wavy surface, respectively. The value of Δ_l in (50) can be written as

$$\Delta_l = r - (H - \xi)\tan\left[\arcsin\left(n\left(\sin\varphi_n - \varphi_0/n\right)\right) - \varphi_n\right],$$

$$\varphi_n = \sin^{-1}(r/R), \tag{51}$$

where r is the half-width of the light spot on the water surface, φ_0 is the beam divergence at the ouput of the beam formation system, R is the curvature radius (R^{-1} is the curvature) of the surface at the intersection point of the surface and the laser beam, H is the receiver location height above the average water level, ξ is the surface deviation from the average level, and n is the water refractive index. Expression (50) is approximate and can be used if the beam size for any R is essentially larger than the slot. For the case when $r/R \ll 1$ and $\xi \ll H$, one can easily obtain from (50) and (51) the expression for the surface curvature radius:

$$R = \frac{r\,(n-1)\,H/\Delta_0}{1 - P_0/P_l},\ R < 0, R > r\,(n-1)\,H/\Delta_0, \tag{52}$$

$$R = \frac{r\,(n-1)\,H/\Delta_0}{1 + P_0/P_l},\ 0 < R < r\,(n-1)\,H/\Delta_0. \tag{53}$$

It follows from here that the curvature may still have more than one value. Hence, it is necessary to eliminate this ambiguity by selecting appropriate parameters of the system or by providing additional information on the assumed value of surface curvature in order to choose one of two formulae (52) or (53). Ambiguity in the curvature modulus can be eliminated if Δ_0 is small. This corresponds to the case when troughs and crests defocus the beam. For larger surface curvatures, $|R| \ll r\,(n-1)\,H/\Delta_0$, we have from both (52) and (53)

$$|R| = r\,(n-1)\,H/\Delta_0 \frac{P_0}{P_l}; \tag{54}$$

i.e.; unambiguous determination of the modulus curvature is possible. Note that the surface curvature distribution in the region $0 < |R| < r\,(n-1)\,H/\Delta_0$ can be obtained by processing only pulses with $P_0/P_l \gg 1$ in signal records.

Nothing can be said about small curvatures when $P_0 \sim P_l$, if such curvatures are present.

Formula (52) describes a situation in which a beam is either defocused by the surface ($R < 0$) or focused with formation of a focus above the receiver location ($R > r\,(n-1)\,H/\Delta_0$). Formula (53) corresponds to a situation in which the beam is focused by the surface with formation of a focus below the plane of the receiver location ($0 < R < r\,(n-1)\,H/\Delta_0$). If it is known beforehand that only small curvatures, $|R| > r\,(n-1)\,H/\Delta_0$, exist on the water surface, then

$$R = \frac{r\,(n-1)\,H/\Delta_0}{1 - P_0/P_l}. \tag{55}$$

This situation does really occur if waves are gentle and the initial beam is defocused. In this case, the surface parts with negative curvature (local trough) defocus the beam even more strongly, and the parts with positive curvature (local crests) narrow the beam with formation of convergence above the receiver plane. As distinct from formula (54), formula (55) yields not only the modulus but also the sign of the curvature. If it is known beforehand that the surface curvatures are so large that the beam is either defocused or focused with formation of a focus below the plane of the receiver location, then by applying alternately formula (52) to one pulse in Fig. 23 and (53) to the next pulse, etc., one can obtain the curvature distribution with its sign.

Besides the information on the surface curvature distribution at points of a definite slope, the signal records of the photoreceiver carry information on temporal wave characteristics. For a quasi-periodic wave, the time interval between three neigboring pulses corresponds to the wave period. The distribution function for the intervals between pulses enables one to make a judgement about the presence of waves of the given frequency in the wave spectrum and, in particular, about the occurrence of high-frequency parasitic ripple on lower-frequency gravity waves.

3.2.3 Measurement results

1. Regular waves Histograms of pulse brightness amplitudes of a beam passed through points of zero slope surface for wavemaker oscillation amplitudes 2 mm and

4 mm are presented in Fig. 24a and Fig. 25a. For small wave amplitudes

(Fig. 24a), the vicinities of troughs (the curve to the left of the arrow indicating the brightness value for a smooth surface) defocus the beam, while the crests (the curve to the right of the arrow) focus the beam above the receiver plane, which enables one to use formula (55) in surface curvature calculation. For small wave amplitudes, the curves to the left and the right of the brightness value for a smooth surface diverge into different sides when the amplitude increases. Figure 24b demonstrates the absence of ripples in this case: there are only two points with zero slope on the wave period corresponding to a crest and trough of the wave. Time intervals between neighboring crest and trough and trough and crest are close to each other, which yields two practically coinciding peaks near the point t=0.14 s; the total time interval for these peaks is, evidently, equal to the fundamental wave period.

A histogram of beam brightness for strongly nonlinear waves (regime 4) is given in Fig. 25a. As might be expected, the curve is shifted to the left, which corresponds to larger surface curvatures. In this situation, only those points with zero surface slope exist which either defocus the beam or focus it below the receiver location. As seen from Fig. 25b, the peaks corresponding to time intervals between neighboring crests and troughs of the wave are separated more strongly than in the previous case; the latter means growth of steep wave slope asymmetry with increase of its amplitude. In this regime, ripple having the frequency of the order of 60-70 Hz was excited on crests of fundamental waves, which is illustrated by an additional peak in Fig. 25b in the region of small time intervals of order 0.007 - 0.01 s. The obtained ripple values agree with those measured earlier in [45].

Let us consider now the surface curvature distributions at zero slope points for all four regimes of wavemaker operations shown in Fig. 26. Histograms in Fig. 26a, b are obtained when processing a signal with formula (55); histograms in Fig. 26c, d are yielded by applying formulae (52) and (53) alternately to neighboring pulses. It is seen from Fig. 26 that the surface curvature increases with the wave amplitude growth, the curvature values at crests and troughs increasing differently. If at small wave amplitudes, the average surface curvature in the positive and negative regions is approximately the same, for larger amplitudes, the curvature at crests ($R > 0$) increases essentially faster than at troughs ($R < 0$) (see Fig. 26b, c). Note that maximum crest curvature distribution for waves of an amplitude close to the critical one for parasitic ripple generation (regime 3) corresponds to the curvature value obtained in another way in [46]. For strongly nonlinear waves (regime 4) to the right and left of principal maxima of the curvature distribution in the region of $60m^{-1}$, the second maxima appear due to ripple (Fig. 26d).

Now, we consider the measurement results for surface wave slopes. In these measurements, the receiver was shifted in the horizontal plane to the left or right with respect to its position in the coaxial observation scheme, so that a laser beam reaching the receiver was refracted by the surface at points with assigned positive or negative slope. At small amplitudes (regimes 1 and 2), there are only two points with a fixed slope of the surface, which indicates the absence of high-frequency ripple. For increased wave amplitude (regime 3), the number of points on the surface of a given slope grows both on the front and rear slopes; in time histograms (Fig. 27), a maximum appears in the region of small time intervals that is caused by ripple generation. The position of the maximum in Fig. 27a associated with the presence of parasitic ripple at the front slope of the fundamental wave corresponds to the value t = 0.007 s, and at the rear slope (Fig. 27b) $t = 0.012$s. Maxima for $t = 0.25$ s in Figs. 27a, b are, evidently, due to an asymmetric arrangement of points with assigned slope at the wave profile (observed by a receiver displaced from the coaxial position) and yield totally with the maximum position for t = 0.25 s, that is the fundamental wave period. Therefore, it follows from Fig. 27 that together with the known (see [44, 45, 46, 47, 48]) high-frequency parasitic ripple at front slopes of a steep decimeter wave, there arises a lower-frequency ripple at its rear slopes. Note that in regime 3 the number of points with zero slope remains the same (two in a period, see Fig. 27c). This indicates that for wave amplitudes slightly exceeding the critical value, the parasitic ripple slope at the front and rear slopes is less than the fundamental wave slope.

At a further increase of wave amplitude (regime 4), the ripple slope increases, and at some parts, it becomes larger than the fundamental wave slope. This is illustrated in Fig. 25b, where in regime 4 at zero slope points in the time histogram, there is a maximum corresponding to the small-scale parasitic ripple (there is no such maximum in regime 3). Histograms of time intervals for the front and rear slopes of a strongly nonlinear wave (regime 4) are shown in Fig. 28a, b respectively, indicating the presence of ripple on both wave slopes as in regime 3. However, the histogram in Fig. 28b has a more complicated form, revealing essential "splitting" of all maxima described for the case of Fig. 27b, i.e., the presence of more than two points with a given slope at the rear wave slope in addition to the ripple. These peculiarities of the strongly nonlinear decimeter wave profile require a further investigation.

2. Wind waves The peculiarities of mechanically generated periodic waves described above can, to a large extent, be transferred to the case of wind waves. Figures 29 and 30 exhibit histograms of pulse signal amplitudes of a receiver and histograms of time intervals between pulses for wind waves at the wind velocities $V = 2.2$ m/s and $V = 4$ m/s, respectively.

Histograms of signal amplitudes at weak wind (Fig. 29a) are characterized by two maxima located at different sides from the signal value corresponding to a smooth water surface. This case is close to the examples of regular gravity waves of small amplitude considered above, when the wave curvature was rather low and the signal value unambiguously corresponded to wave crests and troughs; the amplitude distribution was of the bimodal character (see Fig. 24a). It is also seen in the histogram of time intervals (Fig. 29b) that pulses with periods corresponding to energy-carrying gravity waves prevail in the signal, while the contribution of high-frequency ripple (the left maximum in Fig. 29b) is not large.

The wave character for the wind velocity $V = 4$ m/s is close to the above regimes of strongly nonlinear gravity waves. In this case, the amplitude histogram is shifted to the region of values corresponding to larger curvatures; here, the signal values from crests and troughs lie in overlapped regions, and the distribution bimodality is not observed (compare with Fig. 25a for a regular strongly nonlinear wave with ripple). It also follows from comparison of Figs. 29a and 25a that larger curvature values are observed in wind waves than in regular gravity waves in the presence of capillary ripple. This is, evidently, due to both the wind influence on parasitic ripple generation and the free capillary ripple generated directly by wind on the water surface. The essential contribution of high-frequency ripple at stronger wind is also illustrated by the histogram of time intervals (Fig. 30b), in which a peak at small-scale ripple frequencies dominates over the region of energy-carrying frequencies. Therefore, it can be concluded from Fig. 30b that for developed wind waves, statistical curvature characteristics are determined by high-frequency ripple; this conclusion agrees with those made earlier in [39, 40]. Note that the peak shown in Fig. 30b corresponds to characteristic ripple frequencies close to the frequencies of parasitic capillary ripple excited by steep decimeter waves. The question on the relationship between the energy of the parasitic ripple generated by decimeter waves and the free ripple generated directly by wind needs special analysis.

3.2.4 Conclusion

Let us briefly formulate the main results of this section.

Laboratory measurements of surface wave curvature have been carried out using a defocused laser beam. The method of measuring and processing the results suggested here has permitted us, for the first time, to separate curvature values on crests and troughs of gravity waves and construct a curvature distribution with account of its sign.

It has been determined that for growing amplitudes of regular decimeter-range waves, the curvature on crests increases essentially faster than on troughs. At rather large wave amplitude, this leads to generation of high-frequency ripple. In this case, together with the known capillary parasitic ripple propagating along the front slope of a decimeter wave, a lower-frequency ripple is recorded at the rear slope of the decimeter wave.

It has been shown that curvature characteristics of wind waves for a weak wind are analogous to the characteristics of weakly nonlinear regular decimeter waves with a quasi-sinusoidal profile and small curvature of crests and troughs; the influence of high-frequency ripple on wave curvature is small. For stronger waves, the surface curvature is primarily determined by high-frequency ripple.

Investigation of the relative contribution made to ripple energy by mechanisms of parasitic ripple generation and the free ripple generated directly by wind is of special interest, and it is planned to carry it out further.

3.3 Experimental investigation of surface wave damping by small-scale turbulence

3.3.1 Background

The gravity surface-wave damping by turbulence was investigated more than once, both theoretically and experimentally (see [53, 54] and references therein). Two damping mechanisms of surface waves propagating in a turbulent medium were considered theoretically. The first is wave scattering by turbulent pulsations (convective motions), which results in the mean field attenuation. The second mechanism is related to the turbulence transformation by orbital velocity gradients in a wave, which leads to wave energy transfer to the turbulence and can be considered as "turbulent viscosity" effect. The relationship between these two mechanisms is not quite clear now. It can only be assumed that wave scattering is effective in the case when the turbulence scales are comparable to or larger than the surface wave length, by analogy with electromagnetic wave scattering at refractive index inhomogeneities. In the case of small-scale turbulence, the "turbulent viscosity" mechanism, probably, prevails; in this case, one should distinguish between the damping at "external" turbulence and the damping at the turbulence generated by the wave itself as a result of its breaking. The latter case corresponds to nonlinear effects in a wave and can be significant only for large-amplitude gravity waves.

A common approach to the problem of wave-turbulence interaction is based on the semi-empirical equations with the appropriate closure hypotheses. n particular, the turbulent viscosity coefficient in a wave of frequency ω, can be estimated as

$$\nu_t \sim \left\langle u_t'^2 \right\rangle / \omega, \tag{56}$$

where $\langle u_t'^2 \rangle$ denotes the average of the squared velocity of turbulent pulsations.

Accordingly, the temporal damping rate for a wave with the wavenumber k can be estimated by the formula

$$\gamma_t \sim \nu_t k^2 \sim \langle u^2 \rangle \frac{k^2}{\omega}. \tag{57}$$

Note that for the case of wave damping by turbulence produced by the wave itself, a different expression for turbulent viscosity is given in [52] , that is

$$\nu_t \sim l^2 \left| \frac{\partial U}{\partial z} \right|, \tag{58}$$

where l is the turbulent scale assumed to be of the order of $a + z$ (a is the wave amplitude; z is the distance to free surface). In this case, the viscosity depends on the wave amplitude; thus, damping is nonexponential.

Laboratory experiments on surface wave damping by turbulence known to us from literature are very scarce. A brief review and criticism is given in [54]. If we restrict ourselves by the experiments on wave damping by external independently excited turbulence, data of three experiments are available. In experiments [53], turbulence was excited by a submerged oscillatory grid with cells of approximately 1 cm. The oscillating frequency was about 1 Hz; the amplitude was 1 cm. The frequencies of investigated waves lay in the range 1 - 10 Hz. The wave energy was comparable or less than the turbulence energy in the corresponding spectral frequency band.

Two treatments of the obtained results are suggested in [53]. According to the first one, wave damping by turbulence was approximated by the exponent; i.e., the damping coefficient was assumed to be independent of the wave amplitude. Here, the frequency dependence of the damping coefficient in space was approximated as ω^2. In the other treatment, the damping coefficient was assumed to be dependent on the wave amplitude; in this case, the "best fit" dependence was ω^5. According to [53], the spread in experimental points with respect to the last approximating curve was much smaller than in the first case, which permitted the authors [53] to make a statement on nonlinear character of wave damping by turbulence.

A more recent experiment [54] dealt with the damping of cylindrical waves at frequencies from 4 Hz to 5.27 Hz (wavelengths between 6 and 10 cm) which propagated through the region of turbulence excited by a vertically oscillating grid located under a wavemaker. The experiments were carried out at various grid oscillation amplitudes (from 1.3 cm to 5 cm) and oscillation frequencies 0.62 Hz and 0.9 Hz. Detailed measurements of turbulence spectra $\sqrt{(u'^2)}$ have been performed, and using them and the turbulence scale L, the following empirical formula has been suggested for the spatial damping coefficient:

$$\beta_t = 0.103 \frac{\sqrt{u'^2}}{L^{1/3}\lambda^{2/3}} \tag{59}$$

(λ is the surface wavelength). Besides, Skoda's experiments were analyzed in [54], where the authors of [54] declared their good agreement with the suggested dependence (59). It should be noted, however, that the spread in obtained values of the damping coefficient is rather large, which casts doubt on universality of dependence (59).

It can generally be stated that the experiments performed by now are insufficient for drawing any definite conclusions on mechanisms of surface wave damping by turbulence, which requires further investigations.

3.3.2 Method of the experiment

Gravity surface wave damping by small-scale turbulence was investigated in a resonator with a width of 2 cm, depth 40 cm, and length L equal to 29 cm and 15.5 cm (see Fig. 31). A similar resonator was used previously for studying the amplitude dispersion of standing waves. Let us remember that oscillations in the resonator were excited by an electromechanic wavemaker [49] weakly coupled with the resonator through a face wall partially submerged in water; the frequency and amplitude of wavemaker piston oscillations were assigned by the generator of electromagnetic oscillations GZ-103. The surface oscillation parameters were measured by a wire wave gauge, the wires being arranged along the face wall of the resonator (in the oscillation crest).

Turbulent fluid motions were generated by vertical oscillations of the grid; this method is often used for investigation of turbulent processes. Grid 4, a perforated aluminium plate with a thickness of 1 mm, having holes of diameter *d* and spacing *D*, was placed, as a rule, at a depth of 12 cm and oscillated with the frequency f_g= 3 - 5 Hz and swing 12-16 mm. The parameters of turbulent fluid motions were controlled by a thermoanemometric velocity meter DISA with sensor (5) of the type 55R36. The device measurements were calibrated by submerging the sensor (5) in the crest and node of a standing wave. Here, the fluid velocity was calculated by employing the wave frequency and amplitude measured by a string wave recorder with an accuracy not less than 3%. Note that when treating the measurement results of the fluid velocity pulsation paramaters, one should bear in mind that the thermoanemometric sensor measures the fluid velocity modulus; thus, the frequency of sign-alternating pulsations is doubled.

The method of measuring the damping rate (decrement) for surface waves is as follows. Oscillations of the II mode frequency were excited in the resonator, and after the wavemaker was switched off, their time damping was recorded. A Brüel & Kjær analyzer measured the sweep of the oscillations B from the wave trough to the wave crest at each decreasing wave period, assigned by the number n. Then, dependence $B(n)$ was fitted by the exponent function

$$B(n) = B(0)e^{-\gamma n}.$$

Here, the dimensionless decrement γ characterizes the oscillation damping during the time t equal to one wave period $T = f^{-1}$; i.e., $n = \frac{t}{T}$. Wave damping caused by turbulence was found as a difference of the effects in two experiments

$$\gamma = \gamma_\Sigma - \gamma_0,$$

where γ_Σ is the damping decrement of free oscillations in the presence of turbulence and γ_0 in its absence. Natural damping of surface oscillation in the resonator is characterized by the decrement γ_0 determined by energy loss as a result of fluid friction on walls, radiation at the boundary through a partially submerged wall (2), and the presence of a surface active substance. Surface oscillation damping in a resonator of length L =29 cm is shown in Fig. 32 as an illustration. Note that the decrement values $\gamma_0 = 0.039$ and $\gamma = 0.011$ are small enough to consider their contribution to γ_Σ additive.

3.3.3 Experimental results

The aim of the experiments was to study mechanisms of surface wave damping at small-scale turbulence. The turbulence was generated by a grid with holes with a diameter of 2.9 cm and a distance between centers D=3.6 cm; that is approximately eight times less than the resonator length (L=29 cm).

As mentioned above, wave damping at small-scale turbulence is accompanied by transformation of the latter's spectrum. This effect is explicitly demonstrated in Fig. 33, exhibiting the power frequency of fluid velocity pulsations:

$$P(\omega) = (u')^2 \Delta f^{-1},$$

where u' is the pulsation velocity, and Δf is the frequency bandwidth of a single spectral component window. The spectrum was measured in the central part of the resonator at a depth of 1.2 cm. In this case, the grid oscillates at a depth of 12 cm with frequency f_g=5 Hz and amplitude l_g =0.7 cm. In the absence of a surface wave (Fig. 33a), the turbulence spectrum has a maximum at a frequency $F \simeq 0.4$ Hz and decreases as f^{-2} in the frequency range from approximately 0.4 Hz to 3.5 Hz. Note that pulsations at frequency f_g are spread up to the surface. This is indicated by the corresponding spectral component in Fig. 33a. The above-mentioned qualitative peculiarities of the turbulence spectrum were observed for the entire range of values of the amplitude l_p and the frequency f_g of the grid oscillations. A rather high frequency of f_g=5Hz was chosen to reduce the effect of undesirable surface oscillations caused by the above-mentioned grid influence. In particular, at f_g=3 Hz, such oscillations were recorded by a string wave recorder and impeded measurement of wave damping rate. The characteristic spatial scale of turbulence is determined by the grid perforation spacing D. Besides, the grid generated a mean flow in the whole space of the resonator. In the resonator center, right over the grid, the fluid ascended vertically with a velocity of the order of 12 cm/s (for the case of l_g=0.7 cm, f_g=5Hz); in the subsurface layer, this fluid spread to the resonator boundaries with a horizontal velocity of 7-4 cm/s and returned with a velocity of about 3 cm/s to the grid area along the walls. This flow transported small-scale turbulence from the grid to the surface.

Excitation of a standing wave with the frequency f=2.33 Hz by a wavemaker was accompanied by an essential transformation of the frequency spectrum of turbulence, as can be readily seen in Fig. 33b, c: the spectrum becomes localized in the vicinity of the wave frequency f and its harmonics, while the low-frequency components of the turbulence spectrum, at $f_i \ll f$, decrease practically to zero at sufficiently large wave amplitudes A. The corresponding values of the amplitudes are given in Fig. 33.

The turbulence spectrum transformation in the vicinity of the frequency f occurs due to interactions between turbulent and wave fluid motions, resulting in the generation of oscillations with the sum frequency, $f + f_i$, and the difference frequency, $f - f_i$. This is evident, in particular, for a "marked" component with the frequency f_g. In the presence of the wave, oscillations with the frequencies $f^+ = f_g + f$ and $f^- = f_g - f$ are seen.

The interaction of the wave with turbulence takes place, primarily, in a relatively thin fluid layer adjacent to the surface. Fig. 34 shows the measured dependence of the relative change of the pulsation power due to a surface wave on depth z in the frequency range from f to $2f$ for a fixed wave amplitude A=0.4 cm. This value is defined as

$$m(z) = \frac{\sum_f^{2f} P(z) - \sum_f^{2f} P_0(z)}{\sum_f^{2f} P_0(z)},$$

where $P(z)$ and $P_0(z)$ are the pulsation power densities in the absence and presence of a standing wave, respectively. As seen from Fig 34, the experimental data are satisfactorily described by the exponential function (dashed line)

$$m(z) \simeq e^{2k(z-z_0)},$$

where k =21,8 m^{-1} is the wavenumber, and $z_0 = 1.2$ cm. This result suggests that below $z = z_0$, the rate of the turbulence spectrum transformation is proportional to the squared amplitude, $(A\omega e^{kz})^2$, of the fluid velocity in the wave.

The process of turbulence transformation analogous to that considered above was also observed in a traveling wave. Fig. 35(a) shows the spectrum of turbulence generated in a channel with a length of $L \approx 300$ cm by the same grid which was used in the resonator; the result of the action of a traveling wave with amplitude $a \simeq 0.25$ cm and frequency f=2.3 Hz on turbulence can be seen in Fig. 35b.

The turbulence spectrum transformation is accompanied by wave damping. We shall characterize it by a local decrement γ. The wave damping was accompanied by a small amplitude modulation due to the grid action on the surface and, probably, to slight random variations of the damping rate. To suppress the influence of random factors (such as the surface fluctuations due to the direct action of turbulence), the decrement γ was measured in the time intervals of $5f^{-1}$ and larger, and the data averaged over several experiments were used. In particular, the oscillation envelope shown in Fig. 32 is obtained as a result of averaging over six realizations.

To be able to judge about the mechanism of wave damping by the turbulence, we analyzed the dependence of γ on the wave amplitude A. The corresponding experimental data are presented in Fig. 36. Two qualitatively different attenuation regimes were proved to be possible depending on the wave amplitude, with a conventional boundary between them at some amplitude A^*. At small amplitudes, $A < A^*$, the turbulent pulsation power decreases with A (see Fig. 33b), and the decrement γ is constant (to an accuracy of measurement errors). On the other hand, as is seen in Fig. 33c, for $A > A^*$, the total turbulence energy is changed. Here, the decrement reduces rapidly with the increase of A; these data can be approximated by the function

$$\gamma = \gamma_0 \left(\frac{A_0}{A}\right)^2,$$

which is shown by a dashed line in Fig. 36; here, γ_0 is the wave decrement for the fixed amplitude $A_0 \geq A^*$.

In conclusion, let us briefly discuss a possible mechanism of wave damping by turbulence in our case, in which the frequency F of maximal (large-scale) turbulent velocity pulsations is much less than the wave frequency f. In this case, the wave-turbulence interaction leads to the appearance in the turbulence spectrum of combinational components with higher frequencies, such as $f \pm F$. The wave attenuates due to its energy consumption for this process. If the wave amplitude is small, a part of the turbulence energy transformed in such a way is proportional to the wave power (provided these two processes are statistically independent); hence $\gamma = const$. For higher amplitudes, however, the transformed part of the turbulence is saturated. As a result, with further increase of the initial amplitude for a fixed f, the amount of the wave energy spent on turbulence transformation remains constant, and its ratio to the wave energy decreases as A^{-2}, hence, $\gamma \sim A^{-2}$. Note also that the situation when F is comparable with f is of interest. In this case, the wave amplification by turbulence is possible in principle.

4 Conclusion

There were two overal goals of this work. The first was the development of theoretical models that will increase our understanding of interactions between the main types of motions in the upper ocean layer: surface and internal waves, currents, and turbulence. The second goal was to check some of these models in laboratory tanks of the IAP.

In the course of these investigations, the following THEORETICAL MODELS were developed.

Modulation of the growth rate of short capillary-gravity surface waves by long waves in the presence of turbulent wind was studied. This mechanism enables us to explain intense interaction between short and long surface waves even in the case of small slopes of long waves, and a strong difference in scale between long and short waves.

Transformation of surface waves on 2-D inhomogeneous flows on the ocean surface were studied. Such flows can be created, for example, in the case of streamlining of different submarine obstacles. Resonance effects caused by scattering of a surface gravity wave on such moving obstacles and internal wave generation by stratified shear flows with critical layers around such obstacles were studied.

The ideas that have been developed before in the soliton theory were applied for construction of models of different geophysical flows. Perturbation theory was developed for the motion of small vortices interacting with each other and in a stratified fluid. Stationary nonlinear waves in the frames of the modified nonlinear Schrödinger equation were found.

EXPERIMENTAL STUDIES were carried out in the large thermostratified tank and other laboratory facilities of IAP. The experimental data were compared with the results of the theoretical calculations.

Investigation of the transformation of surface waves on the underwater currents in the large thermostratified tank comprises an important part of the experimental section of this memorandum. In the framework of this program, particular attention was given to two problems. The propagation of short trains of intense surface waves in deep water was studied experimentally in the large thermostratified tank. The evolution of abrupt changes of the surface-wave intensity for various wave amplitudes was analyzed. Investigation of surface wave transformation on a non-uniform current was carried out in the large thermostratified tank. The spatial variability of the surface wave amplitude above a moving sphere was recorded. The dependence of the parameters of surface anomalies on the surface wave frequency was analyzed. At the later stage of these experiments use of remote devices (camera connected with IBM PC) was started. In future experiments, optical spectrum analyzers and microwave scatterometers will also be used.

Finite-amplitude gravity-capillary wave curvature was measured in the wind-wave oval tank. The distribution functions of crest and trough curvatures of short small-amplitude gravity waves were obtained, the wave profile asymmetry growth with its amplitude increase was analyzed, and the transformation of the curvature distribution functions on the profile of steep gravity waves was studied.

Gravity surface wave interactions were studied. The values of nonlinear additions to the wave phase velocity occurring due to the self-action and interaction of wave pairs propagating in opposite direction were measured. The experimental data were compared to the calculation results.

Surface wave damping due to turbulence was investigated. The wave amplitude decreases when passing through the turbulent region, and the related changes in the turbulence spectrum were measured.

In future studies, it is planned to widely use the remote sensing methods of measurements in tanks, along with the contact methods. The long-term planning of environmental studies may include field experiments. IAP has an automated complex of remote-sensing devices for shipboard use which includes optical spectrum analyzers, radar, and Doppler sonar. In the past few years, a bulk of data was collected and processed that has permitted us to evaluate a number of details of interaction between internal and surface waves and confirm some of the theoretical predictions.

5 Acknowledgments

The cooperation with NOAA Environmental Technolology Laboratory and the support from the joint NOAA/DOD Advanced Sensor Application Program are greatly appreciated.

References

[1] Laboratory modeling and theoretical studies of wave interactions in the upper ocean. Part 1: Experimental Design and Program (L. A. Ostrovsky, Editor). *NOAA Technical Memorandum, ERL ETL-278*, Environmental Technology Laboratory, Boulder, Colorado, 1997.

[2] Laboratory modeling and theoretical studies of wave interactions in the upper ocean. Part 2: First Stage Results. (L. A. Ostrovsky, Editor). *NOAA Technical Memorandum, ERL ETL*, Environmental Technology Laboratory, Boulder, Colorado,1997.

[3] Smith, J. A., 1990. Modulation of short wind waves by long waves. In: *Surface Waves and Fluxes*, v. 1, Kluwer Academic Publishers. Netherlands, 247-284.

[4] Valenzuela, G. R. and Wright, J. W., 1979. Modulation of short gravity-capillary waves by longer-scale periodic flows. A higher order theory. *Radio Sci.*, v. 14, 1099-1110.

[5] Landahl, M. T., Widnall, S. E., and Hultgen, L., 1981. An interactional mechanism between large and small scales for wind-generation water waves. *Proc. 12th Symp. on Naval Hydrodynamics*, National Academy of Sciences, p. 541.

[6] Miles J. W., 1962. On the generation of surface waves by shear flows. Part 4. *J. Fluid Mech.*, v. 13, 433-448.

[7] Troitskaya Yu. I., 1994. Modulation of the growth rate of short surface capillary-gravity wind waves by a long wave. *J. Fluid Mech.*, v. 273, 169-187.

[8] Troitskaya, Yu. I., 1997. Modulation mechanism of the growth rate of short surface turbulent wind waves by swell waves. *Izvestija RAN, Fizika Atmosfery i Okeana* (in press).

[9] Monin, A. S., and Yaglom, A. M., 1971. *Statistical Fluid Mechanics: Mechanics of Turbulence*, Cambridge, MA, MIT Press.

[10] Reutov, V. P. and Troitskaya; Yu. I., 1995. On nonlinear effects at interaction between water waves and turbulent wind. *Izvestiya RAN, Fiz. Atm. Okeana*, v. 31, 825-834.

[11] Smolyakov, A. V., 1973. Spectrum of quadrupole radiation of a plane turbulent boundary layer. *Akust. Zh.*, v.19, no. 3, 420-425.

[12] Davis, R. L., 1972. On prediction of the turbulent flow over a wavy boundary. *J. Fluid Mech.*, v. 52 (pt. 2), 287-306.

[13] Plant, W. J., Keller, W. C., and Cross, A., 1083. Parametric dependence of ocean wave-radar modulation transfer functions. *J. Geophys. Res.*, v. 88 (C14), 9747-9756.

[14] Ostrovsky, L.A. Electromagnetic waves in nonlinear media with dispersion. Zh. Techn. Fiz., v. 33, no. 8, 905-908, 1963 (English version: Sov. Phys-Techn. Phys., v. 8, no. 8, 679-681, 1964).

[15] Ostrovsky, L. A., 1966. Propagation of wave packets and space-time self-focusing in a nonlinear medium. *J. Exptl. Theor. Phys.*, v. 51, 1189-1194. (In English: *Sov. Phys. JETP*, v. 24, no. 4, 797-800, 1966).

[16] Akhmanov, S. A., Visloukh, V. A., and Chirkin, A. S., 1986. Wave packets self-action in a nonlinear medium and the femtosecond laser pulses generation. *Soviet Phys. Advances*, v. 149, 350-383.

[17] Dysthe, K. B., 1979. Note on a modification to the nonlinear Schrödinger equation for application to deep water waves. *Proc. R. Soc. Lond.*, A369, 105-114.

[18] Benjamin, T. B. and Feir, J. E., 1967. The disintegration of wave trains on deep water. Part 1., Theory. *J. Fluid Mech.*, v. 27, 417-430.

[19] Yuen, H. C. and Lake, B. M., 1982. Nonlinear dynamics of deep-water gravity waves. *Advances in Appl. Mech.*, v. 22, 67-229.

[20] Su, M. Y., 1982. Evolution of group of gravity waves with moderate to high steepness. *Phys. Fluids*, v. 25, 2167-2174.

[21] Lo, E. and Mei, C. C., 1985. A numerical study of water-wave molation based on a higher-order nonlinear Schrödinger equation. *J. Fluid Mech.*, v. 150, 395-416.

[22] Zakharov, V. E. and Shabat, A. V., 1971. Exact theory of two-dimensional self-focusing and one-dimensional self-modulation of waves in nonlinear media. *ZhETF*, v. 61(1), 26-35.

[23] Hirota, R., 1972. Exact solution of the modified Korteveg-deVries equation for multiple collision of solitons. *J. Phys. Soc. Japan*, v. 33, 1456-1458.

[24] Hirota, R., 1965. Exact envelope-soliton solution of a nonlinear wave equation. *J. Math. Phys.*, v. 14, 805-809.

[25] Wadati, M., 1972. The exact solution of the modified Korteveg-de Vries equation. *J. Phys. Soc. Japan*, v. 32, 1681.

[26] Gray, E. P., 1978. Scattering of surface wave by a submerged sphere. *J. Eng. Math.*, v. 12, 15-41.

[27] Grue, J. and Palm, E., 1985. Wave radiation and wave diffraction from a submerged body in a uniform current. *J. Fluid Mech.*, v. 151, 257-278.

[28] Haskind, 1973. M.D. *Hydrodynamic Theory of Ship Motions*. Moscow: Nauka. 328 p.

[29] Newman J., 1985. *Sea Hydrodynamics*. Leningrad: Sudostroenije. 368 p.

[30] Dolina, I. S. and Pelinovsky, E.N., 1987. Surface gravity-wave scattering by small submerged bodies. Doklady AN SSSR, v. 295, no. 5, 1058-1060.

[31] Dolina, I. S. and Pelinovsky, E. N., 1987. Long-wave approximation in problems on sea wave scattering by bodies. In: *Methods of Hydrophysical Research. Waves and Vortices*, Inst. Appl. Phys., USSR Acad. Sci., Gorky, USSR, 184-194.

[32] Cherkesov, L. V., 1973. *Surface and Internal Waves. Kiev, Naukova Dumka*, 248 p.

[33] Lim, C. S., 1981. Water waves generated by an oscillatory surface pressure travelling at critical speed. *Wave Motion*, v. 3, 159-179.

[34] Dagan, G. and Miloh, T., 1982. Free surface flow past oscillating singularities at resonance frequency. *J. Fluid Mech.*, v. 120, 139-154. .

[35] Borovikov, V. A., 1997. Resonance far field excited by a moving oscillating source. *Okeanologiya* (in press).

[36] Gaponov-Grekhov, A. V., Dolina, I. S., and Ostrovsky, L. A., 1983. Anomalous Doppler effect and radiation instability of oscillators in hydrodynamics. *Doklady AN SSSR*, v. 268, no. 4, 827-831.

[37] Badulin, S. I., Pokazeev, K. V., and Rozenberg, A. D. 1983. Laboratory investigation of regular gravity-capillary wave transformation in inhomogeneous flows. Izv. AN SSSR, Fiz. Atmos. Okeana, v. 19, no. 10, 1035-1041.

[38] Schooley, A. H., 1955. Curvature distribution of wind created water waves. *Trans. Amer. Geophys. Union*, v. 36, no. 2, 274-278.

[39] Wu, J., 1971. Slope and curvature distributions of wind-disturbed water surface. J. Opt. Soc. Amer., v. 61, no. 7, 852-858.

[40] Wu, J., 1977. Directional slope and curvature distributions of wind waves. *J. Fluid Mech.*, v. 79, pt. 3, n. 10, 463-480.

[41] Esipov, I. B., Naugol'nykh, K. A., Nosov, V. N., and Pashin, S. Yu., 1986. Measurement of probability distribution of sea surface curvature radii. *Izvestiya AN SSSR, Fiz. Atmos. Okeana*, v. 22. no. 10, 1115-1117.

[42] Nosov, V. N. and Pashin, C. Yu., 1990. Statistical characteristics of wind-crested sea waves in the gravity and capillary range. *Izvestiya, Atmos. Oceanic Physics*, v.26, 851-856.

[43] Burtsev, Yu. G. and Pelevin, V. N., 1972. Curvature distribution of environmental elements of wavy sea surface. Light fields in the ocean. *Preprint*. Moscow, IO AN SSSR, 231-232.

[44] Longuet-Higgins, M. S., 1963. The generation of capillary waves by steep gravity waves. *J. Fluid Mech.*, v. 16, 138-159.

[45] Ermakov, S. A., Ruvinsky, K. D., Salashin, S. G., and Freidman G. I., 1986. Experimental investigation of gravity-capillary ripple generation by strongly nonlinear waves on deep fluid surface. *Izv. AN SSSR, Fiz. Atmos. Okeana*, v. 22, no. 10.

[46] Ermakov, S. A., Ruvinsky, K. D., and Salashin, S. G., 1988. On local relation between characteristics of ripple on gravity-capillary wave crests and their curvature. *Izv. AN SSSR, Fiz. Atmos. Okeana*, v. 24. no. 7, 771-773.

[47] Ruvinsky, K. D., Feldstein, F. I., Freidman, G. I., 1991. Numerical simulations of the quasi-stationary stage of ripple excitation by steep gravity-capillary waves. *J. Fluid Mech.*, v. 230, 339-353.

[48] Longuet-Higgins, M. S., 1992. Capillary rollers and bores. *J. Fluid Mech.*, v. 240, 659-679.

[49] Phillips, O. M. 1958. The scattering of gravity waves by turbulence. *J. Fluid Mech.*, v. 5, 177-192.

[50] Boyev, A. G., 1988. The damping of surface waves by intense turbulence. *Izv. AN SSSR, Fiz. Atmos. Okeana*, v. 7, 31-36.

[51] Kitaigorodsky, S. A. and Lumley, J. L., 1983. Wave-turbulence interactions in the upper ocean. Part 1. The energy balance of interacting fields of surface wind waves and wind-induced three-dimensional turbulence. it J. Phys. Oceanogr., v. 13, 1977-1987.

[52] Levedi, V. G., 1962. *Physicochemical Hydrodynamics.* N.J., Prentice Hall

[53] Green, T., Medwin, H., and Paquin, J. E., 1972. Measurements of surface wave decay due to underwater turbulence. *Nature Phys. Sci.*, v. 237, 115-117.

[54] Olmer, H. and Milgram, J. H. An experimental study of attenuation of short water waves by turbulence. *J. Fluid Mech.*, v. 239, 133-156.

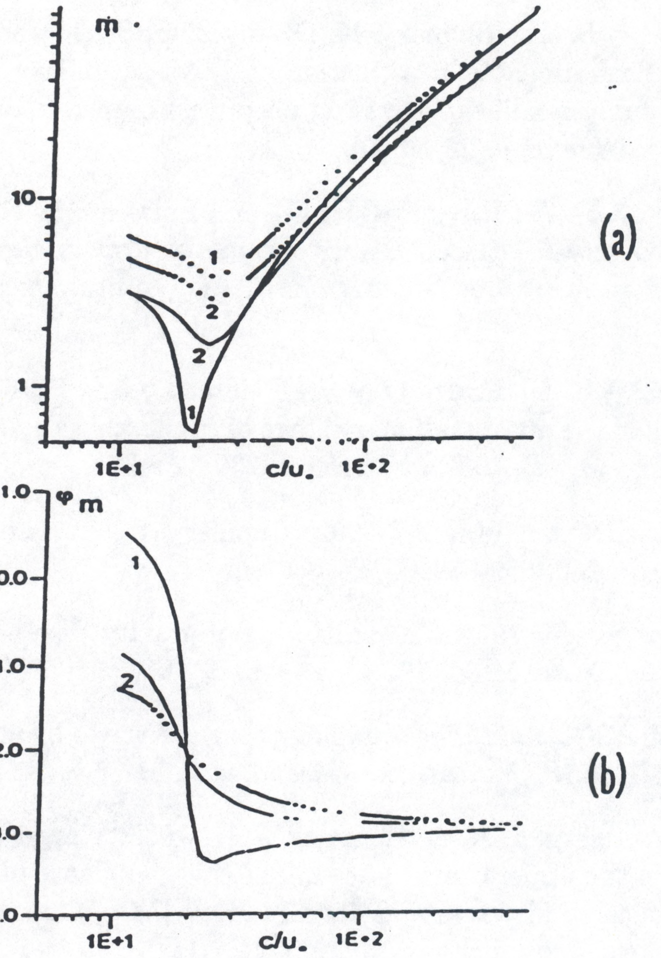

Fig. 1 . Modulus m (a) and phase φ_m (b) of modulation coefficient of short-wave wind increment versus normalized long-wave phase velocity $\frac{c}{u_*}$. Wind friction velocity is $u_*=10$ cm/s. Short-wave wavenumbers are 1 - $K = 0.3cm^{-1}$, 2 - $K = 3cm^{-1}$. Solid lines show data of exact calculation, dashed lines - data by approximate formula (13).

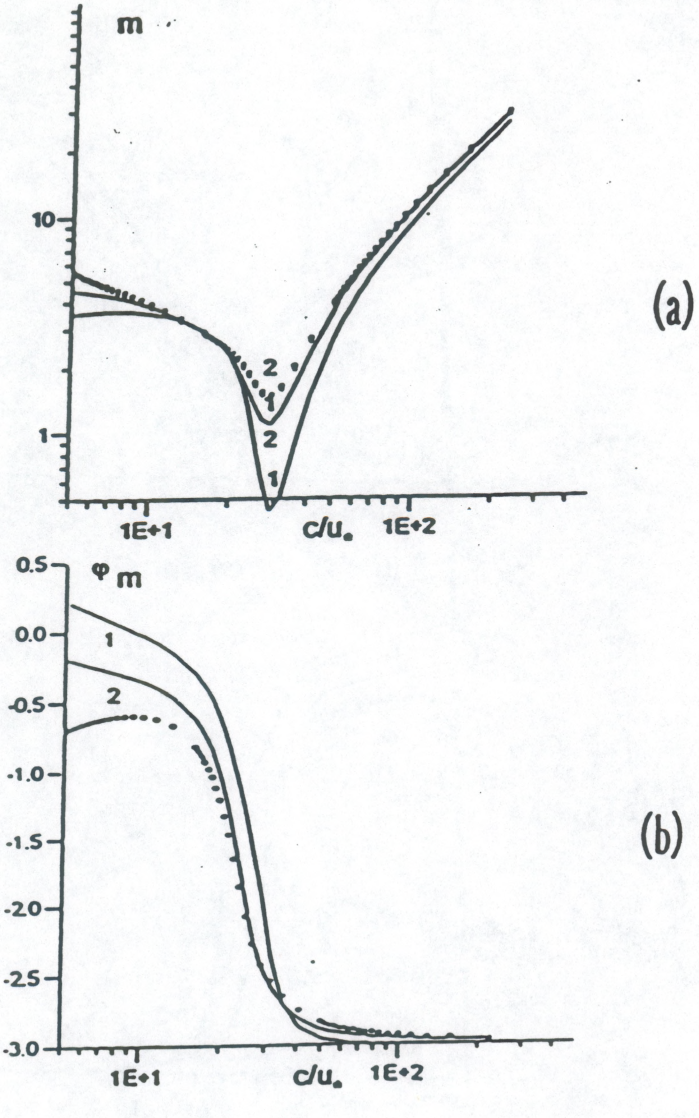

Fig. 2. The same as in Fig. 1, for $u_* = 20$ cm/s.

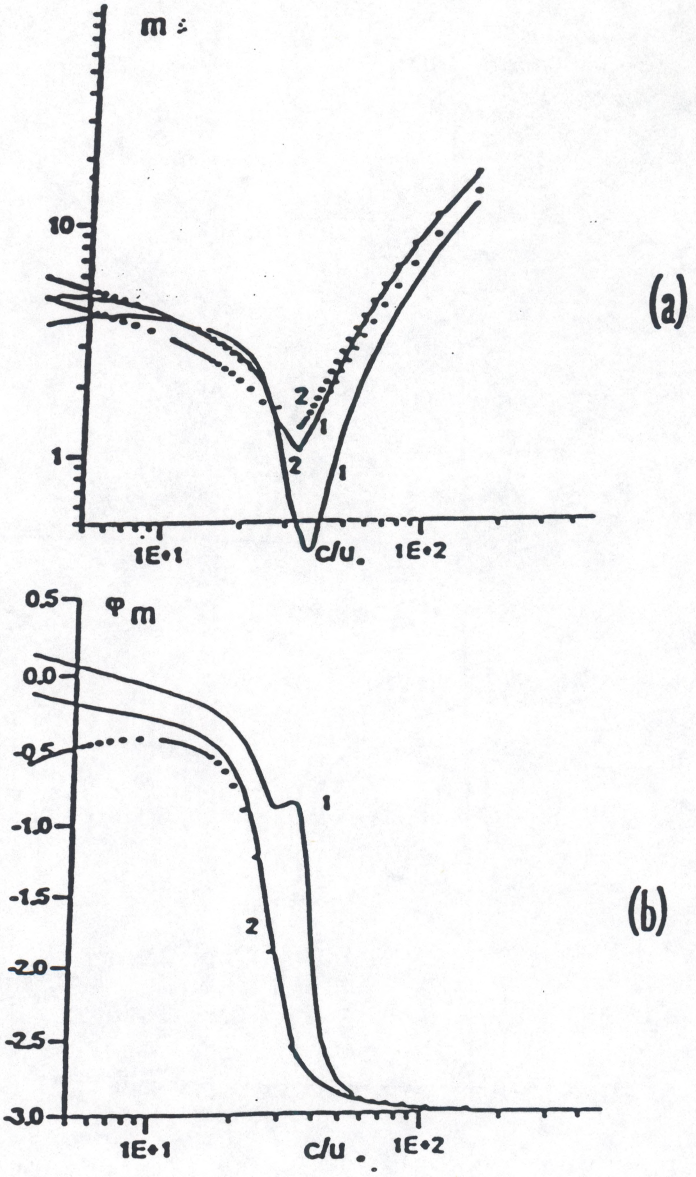

Fig. 3. The same as in Fig. 1, for $u_* = 30$ cm/s.

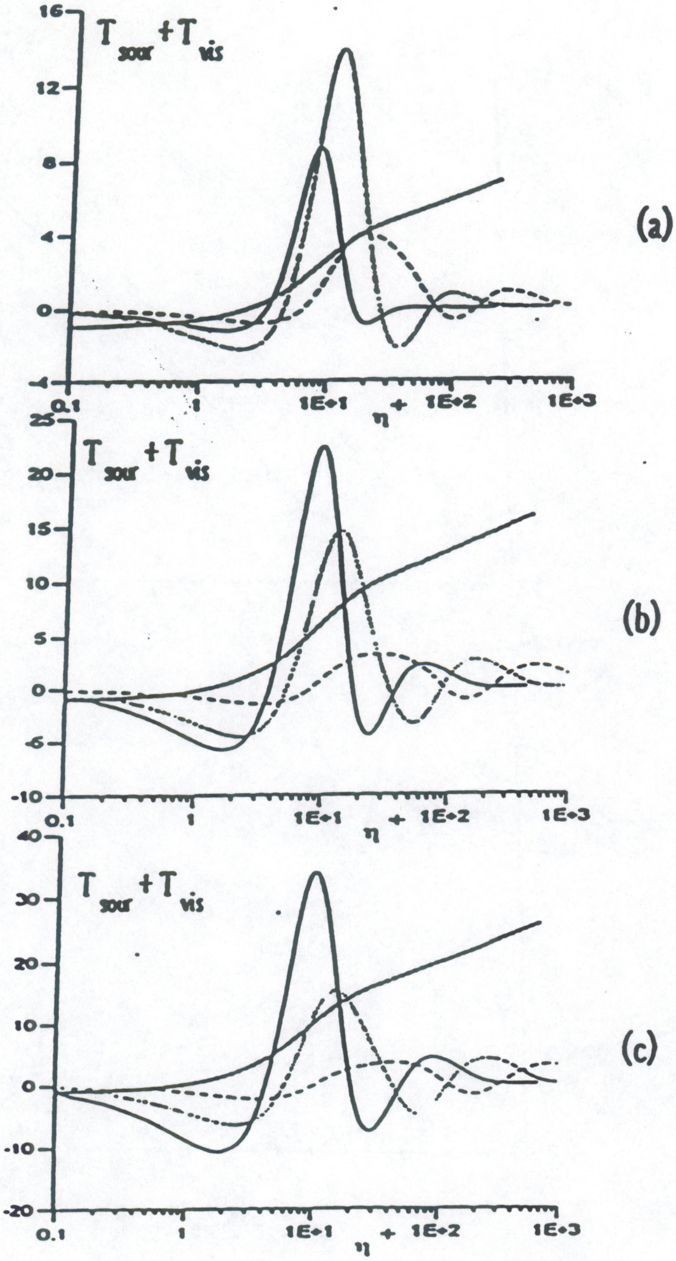

Fig. 4. Energy flux density profiles from wind to waves: a) $u_* = 10$ cm/s, b) $u_* = 20$ cm/s, c) $u_* = 30$ cm/s

______________________ $K=3$ cm^{-1}

.... $K=1$ cm^{-1}

-- - - - - - -- $K=0.3$ cm^{-1}

·+··+··+··+· is wind velocity profile.

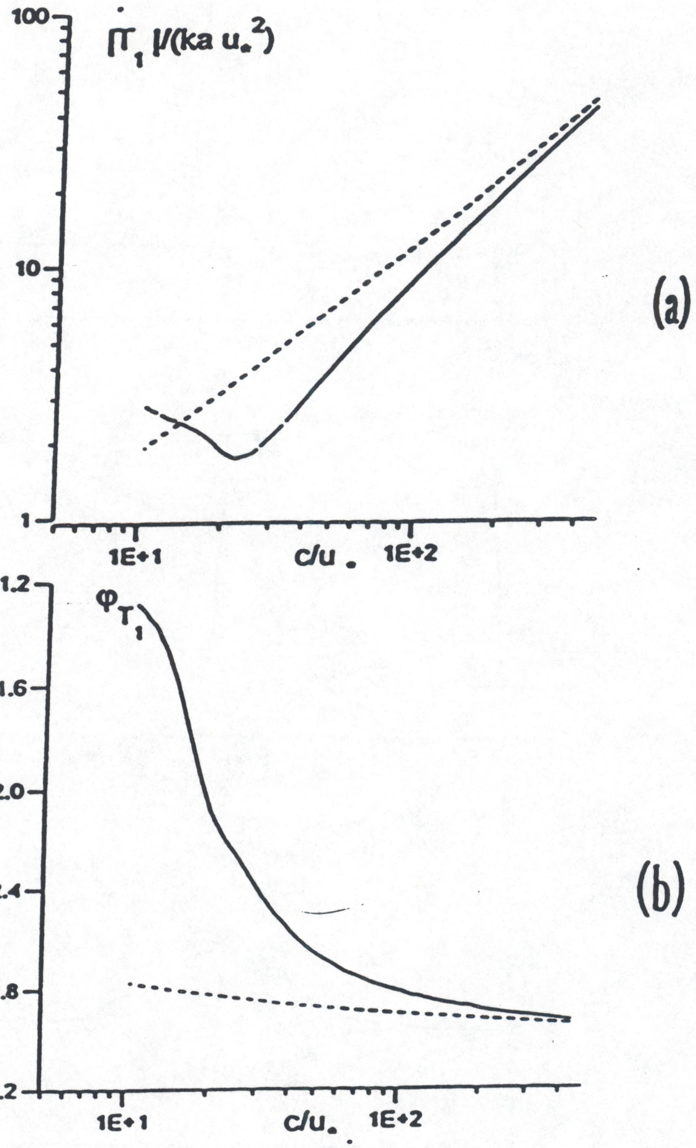

Fig. 5. Modulus (a) and phase (b) of modulation coefficient versus tangential viscous stress on water surface. Solid line shows numerical calculation, dashed line - calculation by formula (14). Wind friction velocity is $u_* = 10$ cm/s.

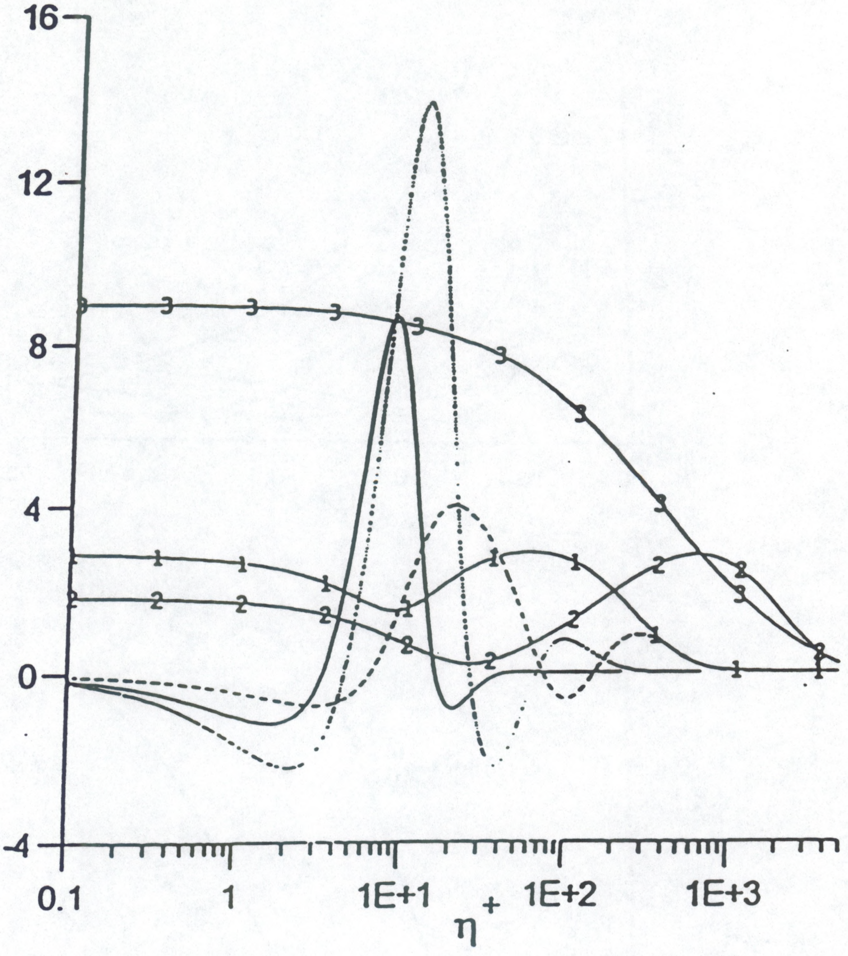

Fig. 6. Profiles of long-wave perturbation of tangential viscous stress $T_1(\eta^+)$ at $u_* = 10$ cm/s. Curves are marked by digits: 1 for $c/u_* = 10$, 2 for $c/u_* = 20$, 3 for $c/u_* = 100$. Profiles of energy flux density from wind to waves ___________________ $K = 3$ cm^{-1} .... $K = 1$ cm^{-1} - - - - - - - - $K = 0.3$ cm^{-1}.

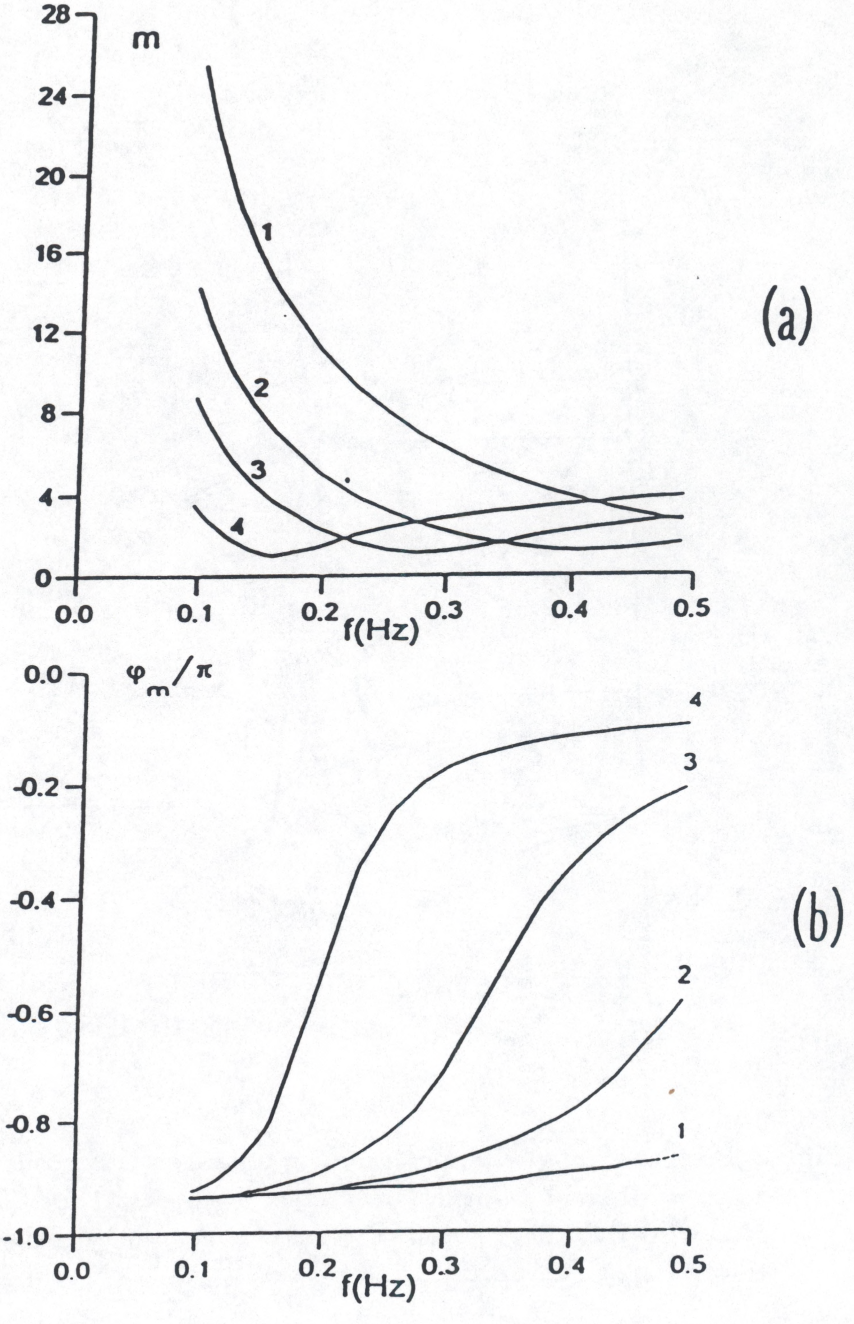

Fig. 7. Modulus m (a) and phase φ_m (b) of modulation coefficient of wind increment of $\lambda = 2.1$ cm wave on long-wave frequency for various wind velocities: 1 - $u_* = 10$ cm/s, 2 - $u_* = 15$ cm/s, 3 - $u_* = 20$ cm/s, 4 - $u_* = 30$ cm/s.

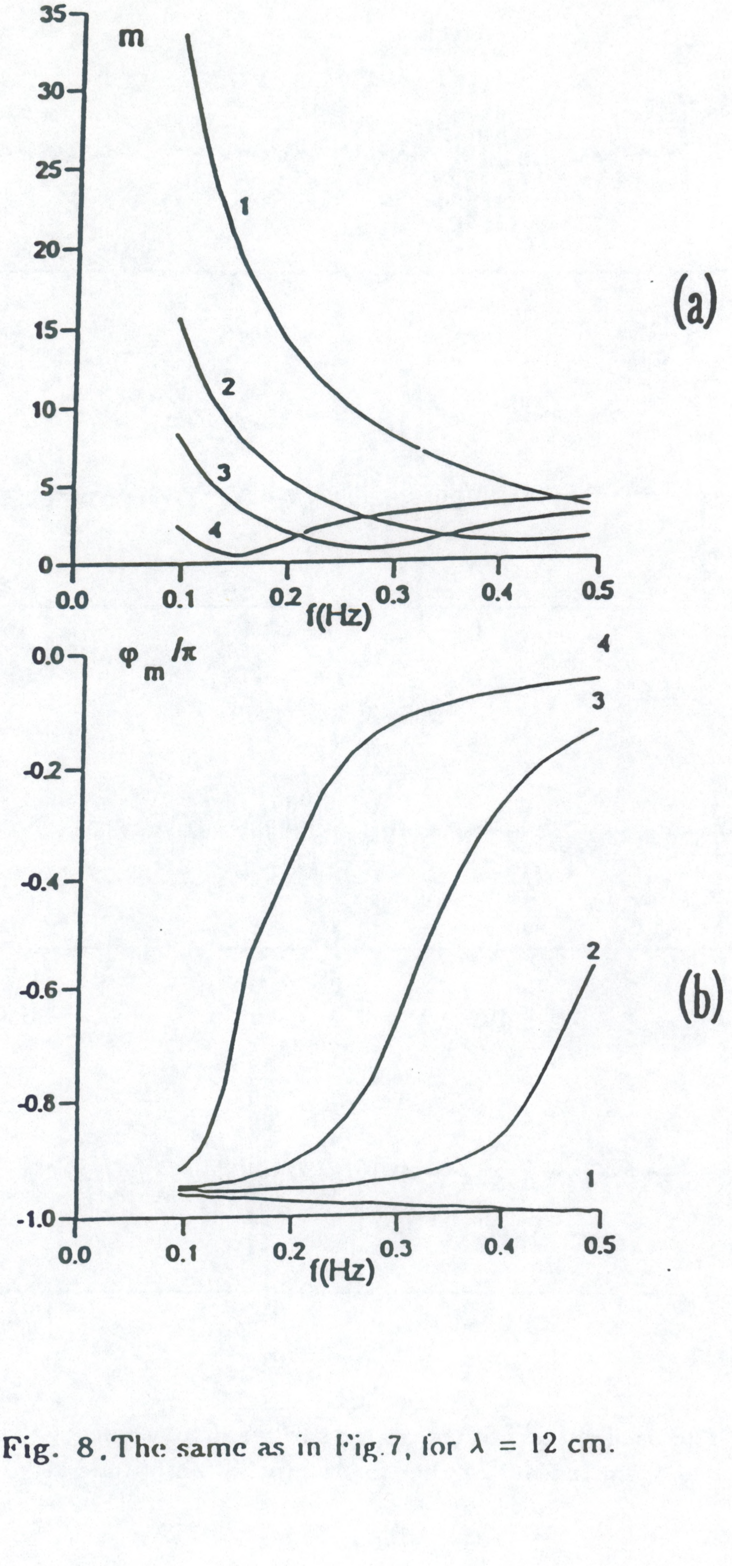

Fig. 8. The same as in Fig.7, for λ = 12 cm.

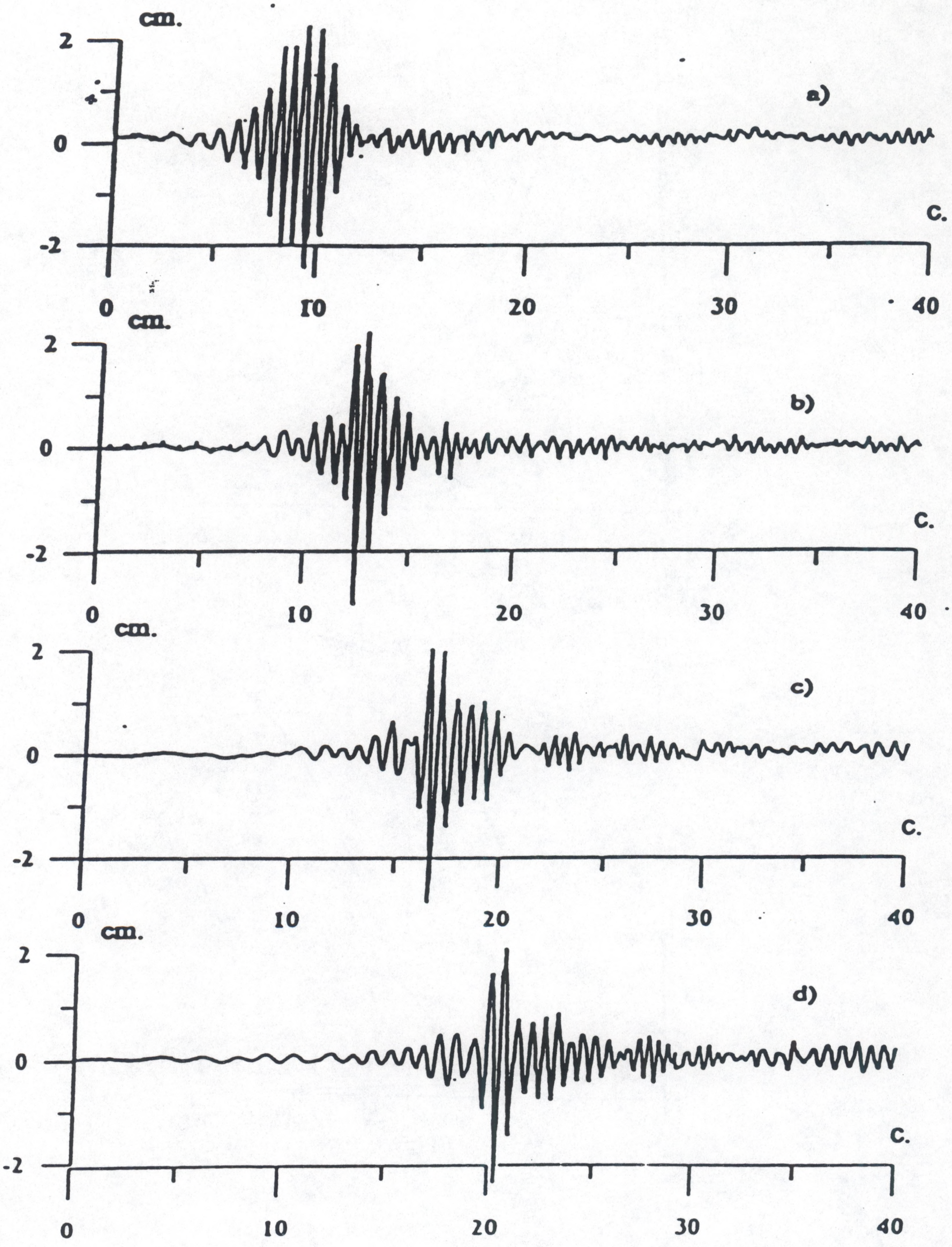

Fig. 9. The oscillograms of the water-surface displacements at different distances from the wavemaker for the initial amplitude $a = 3\text{cm}$.

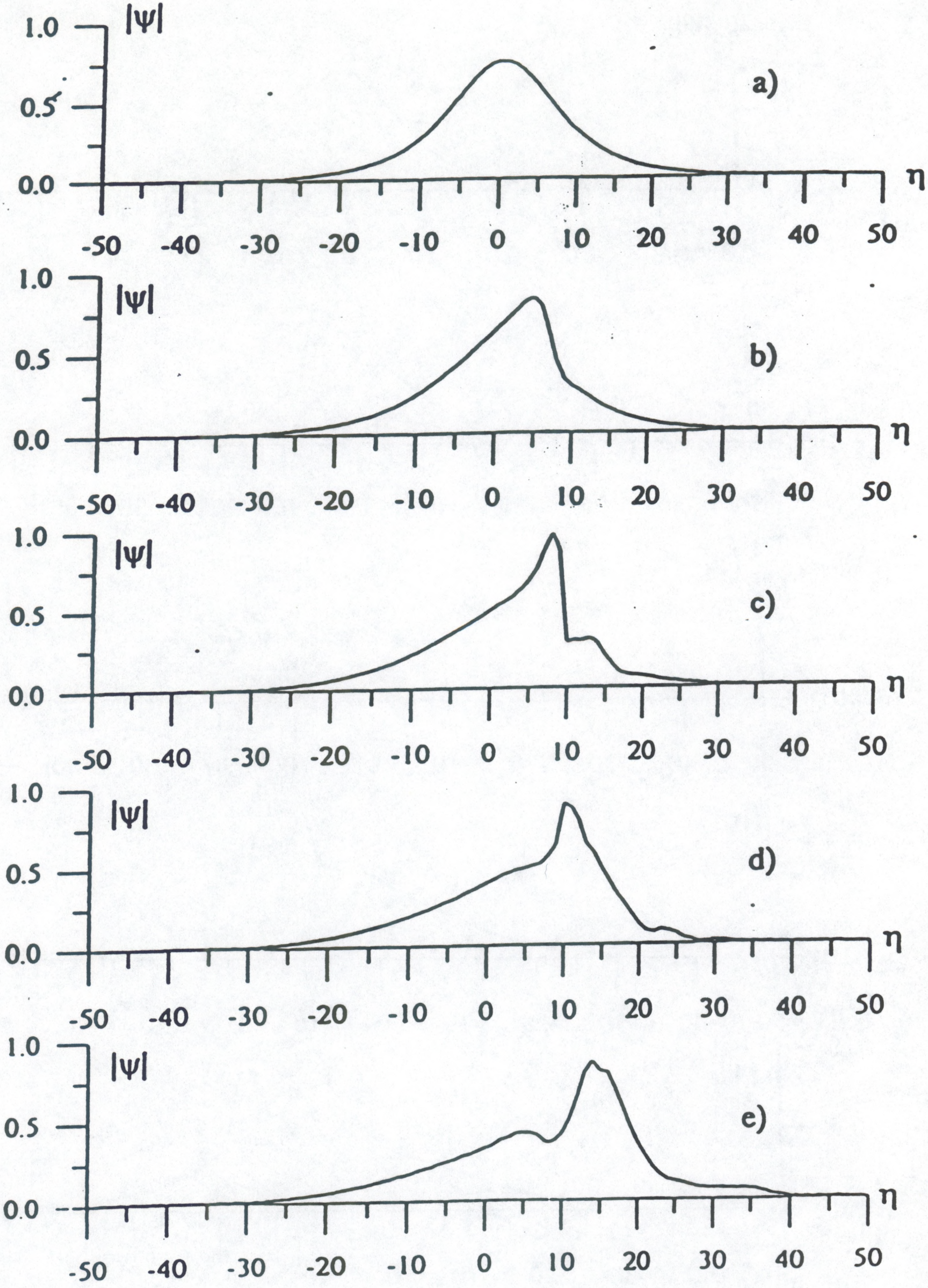

Fig. 10. The result of simulation of Eq. (23) under the initial conditions (24) for the dependence of the wave train envelope modulus $|\psi|$ on coordinate η at different time moments τ.

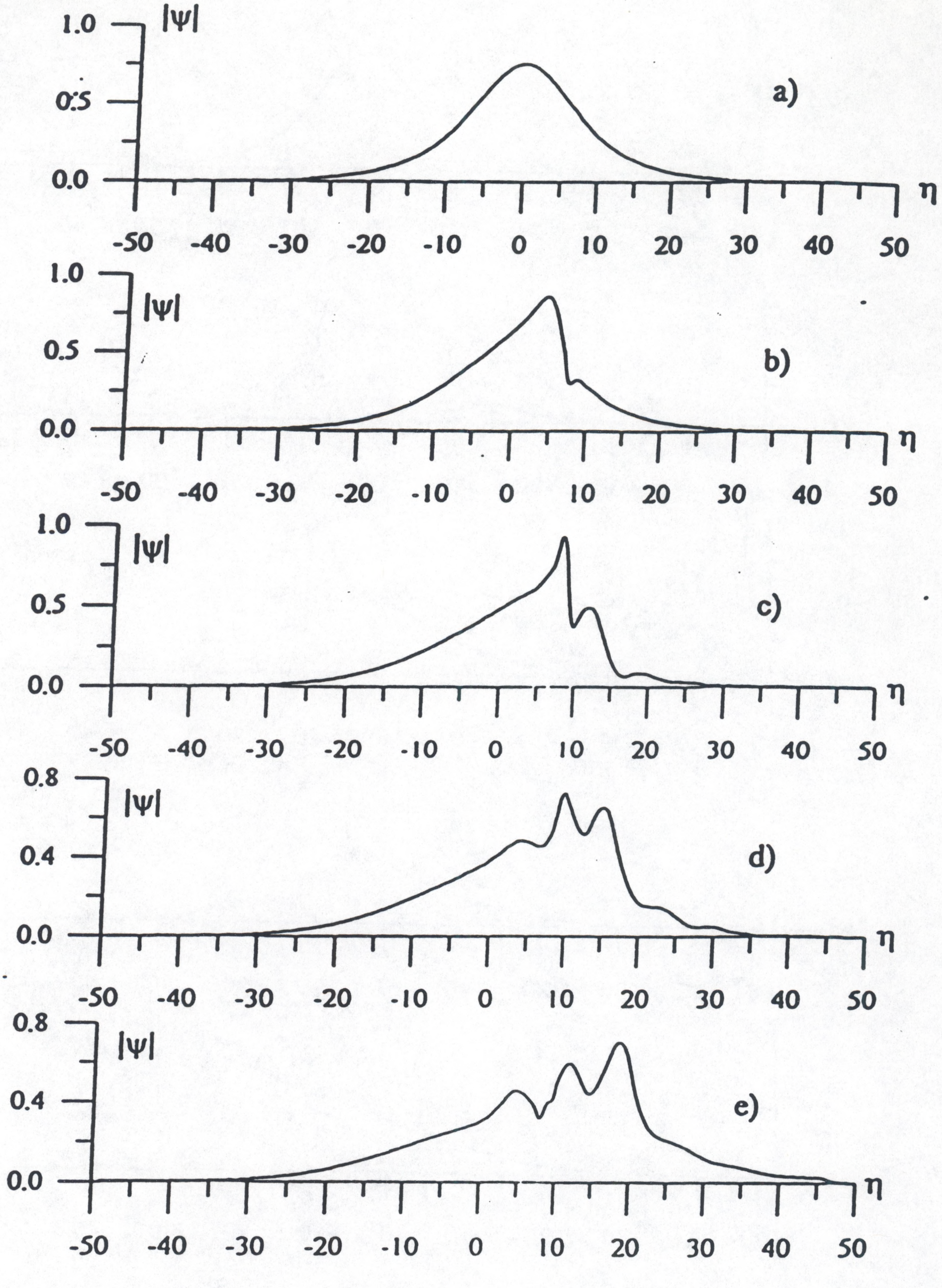

Fig. 11. The result of simulation of Eq. (23) without an integral term under the same initial condition (24) at the same time moments as those in Fig. 10.

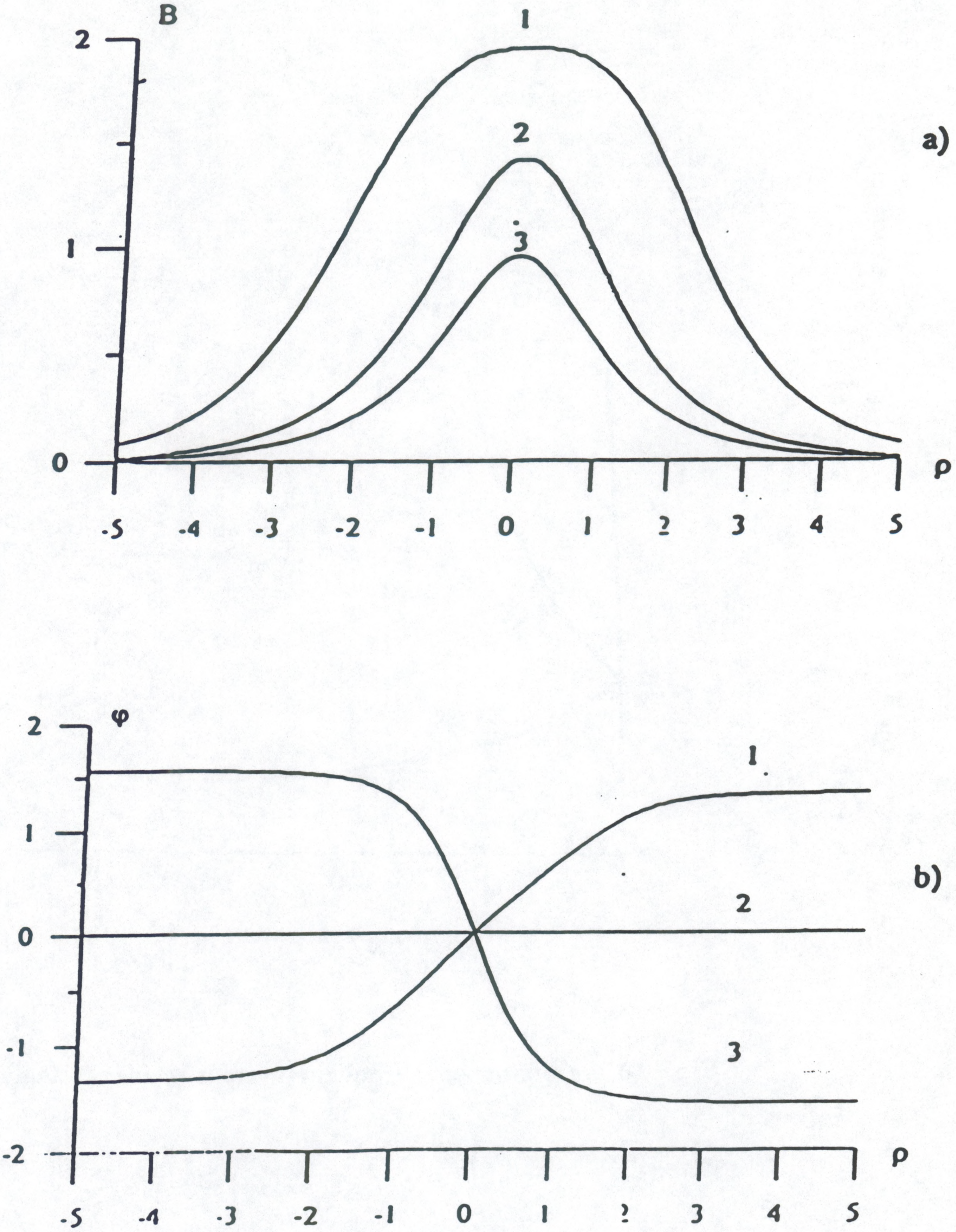

Fig. 12. The dependence of the packet envelope B and phase φ on coordinate ρ for different values r a)- envelope B; b) - phase φ for $q = r$. Curves 1 correspond to the value $r = -2990/16000$, $2 - r = 0$, $3 - r = 2$.

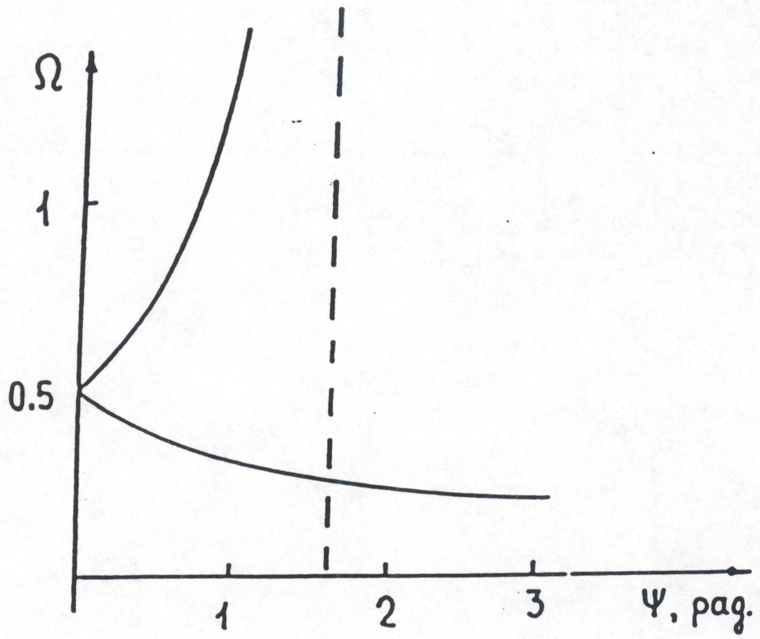

Fig. 13. Resonant wave frequency versus incidence angle Ψ.

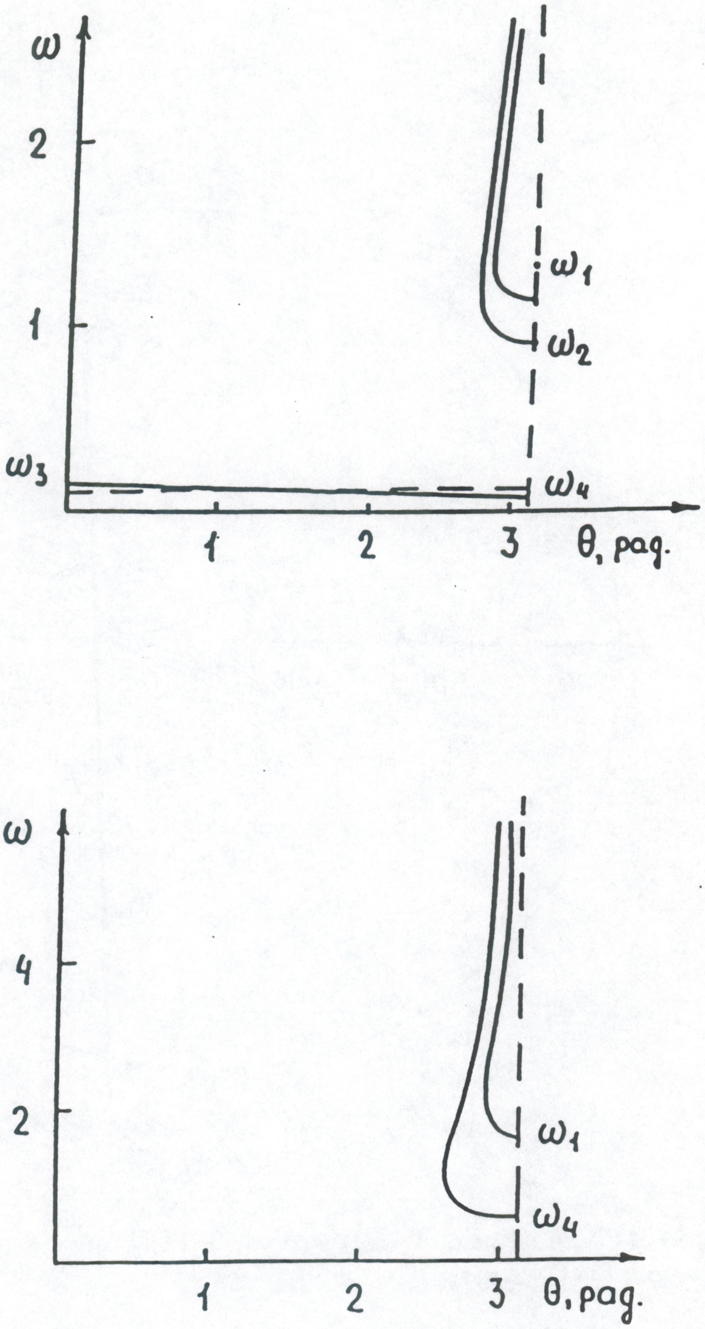

Fig. 14. Scattered wave frequency versus angle θ: a) $\Omega_1 = 0.1$; b) $\Omega_1 = 1$.

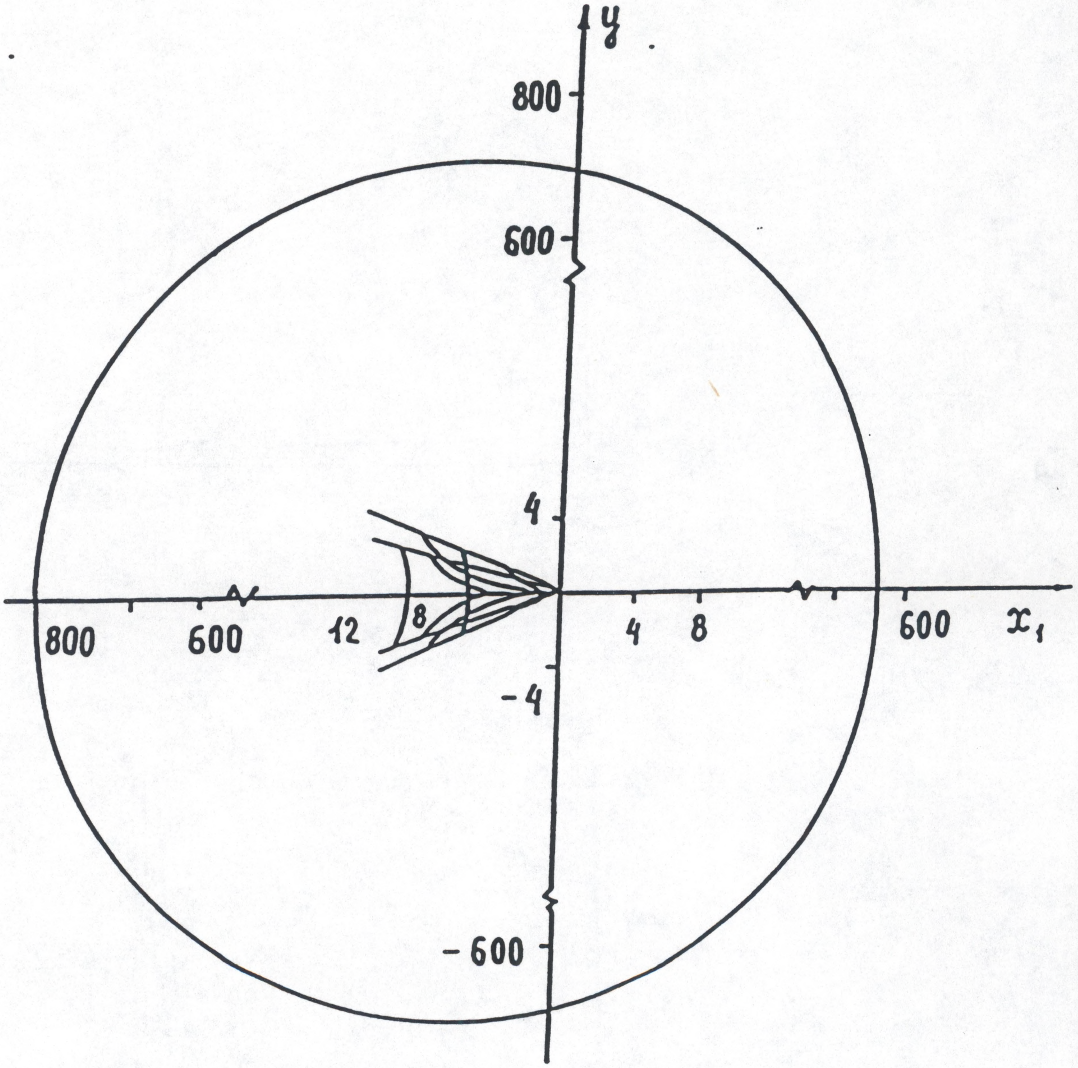

Fig. 15. Phase picture of scattered waves in accompanying coordinate system for $\Omega_1 = 0.1$.

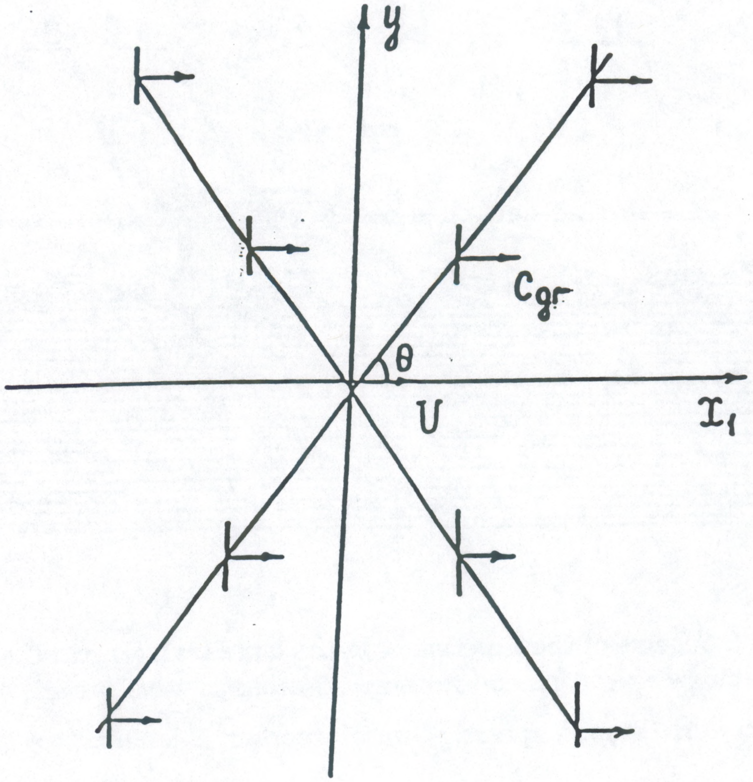

Fig. 16. Schematic form of phase picture of scattered waves in resonance.

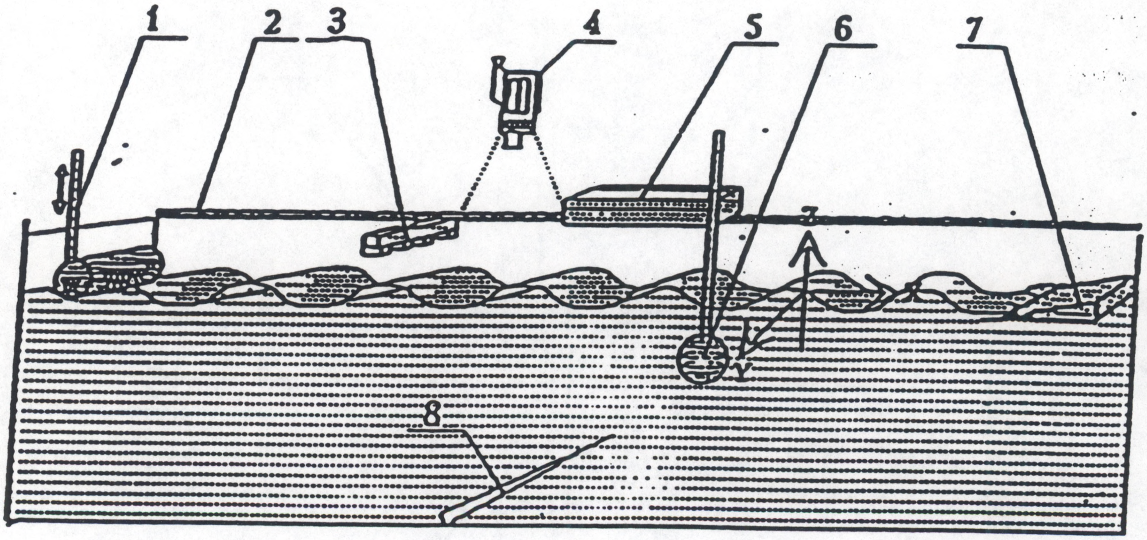

Fig. 17. Scheme of the experiment in the large tank (longitudinal section): 1-surface wave generator; 2-rails; 3-acoustic wave gauges; 4-camera; 5-trolley; 6-towed sphere; 7-wave absorber; 8-knife across the bottom.

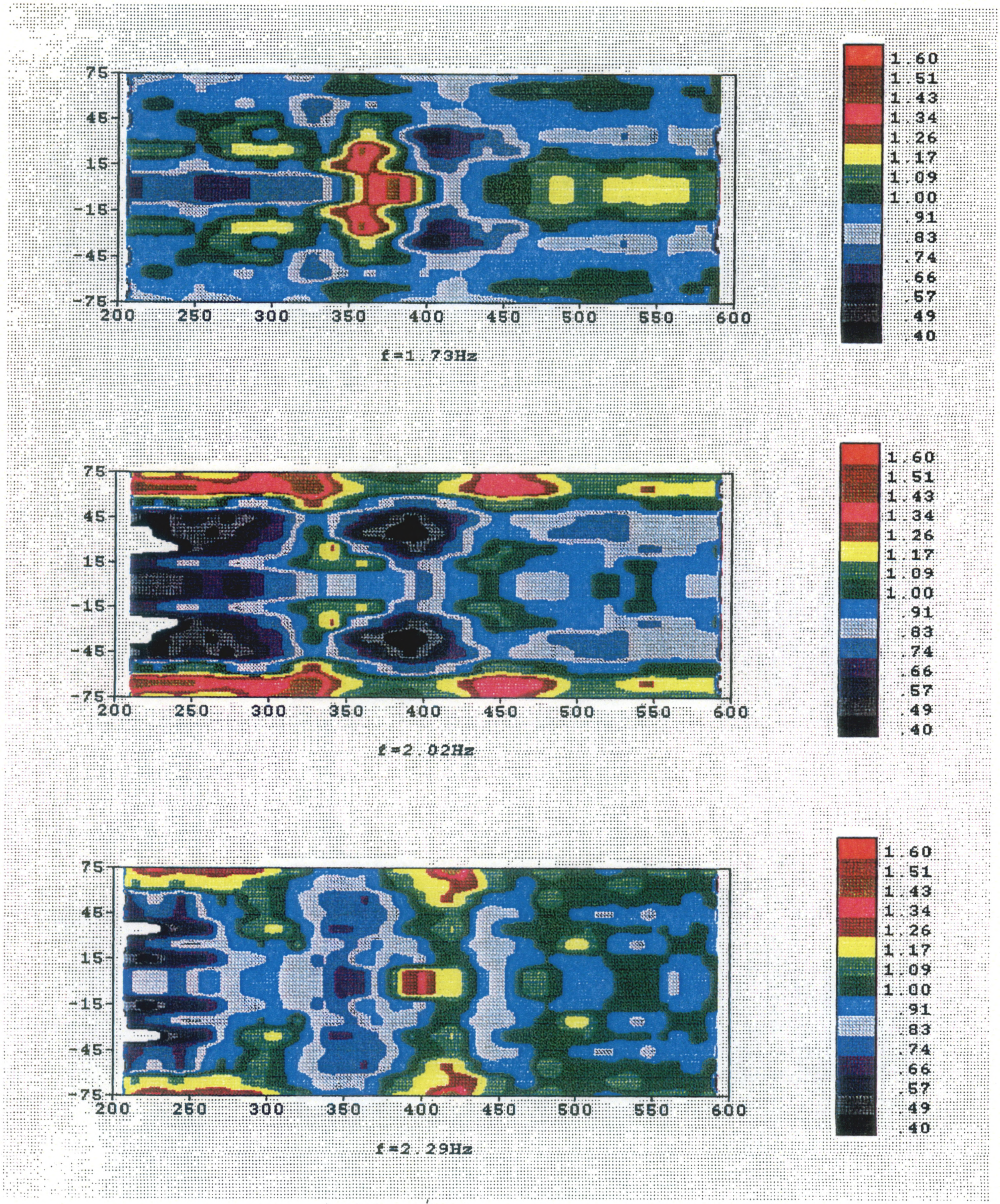

h=0.3m; R=4m; r=75mm

Fig. 18. Experimental spatial distributions of relative variation of surface wave amplitude (no. 1-3 in Table 1).

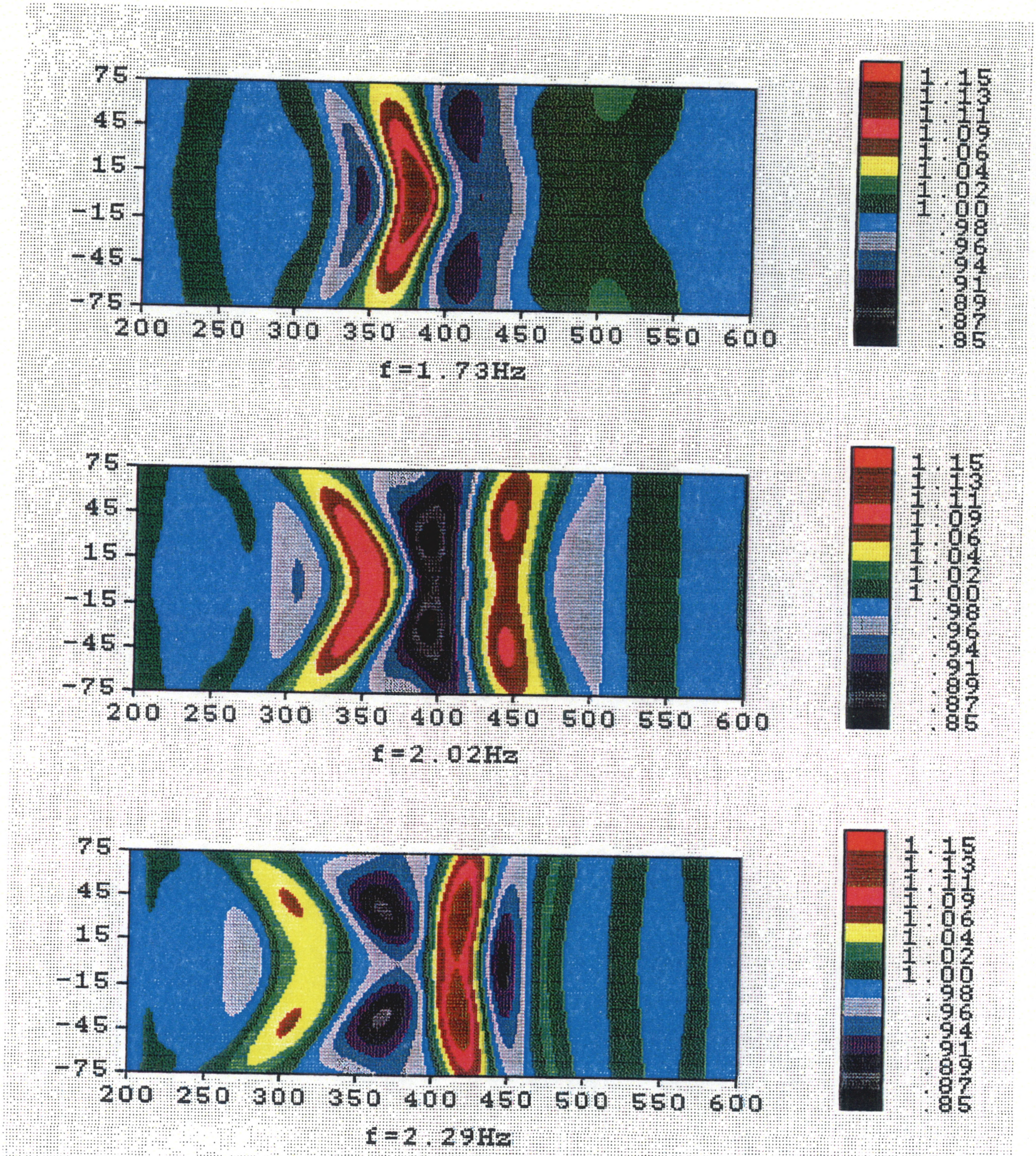

h=0.3m; R=4m; r=75mm

Fig. 19. Theoretical spatial distributions of relative variation of surface wave amplitude corresponding to Fig. 18.

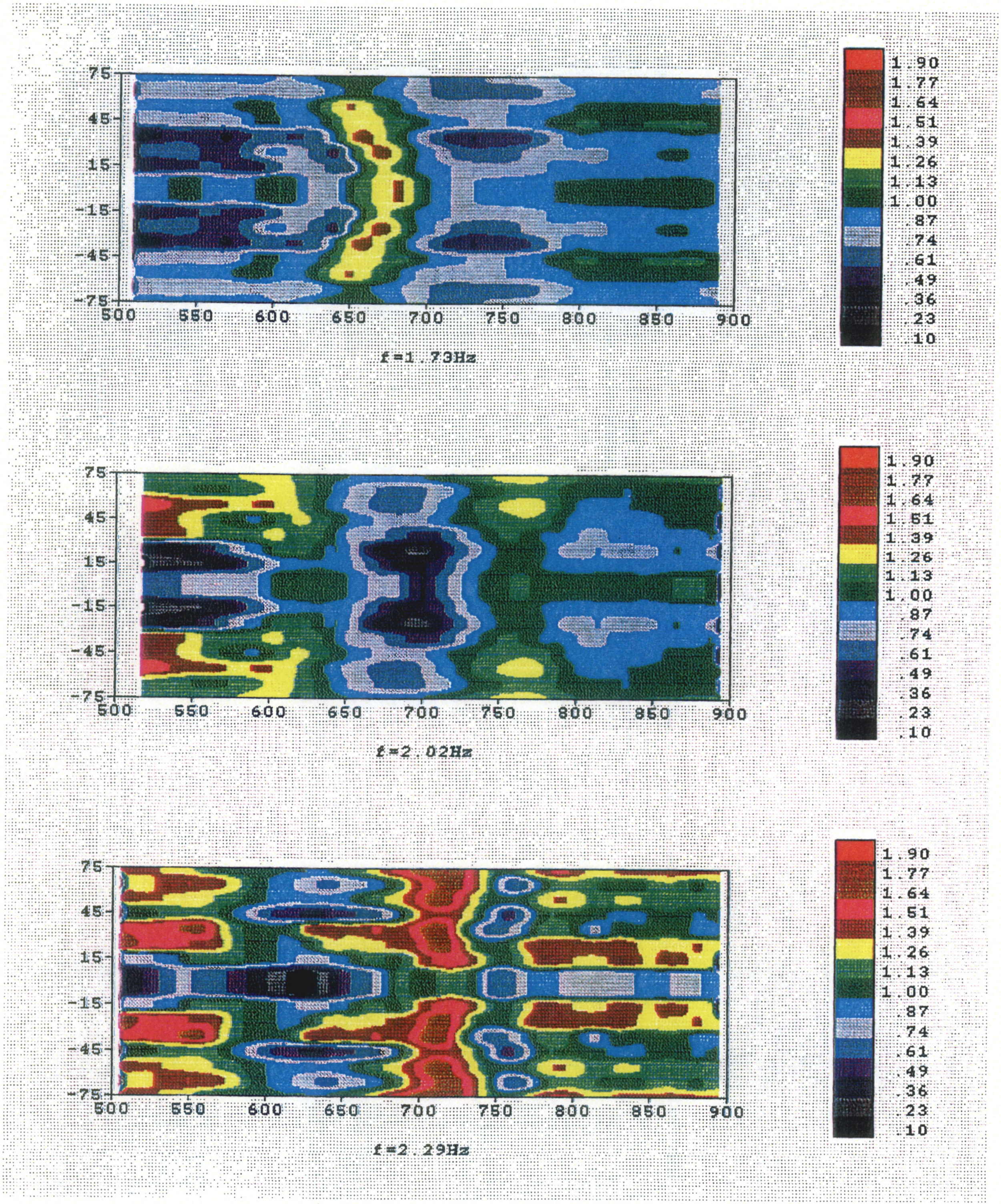

h=0.3m; R=7m; r=75mm

Fig. 20. Experimental spatial distributions of relative variation of surface wave amplitude (no. 6-8 in Table 1).

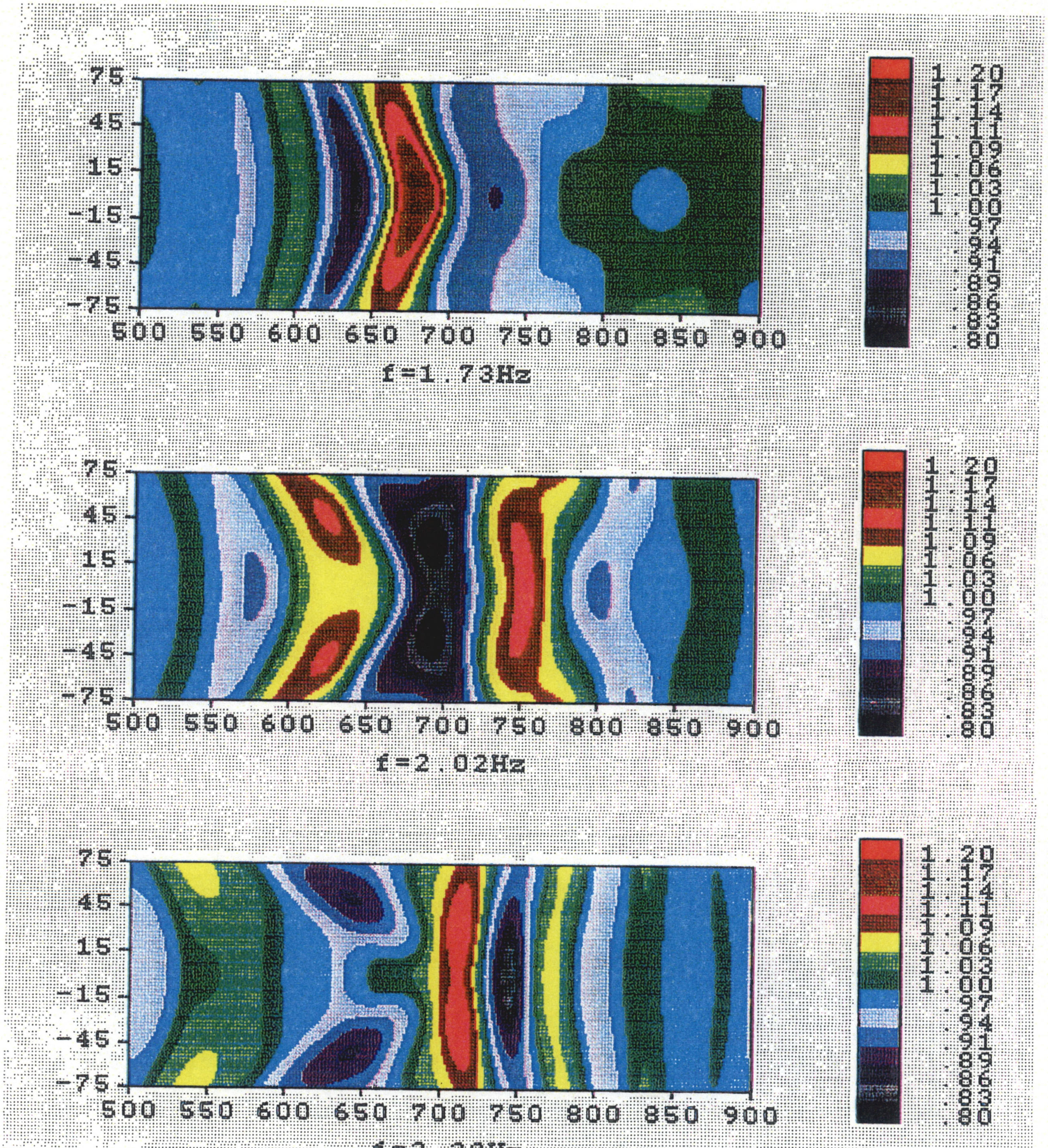

h=0.3m; R=7m; r=75mm

Fig. 21. Theoretical spatial distributions of relative variation of surface wave amplitude corresponding to Fig. 20.

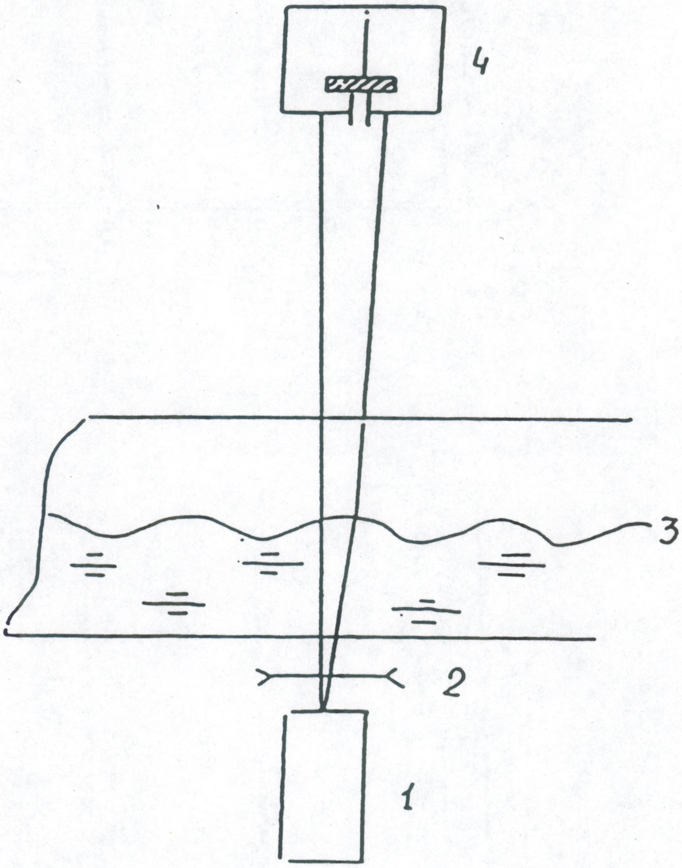

Fig. 22 Scheme of measuring waves with defocused laser beam: 1 - laser, 2 - beam formation system, 3 - hydrochannel, 4 - photoreceiver.

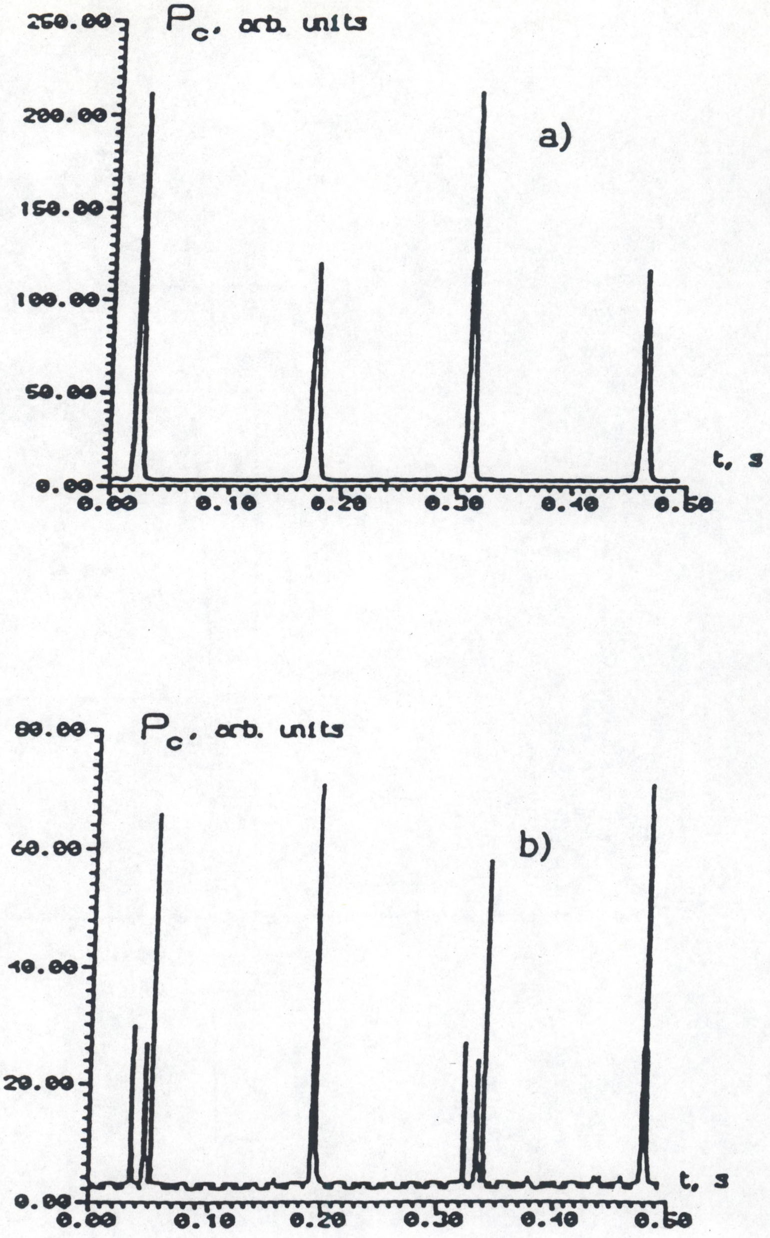

Fig. 23. Photoreceiver signal realization for gravity sinusoidal small-amplitude waves (a) and for steep gravity waves with parasitic ripple (b).

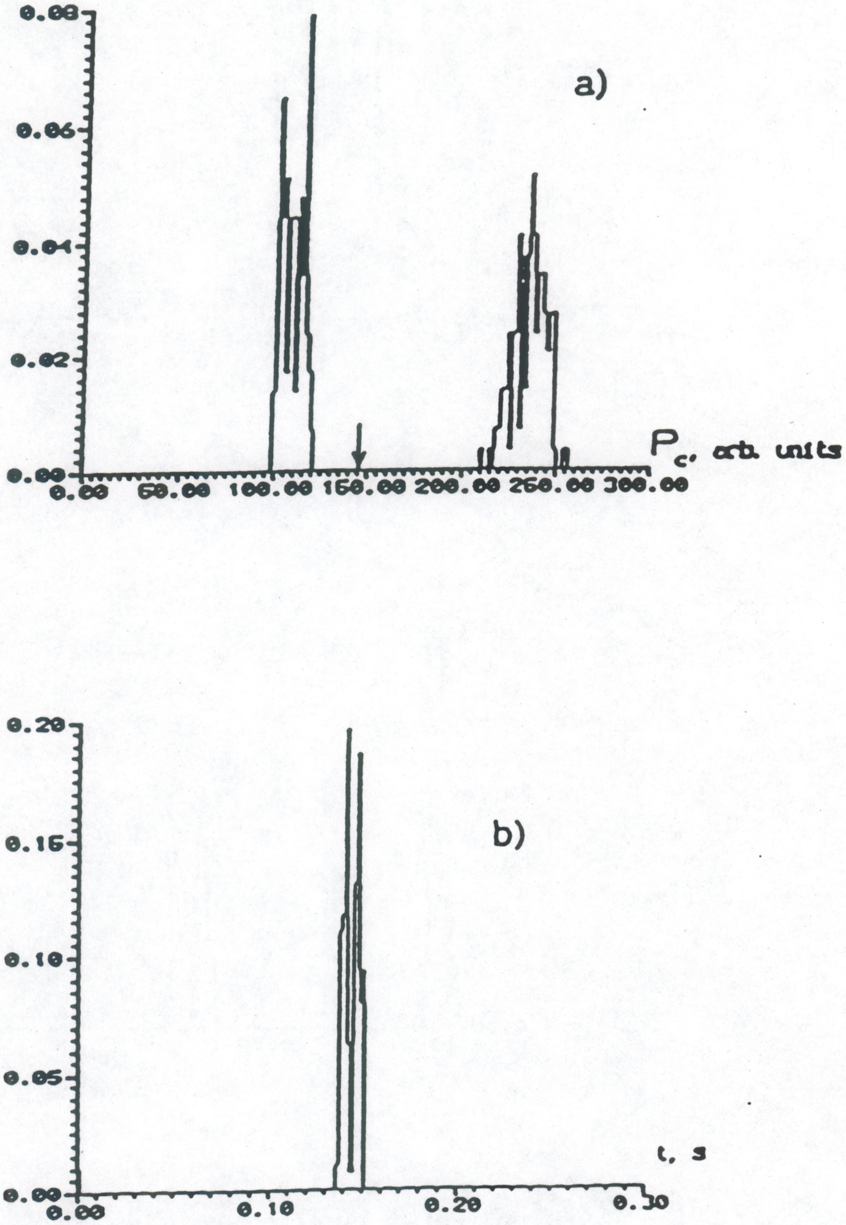

Fig. 24. Histogram of photoreceiver pulse signal amplitudes (a) and histogram of time intervals between pulses (b) for periodic gravity small-amplitude waves (regime 2). Arrow in (a) indicates signal value of 146 conv.units for a smooth surface.

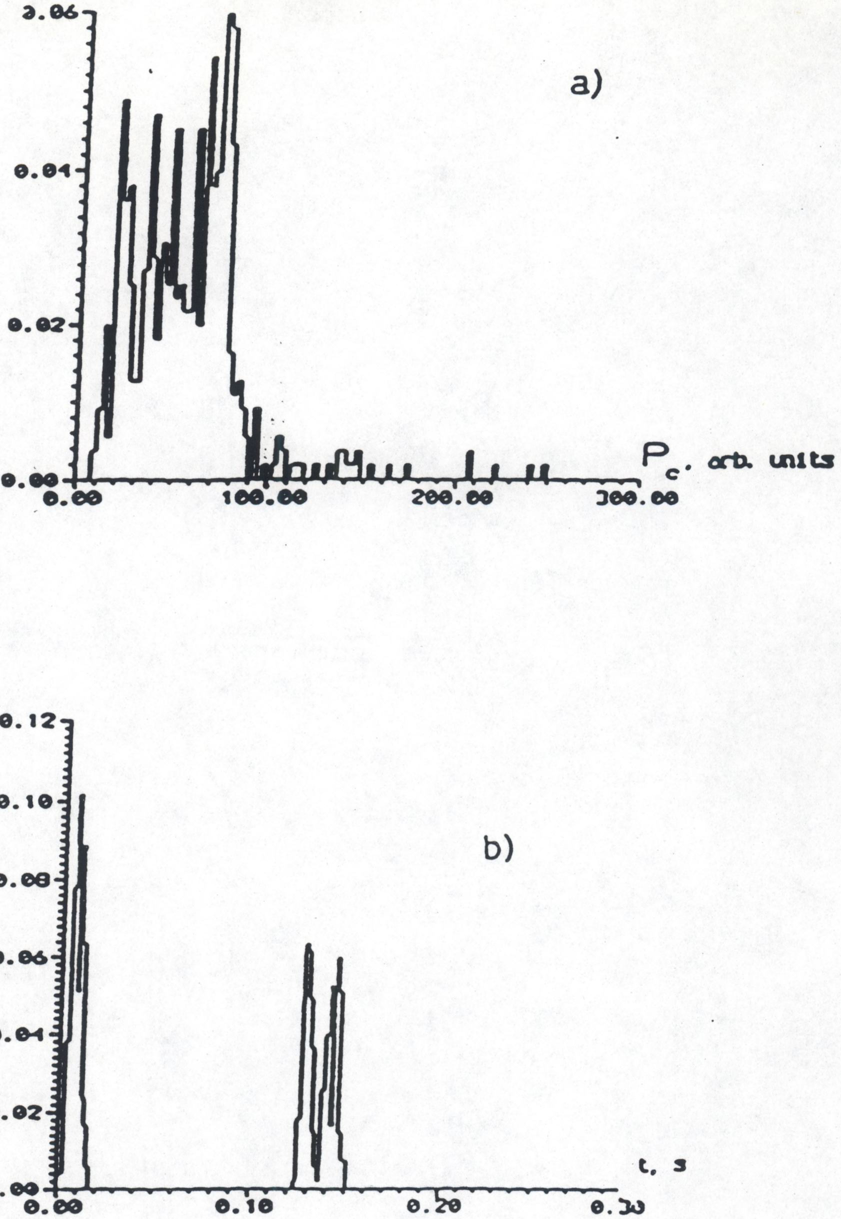

Fig. 25. Histogram of photoreceiver pulse signal amplitudes (a) and histogram of time intervals between pulses (b) for periodic gravity waves with developed parasitic ripple (regime 4).

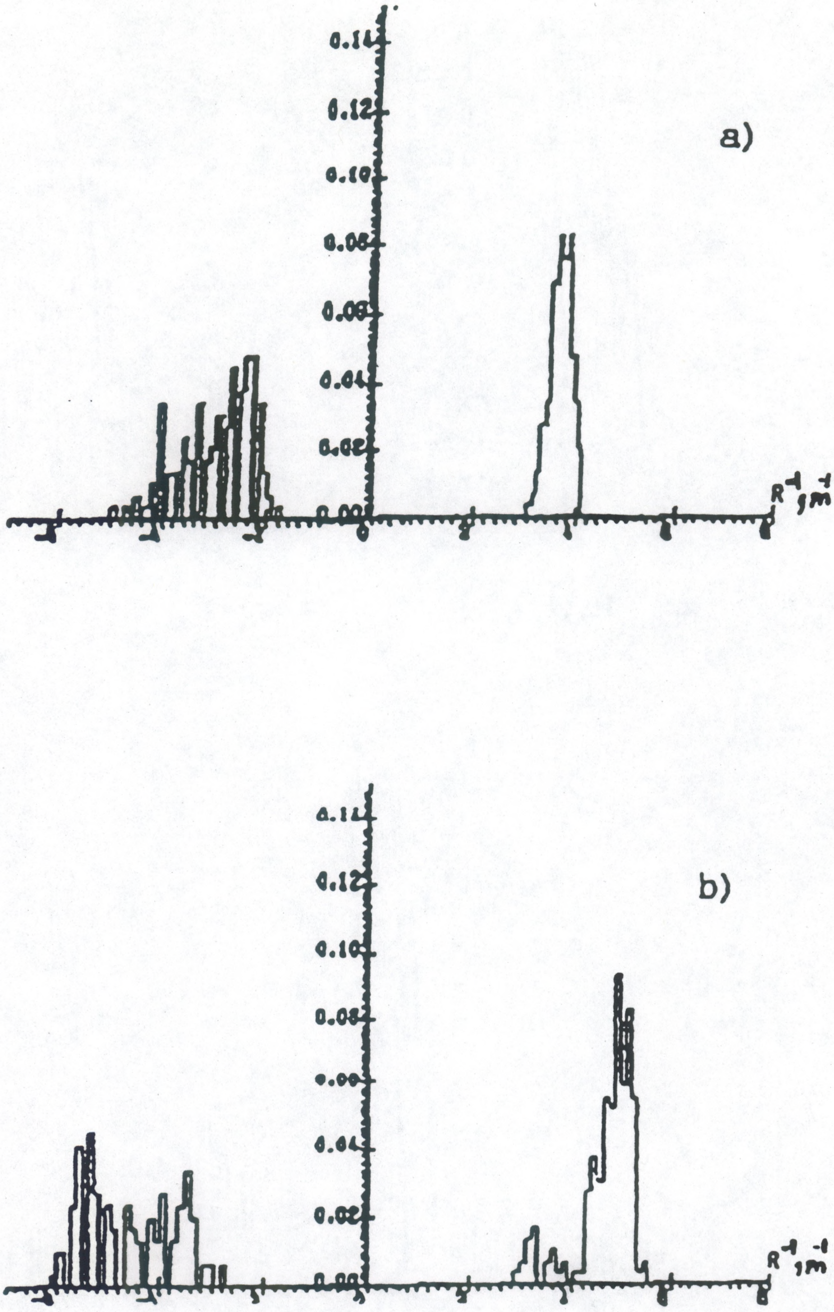

Fig.26. Histogram of curvature for periodic gravity waves of different amplitudes (a - regime 1, b - regime 2, c - regime 3, d - regime 4).

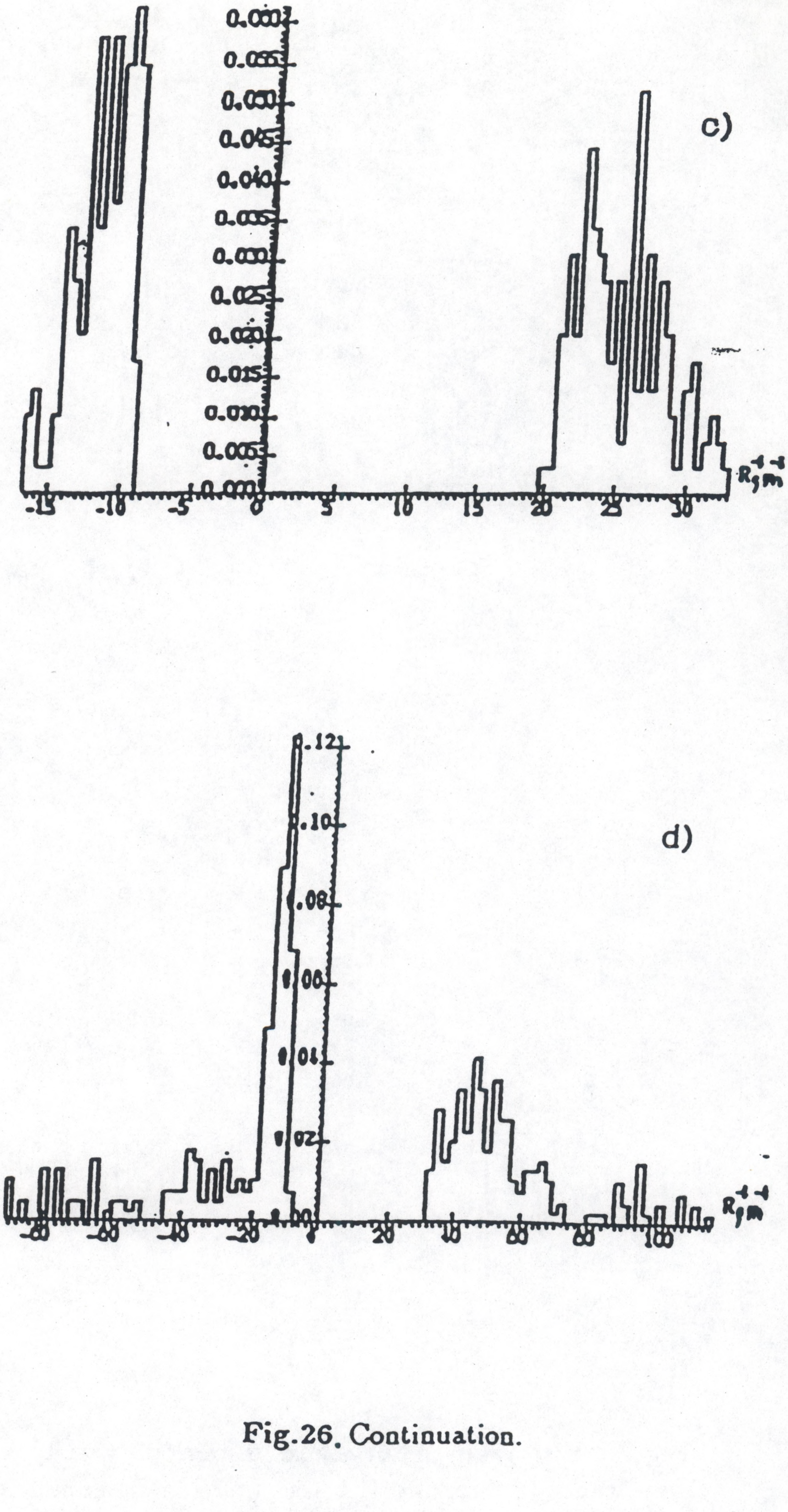

Fig.26. Continuation.

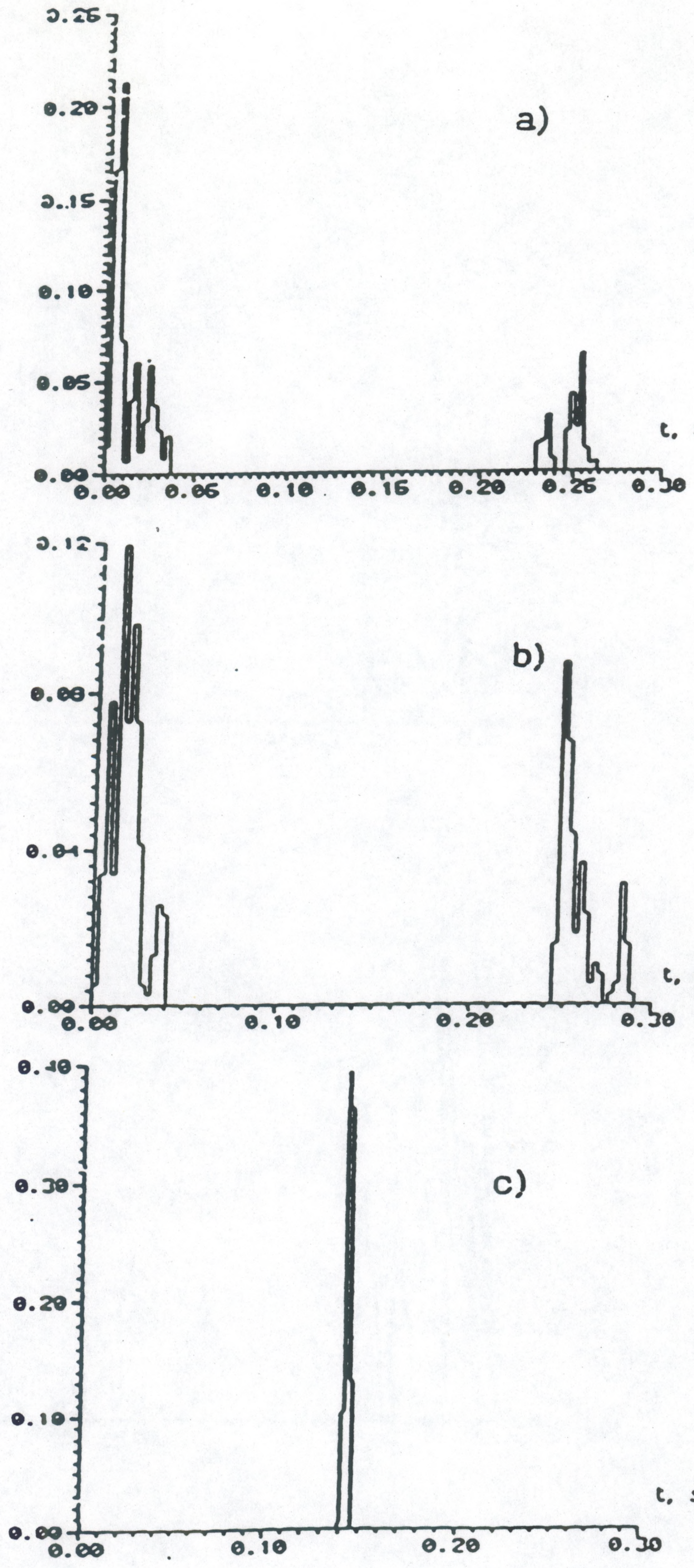

Fig. 27. Histogram of time intervals for periodic gravity waves with weakly developed ripple (regime 3) (a - on front slope, b - on rear slope, c - at zero slope points; front slope is 0.03 rad; rear slope is 0.02 rad).

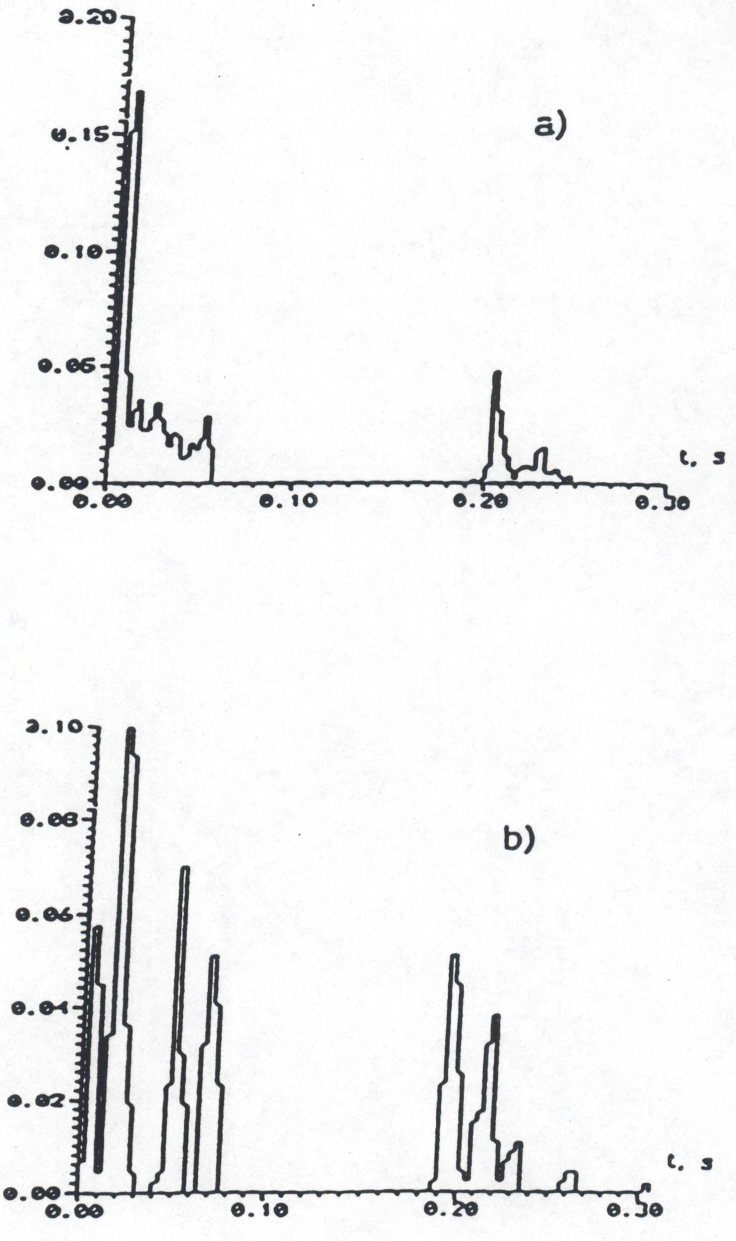

Fig. 28. Histogram of time intervals for periodic gravity wave with developed parasitic ripple (regime 4) (a - on front slope, b - on rear slope; front slope is 0. 03 rad; rear slope is 0.02 rad)

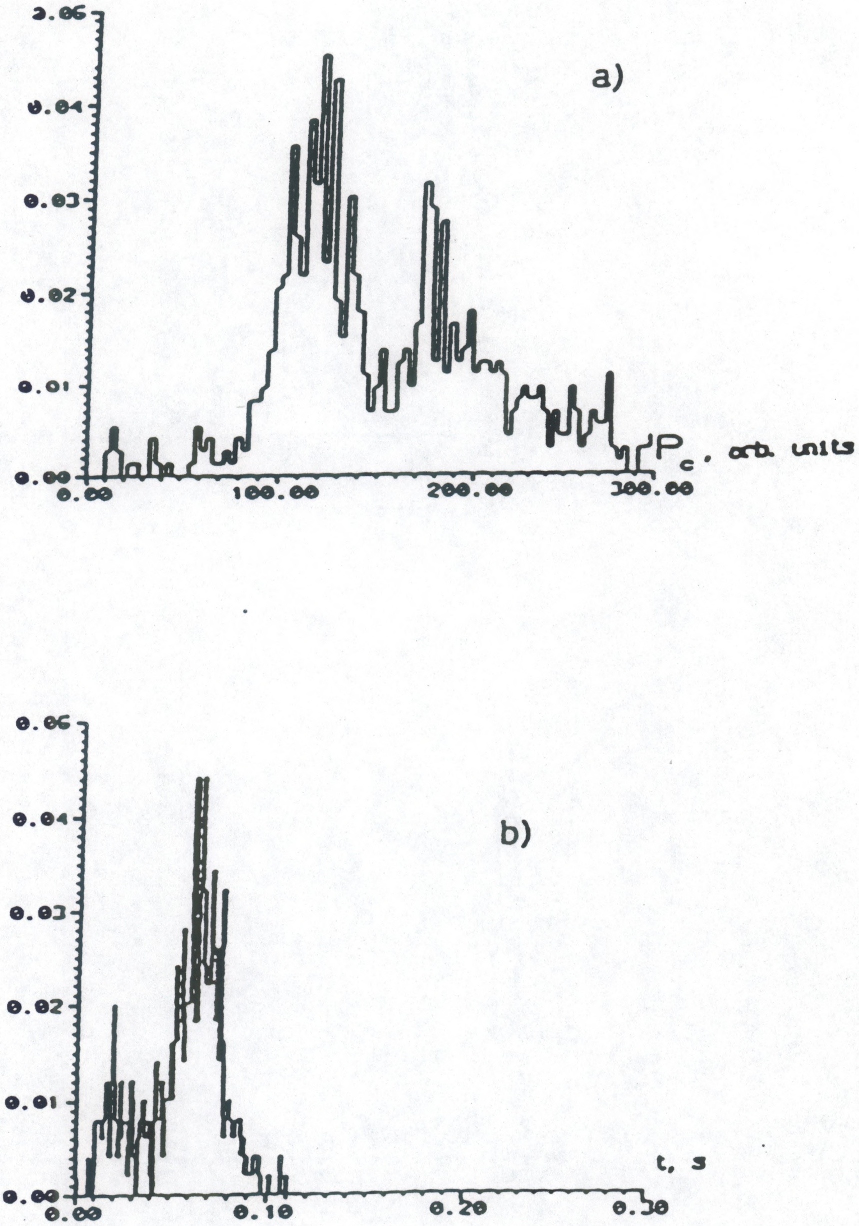

Fig. 29 Histogram of signal amplitudes (a) and time intervals (b) at zero slope points for wind velocity 2.2 m/s.

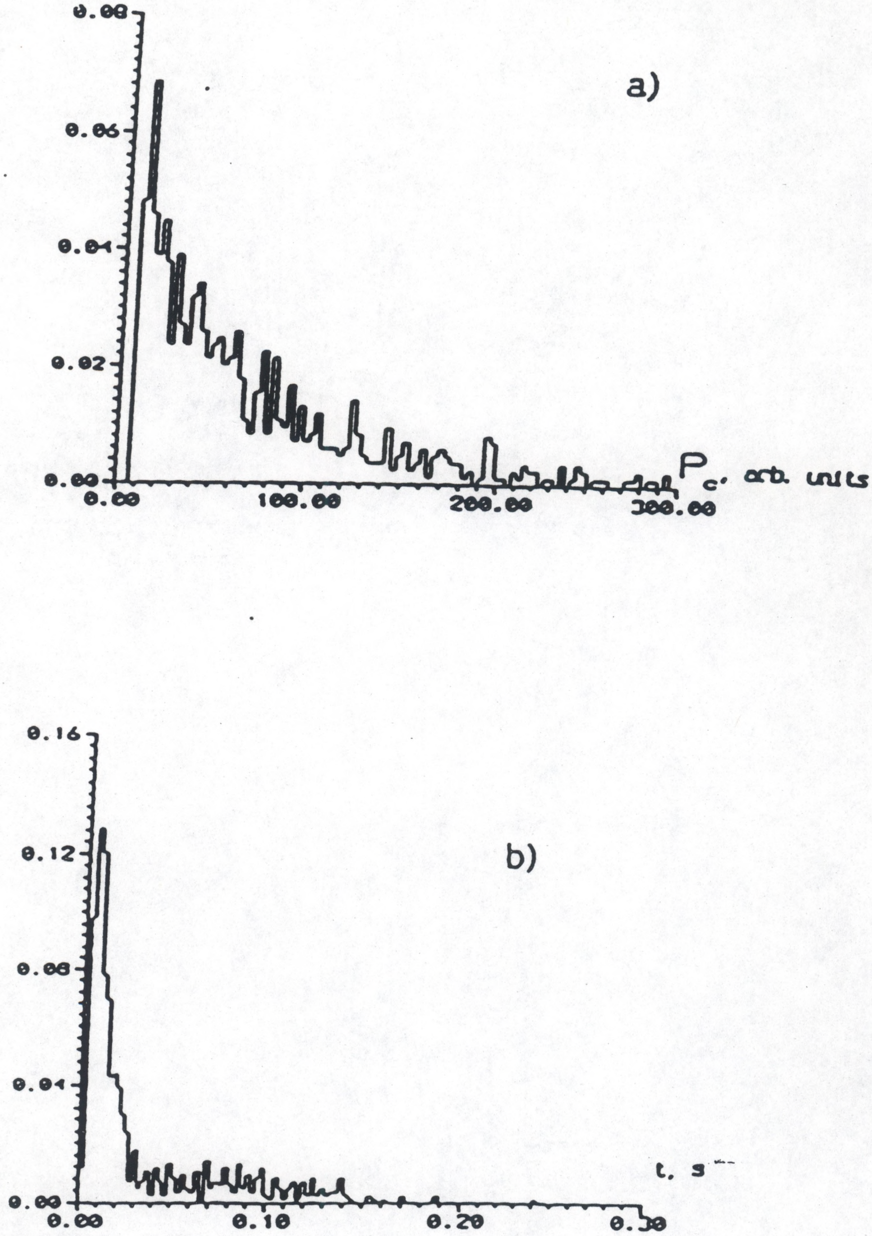

Fig. 30. Histograms of signal amplitudes (a) and time intervals (b) at zero slope points for wind velocity 4 m/s.

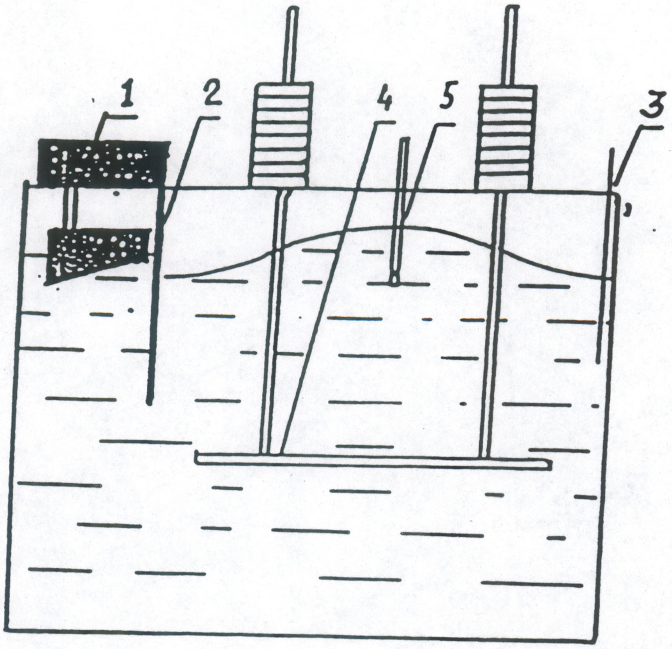

Fig. 31. Setup for study of surface wave damping at turbulence: 1-wavemaker; 2, 3-submerged walls; 4-oscillating grid; 5-thermoanemometer with sensor.

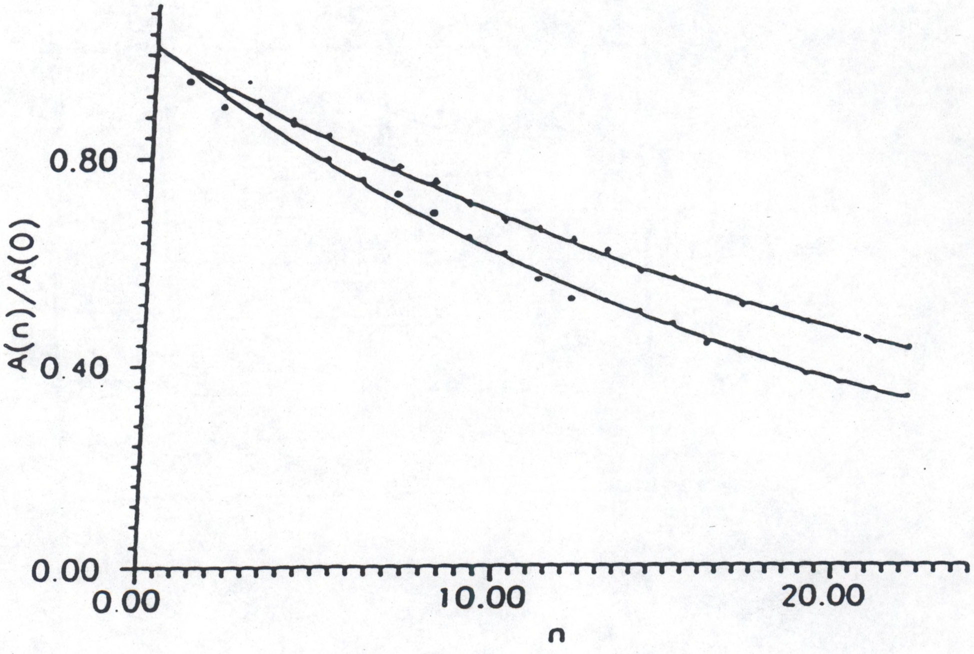

Fig. 32. Damping of free oscillations of surface in resonator without turbulence (+) and with turbulence (°).

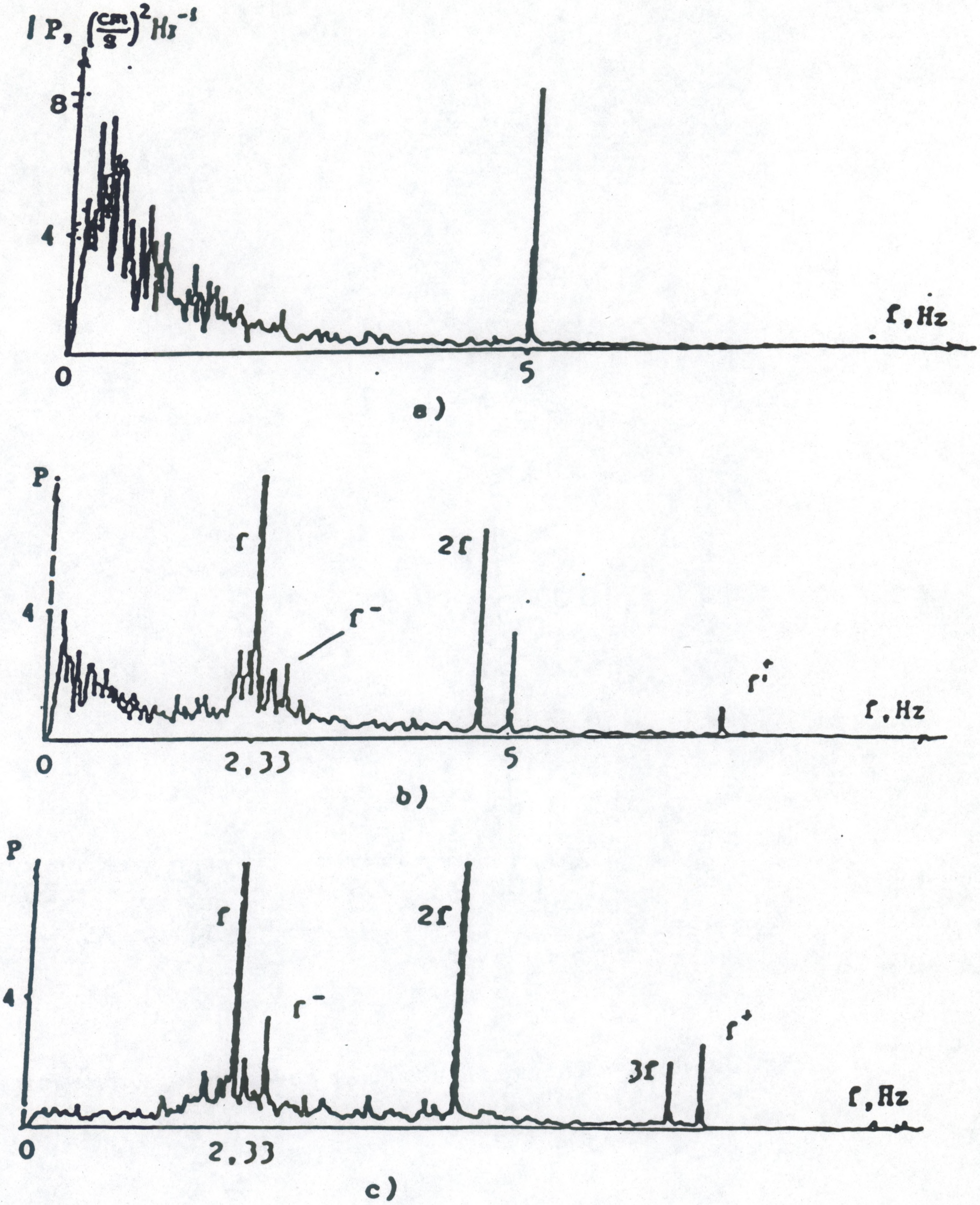

Fig. 33. Transformation of turbulence frequency spectrum (a) by the standing surface wave with amplitude $A=0.3$ cm (b) and $A=0.5$ (c)

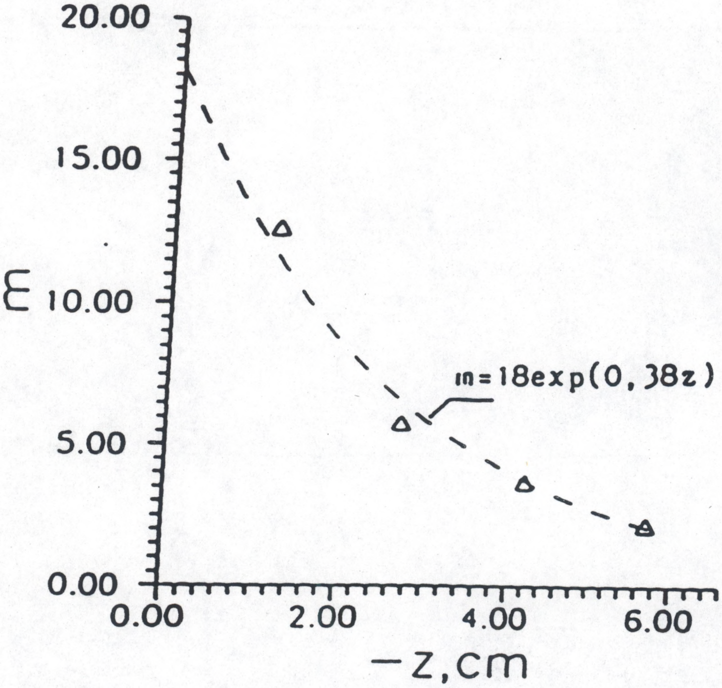

Fig. 34. Relative change of turbulence power due to surface vave vs. depth.

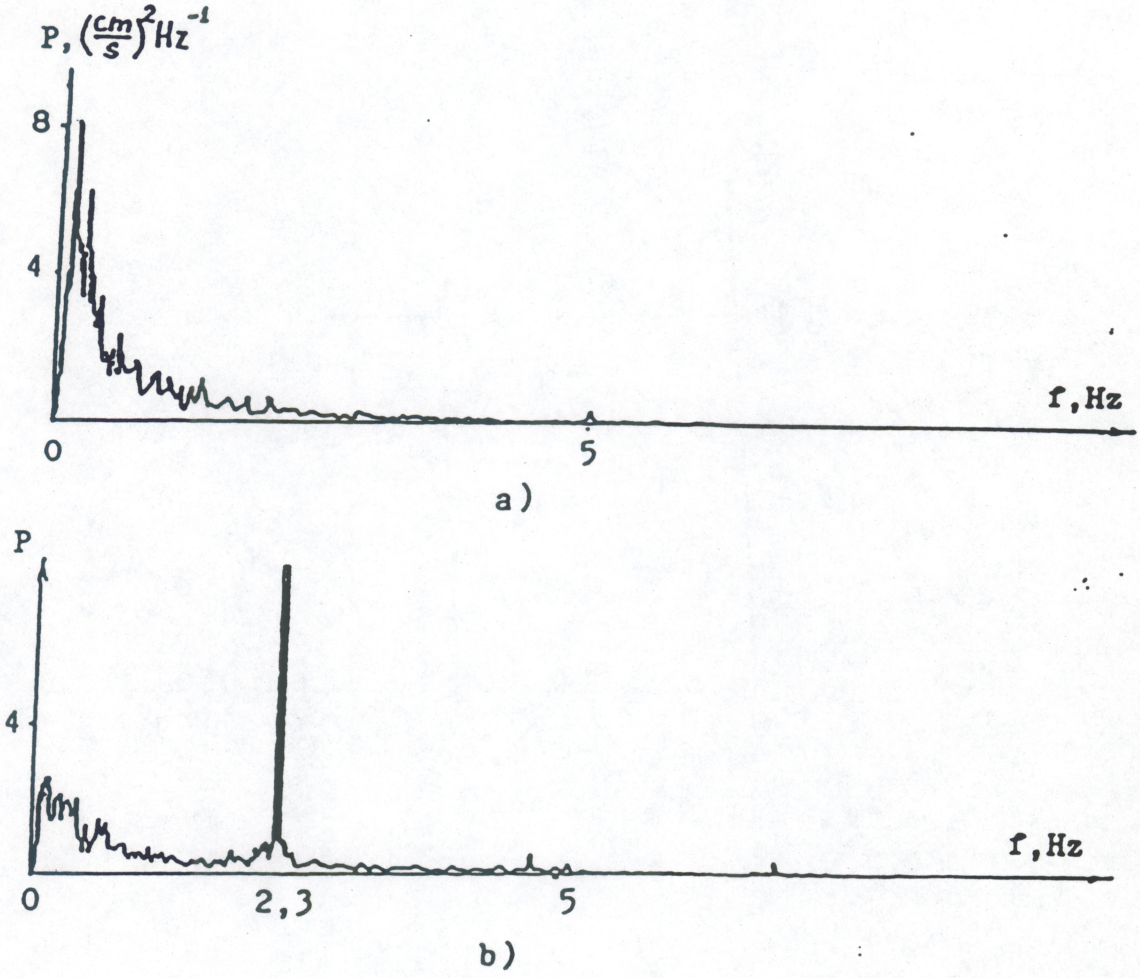

Fig.35. Transformation of turbulence frequency spectrum by the progressive surface wave.

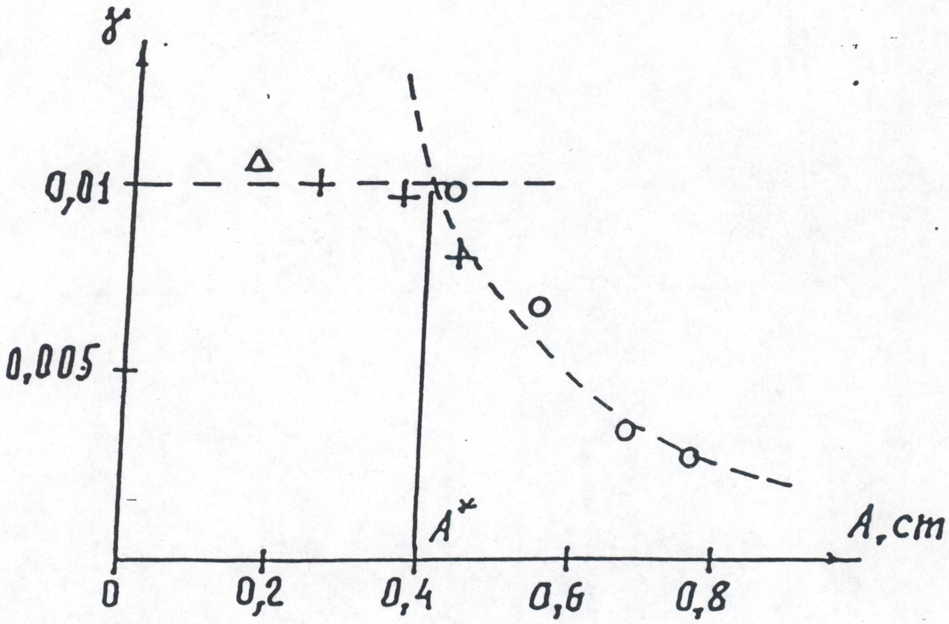

Fig.36. Dependence of decrement on damping wave amplitude.